Construction of an Optical Quarter-Wave Stack Using the ISAM (Ionic Self-Assembled Multilayers) Technique.

Kriton Papavasiliou

Dissertation submitted to the faculty of the Virginia Polytechnic Institute and State University in partial fulfillment of the requirements for the degree of

Doctor of Philosophy
In
Physics

Alfred L. Ritter
(Committee Chair)
James R. Heflin
Hans Robinson
Giti Khodaparast

July 9, 2010
Blacksburg, Virginia

Keywords: Ionic Self-Assembled Multilayers (ISAM), Titania Nanoparticles, Broad-Band Antireflection Coatings, Quarter-Wave Stacks

Construction of an Optical Quarter-Wave Stack Using the ISAM (Ionic Self-Assembled Multilayers) Technique.

Kriton Papavasiliou

Abstract

The purpose of this thesis is to make a broadband antireflection coating configuration known as a quarter-wave stack consisting of one layer of titania and of one layer of silica nanoparticles. We utilize much that is already known about silica nanoparticle deposition. The first objective of this thesis is deposition and characterization of titania nanoparticle films deposited on glass microscope slides by a technique known as Ionic Self-Assembled Multilayers or ISAM deposition. This technique takes advantage of the electrostatic attraction between oppositely charged materials and ideally results in a uniform nanoparticle film whose thickness and optical properties can be tightly controlled. Deposition of a quarter-wave stack based on ISAM deposition of silica and titania nanoparticles is significantly simpler and less expensive than alternative deposition methods.

Initial attempts to deposit titania films were unsuccessful because of excess diffuse scattering due to inhomogeneities in the film. In order to reduce diffuse scattering, two approaches were considered. The first approach was to improve the deposition process itself by experimenting with different values of deposition parameters such as solution pH and solution molarity. The other approach focused on removing the large nanoparticle aggregates from the colloidal solutions of titania nanoparticles that were suspected to be responsible for rough film surfaces resulting in diffuse scattering. This approach was successful. In addition, evidence suggested that surface roughness contributed more to diffuse scattering than the bulk of the films.

After minimizing diffuse scattering from titania nanoparticle films, we used known results from research on silica nanoparticle films to deposit quarter-wave stacks consisting of one layer of titania nanoparticles with high refractive index and one layer of silica nanoparticles with low refractive index. This contrast in refractive indices is a desirable characteristic of quarter-wave

stacks. The thicknesses and refractive indices of the two layers in the quarter-wave stacks were measured by ellipsometry and compared to the nominal thicknesses of these layers. Finally, the reflectance was derived from a model of the quarter-wave stack and was compared to the measured reflectance. It was found that construction of a quarter-wave stack by ISAM is possible but that it will be necessary to acquire data from more experiments.

Στους γονείς μου Θωμά και Θεοδώρα

Acknowledgments

This is probably the most fun part of the thesis. It is the point where I get to give sincere thanks to everyone who has been a significant help during these years.

First of all, great thanks and appreciation to my advisor Dr. Alfred L. Ritter for guidance, very useful advice, and overall mentoring. By example and patience he made me appreciate the value of research.

Also I owe many thanks for very useful advice and help to Dr. Randy Heflin whose work is in the same field.

I am very grateful to Drs. Hans Robinson and Giti Khodaparast for being on my committee and displaying great patience. Also many thanks to Dr. Tetsuro Mizutani who was on my committee initially but is now enjoying retirement.

Everything I have come to know about proper procedures and overall lab etiquette (a very underrated aspect of experimental physics) I owe to Cemil Durak and Jason Ridley. I will do my best to pass on their wisdom.

Many thanks to all the people who saved several expensive instruments from being used by me without previous training. These are Anamika Gopal and Manpreet Kaur (Filmetrics), Raquel Mejia-Ariza and William Miles (DLS), Russell Mammei (Ellipsometer), Steve McCartney, John McIntosh, and Frank Cromer (AFM, SEM), and everyone at the machine shop.

I also want to add one more entry to probably the most thanked person in the physics department at Virginia Tech, Chris Thomas who is always eager to help graduate students.

Also thanks to Mary Jane Smith for help with labyrinthine paperwork and Travis Heath for equally valuable computer help.

I also want to acknowledge financial support from the Army Research Laboratory under the Cooperative Agreement Number W911NF-06-2-0014.

Much gratitude to Leah Wolford for displaying mastery and providing priceless help with page numbering.

The only self-praise I can give is that I completed this work in the summer of 2010 without ever owning a computer.

Finally I want to thank the entire physics department at Virginia Tech especially for giving me the opportunity to teach a full course during my last semester as a graduate student, an

experience that I very much enjoyed. I am looking very forward to working with you all starting the following academic year.

Personal thanks

First of all my parents Thomas and Theodora. There are not enough words to express this properly so I will leave it at that. Also my sister Faidra who made it to this point much faster than I did.

There are many close friends and relatives that I want to mention here. My sincere apologies if I am forgetting anyone. I consider myself very fortunate to have been close to the following people: Leah Wolford, Dan and Irina Mazilu, Cemil Durak, Thanos Bisbikas, Dimitris "The Trooper" Stalidis, Catalin Ticos, and all my close relatives in Athens, San Antonio, Los Angeles, and England.

Thanks also to JoAnna Lujan, Vasilia Zivala, Daniela Bogorin, Ying Shen, and everyone at the University of Texas at San Antonio for valuable friendship and education in the early years. I am also very grateful to Victoria Soghomonian for valuable advice and support.

TABLE OF CONTENTS

LIST OF FIGURES

CHAPTER ONE

CHAPTER FOUR

CHAPTER FIVE

CHAPTER SIX

LIST OF TABLES

CHAPTER TWO

CHAPTER FOUR

CHAPTER FIVE

CHAPTER SIX

CHAPTER ONE

Introduction

Antireflection (AR) coatings have been used for many years in order to reduce reflection of incident light from surfaces. The idea is quite simple. Form a film over the surface such that the light reflected from the substrate/film interface will interfere destructively with light reflected from the film/air interface. We present here briefly the theory of reflectance from single and from multiple layer thin films as well as a film characterization technique known as ellipsometry. In addition we give an overview of loss processes such as diffuse scattering and absorption. Finally we review ISAM which is our choice for a deposition technique.

1.1 Motivation

There are many applications for antireflection coatings for optical media such as lenses, monitor screens, eyewear, windows, photovoltaic devices, etc, that require high transmittance and hence low reflectance. Antireflection coatings are commercially available but most methods of producing them are complicated and/or expensive and difficult to perform for large and/or non-flat surfaces. Nanoparticle films can be easily and inexpensively deposited on substrates of various sizes and shapes by ISAM.

1.2 Theory

1.2.1 Single Layer Antireflection

Considering only the case of normal incidence, there are two relatively simple conditions that must be met in order for the reflectance to equal exactly zero. These are:

1) $OT = k\,\frac{\lambda}{4}$ where $OT = n_{film} * Thickness$ and k = odd integer

2) $n_{film} = \sqrt{n_{substrate} n_{air}}$

The first condition insures that the two waves are out of phase by 180^{o} so that they interfere destructively, provided that the incident light is always moving from an optically thin medium to

an optically denser one, and the second insures that the amplitudes of the two reflected waves will be the same so that they can completely cancel each other out.

The first condition makes control of the film's thickness desirable and the second condition requires control over the film's index of refraction. The second condition is usually more difficult to satisfy as different materials that could be deposited as film have fixed optical properties that will not in general satisfy it. It is this second condition that makes SiO_2 a good material for an antireflection coating. The index of refraction of a closely packed silica nanoparticle film is approximately 1.25 while condition 2 gives $n_{film} = 1.22$ if we take glass as the substrate ($n \approx 1.5$). The proximity of these two values is what makes a silica nanoparticle film worth pursuing as an antireflection coating.

Condition 1 implies that there are only few distinct wavelengths at which the reflectance equals zero. In addition, the range of wavelengths over which reflectance is minimum is rather narrow. There are many uses for a coating capable of reducing reflectance over a broader region of wavelength, especially if one can be constructed in a simple and inexpensive manner. The primary objective of this thesis is the construction of such a broad-band (BB) antireflection coating by ISAM. A broad-band antireflection coating necessarily requires a minimum of two layers of two different materials. The difference between a single layer AR coating and a multilayer broadband coating is illustrated in Fig.1.1 used with the permission of ISP Optics.

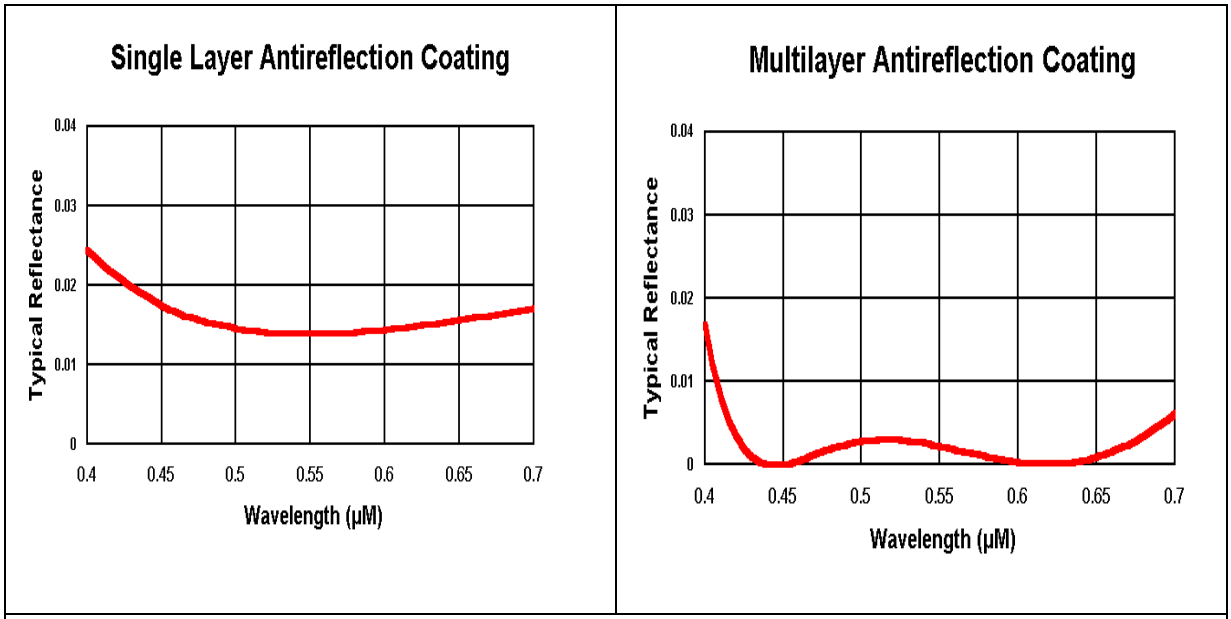

Fig. 1.1. Single wavelength reflectance and broad-band reflectance. Courtesy of ISP Optics.

A quarter-wave stack is one possible approach to making a broadband AR coating. It is desirable to have a large contrast between the refractive indices of the two materials. Silica films, which have been extensively studied, have a relatively low refractive index and can serve as one of the two components of the quarter-wave stack. For the second component we chose titania which has one of the highest refractive indices among known and widely used dielectrics that are transparent in the visible spectrum. The main part of this thesis is developing the process for depositing a single layer titania film by ISAM. It was found that due to the initial inhomogeneity of these films, there was an unacceptable level of diffuse scattering. The major emphasis of this thesis was optimizing the deposition process to minimize this diffuse scattering.

1.2.2 Theory of Reflectance – Quarter-Wave Stacks

There is a well established theory for reflectance and transmittance of light incident on a surface, whether this surface is conducting or not. Here we will look at reflectance from a single layer film deposited on glass as well as reflectance from a double layer film consisting of one layer of low refractive index on another layer of high refractive index the combination of which is deposited on a glass surface. If the optical thickness of each layer is one quarter of a target wavelength where R is minimum, then the arrangement is known as a high-low (HL) quarter wave stack and theory predicts that it will broaden the range of wavelength over which reflectance is minimized.

The theory of reflectance from thin films can be found in any intermediate or advanced optics textbook such as Optics by Hecht[1]. By considering total electric and magnetic fields on both sides of an interface as well as the continuity requirements for these fields it can be shown that

$$\begin{bmatrix} E_I \\ H_I \end{bmatrix} = \begin{bmatrix} \cos k_0 h & (i \sin k_0 h)/Y_I \\ Y_I i \sin k_0 h & \cos k_0 h \end{bmatrix} \begin{bmatrix} E_{II} \\ H_{II} \end{bmatrix} \qquad \text{(Eq. 1.1)}$$

where $E_{I,II}$ and $H_{I,II}$ are the total electric and magnetic fields on each side of the interface, h is the film thickness, $k_0 = 2\pi/\lambda$ and $Y_I = \sqrt{\frac{\varepsilon_0}{\mu_0}} n_I \cos\vartheta_{incident}$ where ε_0 is the permittivity of free space, μ_0 is the permeability of free space, n_1 is the refractive index of the film, and $\vartheta_{incident}$ is the angle between the incident ray and the normal to the surface.

In all that follows, all the incident angles are taken to be 0^o, that is, we only consider normal incidence. The matrix in the above equation is called the characteristic matrix of the film and is denoted by M. If the film consists of more than one layer, say p layers, the characteristic matrix of this multimaterial film is simply the product of the individual matrices:

$$M_{film} = M_I M_{II} \cdots M_P \qquad \text{(Eq. 1.2)}$$

Therefore the characteristic matrix of an HL quarter-wave stack is the product of two characteristic matrices for the two different materials. Fig. 1.2 is a schematic of a HL quarter-wave stack.

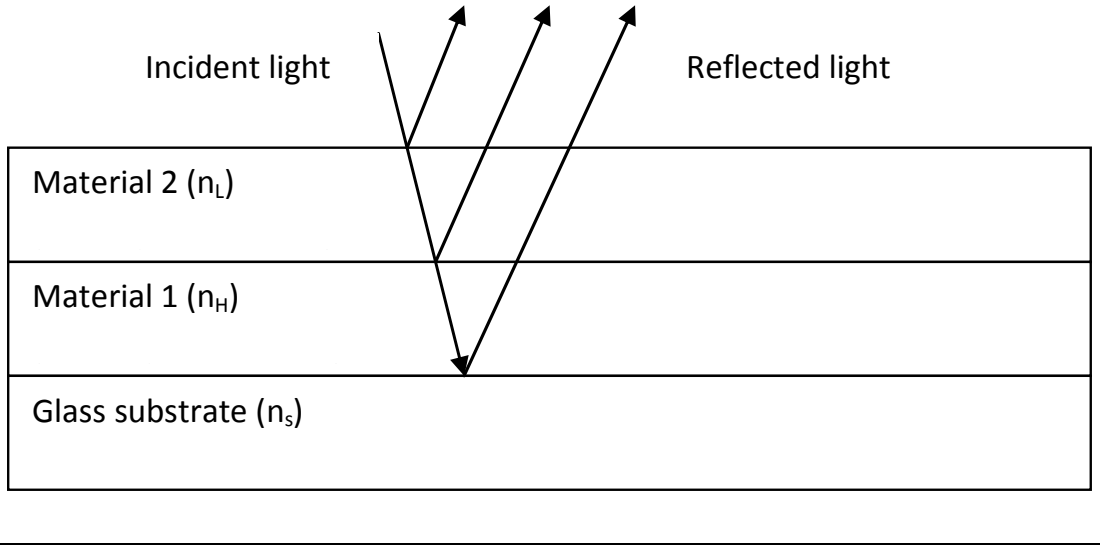

Fig. 1.2. HL Quarter wave stack.

The importance of the characteristic matrix is that it allows us to calculate the coefficient of reflection and transmission with relative ease. These coefficients turn out to be:

$$r = \frac{Y_o m_{11} + Y_0 Y_s m_{12} - m_{21} - Y_s m_{22}}{Y_0 m_{11} + Y_0 Y_s m_{12} + m_{21} + Y_s m_{22}} \qquad \text{(Eq. 1.3)}$$

and

$$t = \frac{2\,Y_o}{Y_0 m_{11} + Y_0 Y_s m_{12} + m_{21} + Y_s m_{22}} \qquad \text{(Eq. 1.4)}$$

where the m's are the elements of the 2 x 2 characteristic matrix, the subscript s refers to the substrate, and the subscript 0 refers to air. The reflectance R is defined as the square of the reflection coefficient and the transmittance T as the square of the transmission coefficient. If we

calculate those for a single layer film and set R equal to zero, we recover condition 2 above for antireflectance. We note that in the case of zero scattering and zero absorption, R + T = 1. The only difficulty now for evaluating R and T for any film, whether composed of a single material or many different materials, is to evaluate the characteristic matrix M by forming the product of the individual characteristic matrices for each material.

Fig.1.3 shows the reflectance of a single layer film superimposed with the reflectance of a HL quarter-wave stack for a center wavelength $\lambda = 0.5$ μm (yellow). R is plotted versus $1/\lambda$ so that the extrema are equally spaced.

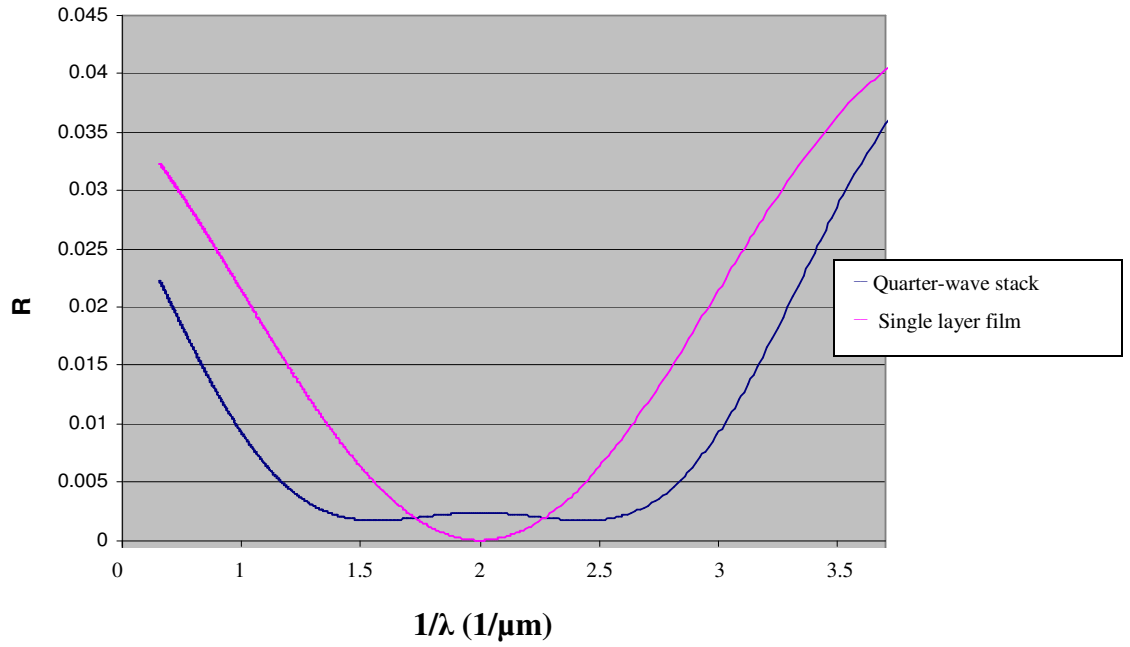

Fig. 1.3. Effect of quarter-wave stack on reflectance. Quarter-wave stack reflectance (blue), single layer film reflectance (red).

For this graph, the thickness of the titania layer is 70nm, the thickness of the silica layer is 100nm, the refractive index of the titania layer is 1.8, and the refractive index of the silica layer is 1.25. These values give optical thicknesses equal to 125nm for both layers which corresponds to a quarter wave stack "tuned" to 500nm which is the middle of the visible part of the spectrum. We can see that the effect of the quarter wave stack is the broadening of the region of minimum reflectivity. This is the first step to broadband antireflection coatings. It should be noted here

that there is no limit as to the number of layers in a quarter wave stack. Fig. 1.3 above shows R for a quarter wave stack of two layers one with high index of refraction and one with low index of refraction, here assumed constant.

1.2.3 Film Characterization – Ellipsometry

An optical film is characterized by its optical properties (index of refraction and coefficient of extinction) and its thickness. In addition, inhomogeneous films, such as those consisting of nanoparticles, exhibit diffuse scattering, either due to bulk inhomogeneities or to surface roughness, inherent in the deposition process. The film's optical properties and thickness can be measured by ellipsometry. An ellipsometer measures the relative amplitude and the change in polarization of incident light after reflection characterized by two angles, Δ and Ψ respectively. The acquired data are then fitted with a model to obtain the thickness and the refractive index. All the models described here are applicable to single as well as multiple layer films.

There are a variety of models that we can use and each can be modified slightly to account for imperfections in the data taking such as the incident beam's angular spread. In addition, features such as refractive index grading of the film can be added. For our purposes, we used the following three:

1) **Effective Medium Approximation (EMA).** The dielectric constant is assumed complex to account for extinction due to the losses of the material:

$$\varepsilon_{complex} = \varepsilon_{real} + i\,\varepsilon_{imaginary} \qquad \text{(Eq. 1.5)}$$

The relation between the complex dielectric constant and the complex refractive index is

$$n^2_{complex} = \varepsilon_{complex} \qquad \text{(Eq. 1.6)}$$

and

$$n_{complex}(\lambda) = n(\lambda) + i\,k(\lambda) \qquad \text{(Eq. 1.7)}$$

where n and k are the refractive index and extinction coefficient, respectively. There are several approaches to evaluating the effective complex dielectric constant by EMA[2,3]. For this work, we chose the Bruggeman equation:

$$\varepsilon_{eff} = \frac{\varepsilon_2 + 2\varepsilon_1 + 2f_{ti\tan ia}(\varepsilon_2 - \varepsilon_1)}{\varepsilon_2 + 2\varepsilon_1 - f_{ti\tan ia}(\varepsilon_2 - \varepsilon_1)}\varepsilon_1 \qquad \text{(Eq. 1.8)}$$

where ε_1 is the complex dielectric constant of the matrix (in our case void space between the particles), ε_2 is the complex dielectric constant of the inclusions (in our case the titania nanoparticles), and $f_{titania}$ is the volume fraction of titania in the film. Hence this equation gives the effective complex dielectric constant ε_{eff} of a mixture of two materials in terms of the optical properties of each one in bulk. For this to work we have to know the optical properties of pure titania. Bulk titania comes in crystalline forms such as anatase, rutile, and brookite. The majority of the commercially available titania nanoparticles are anatase. We obtained the optical properties of pure anatase from Mardare et al.[4] where the refractive index and extinction coefficient are given as functions of wavelength. In Fig. 1.4 is shown the index of refraction and the extinction coefficient as functions of wavelength of a mixture 1/3 void and 2/3 anatase titania based on the EMA model.

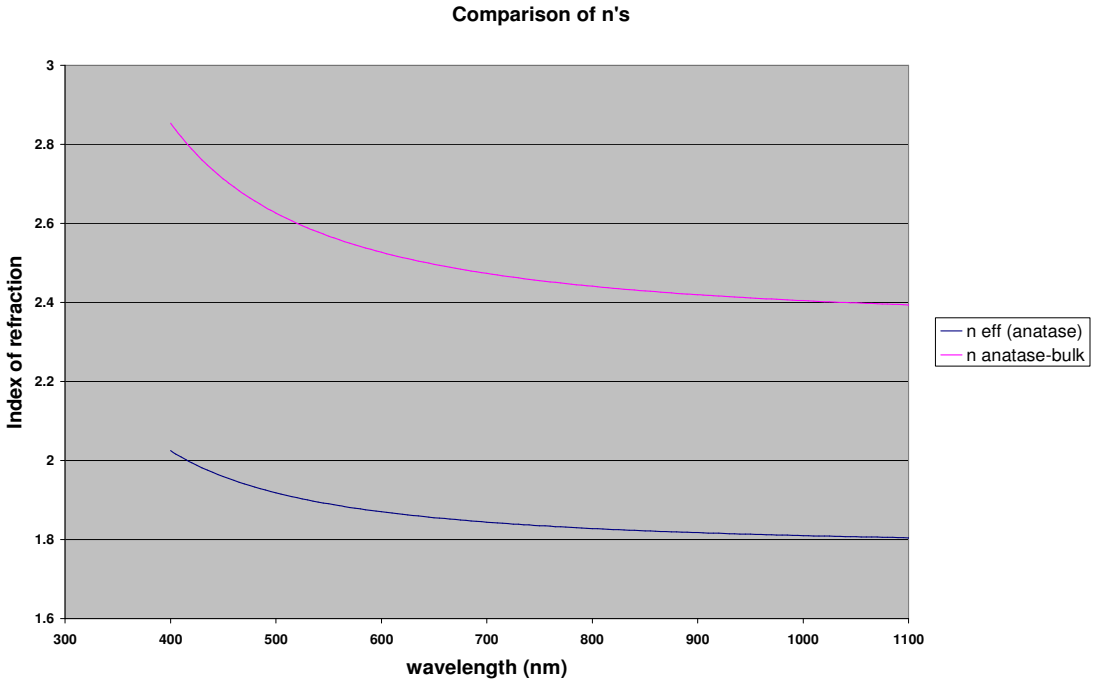

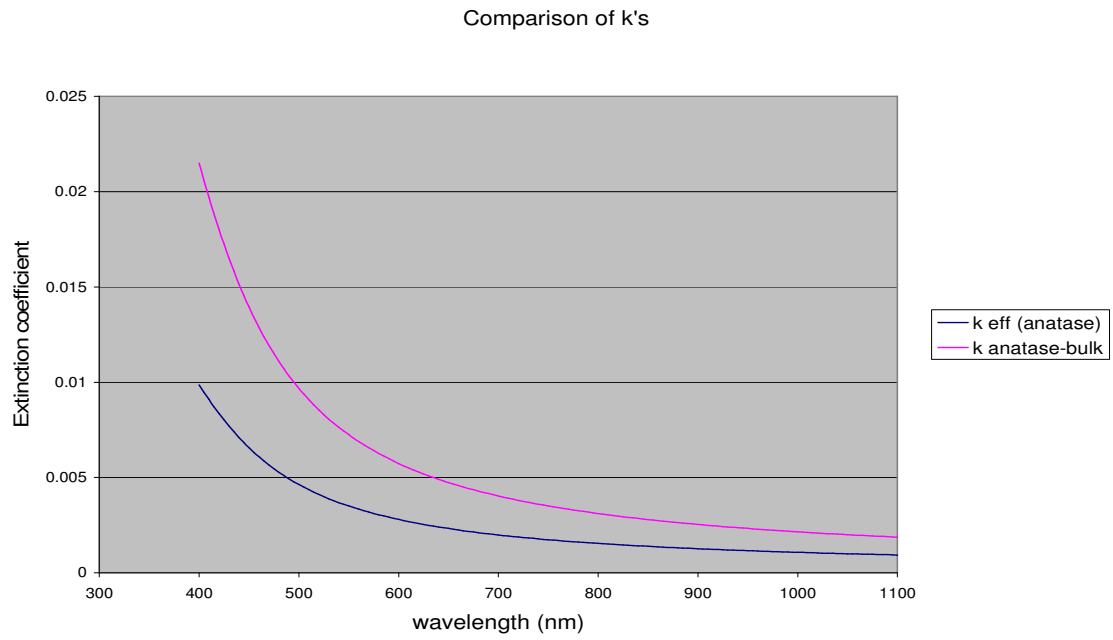

Fig. 1.4. n and k of pure anatase titania and EMA mixture of 1/3 void and 2/3 pure anatase titania.

The ellipsometry program fits the fraction of void space in the film and the film's thickness based on the EMA model and the optical properties of the two constituents of the film.

2) **The Cauchy model.** This model assumes the coefficient of extinction to be zero and the following dependence of the refractive index on wavelength:

$$n(\lambda) = A + \frac{B}{\lambda^2} + \frac{C}{\lambda^4} \qquad \text{(Eq. 1.9)}$$

where the parameters A, B, and C are the fitting parameters of the model. This is a good model for dielectric films with photon energies below the bandgap, but becomes inaccurate when the film has non-zero losses as seems to be the case with our films.

3) **The Lorentz model**, which, although more complicated than the first two, seems to be more suitable since it accounts for absorption[5]. This model assumes that energy dependence of the complex dielectric constant has the form:

$$\varepsilon_{complex} = \varepsilon_1 + \frac{AE_c}{E_c^2 - E^2 - iBE} \qquad \text{(Eq. 1.10)}$$

where ε_1, A, B, E_c, and the film thickness of are the fitting parameters and E is the energy of the incident photons: $E = hc/\lambda$. The parameters ε_1, A, B, and E_c are assumed to be real and positive. EMA also accounts for absorption but the Lorentz model turned out to be more suitable for films such as these since it provided us with better fits. The predicted refractive index n and extinction coefficient k versus inverse wavelength are shown in Fig.1.5. For this plot the values of the fitting parameters were chosen as $\varepsilon_1 = 1.13$, A = 1.2, B = 0.5, and $E_c = 3.46$. These values are actually the average values of the better films of the seventh set of titania films that will be discussed in Section 4.8.

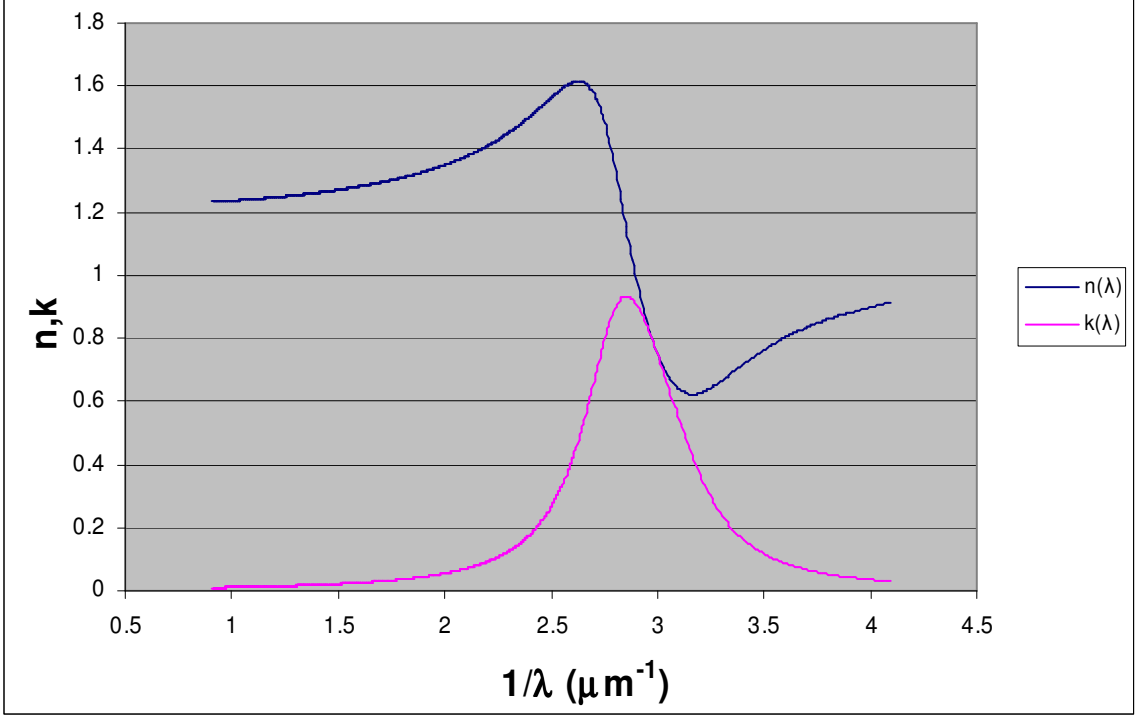

Fig. 1.5. Typical n and k of titania films using the Lorentz model.

It is difficult to model Ellipsometry data when the films are thin and there is significant diffuse scattering. To illustrate the difficulty we faced, the results are shown in Fig. 1.6 of using the three different models, described above, to fit the ellipsometry measurements on one titania film. The green lines represent measured data and the red lines are the best model fit.

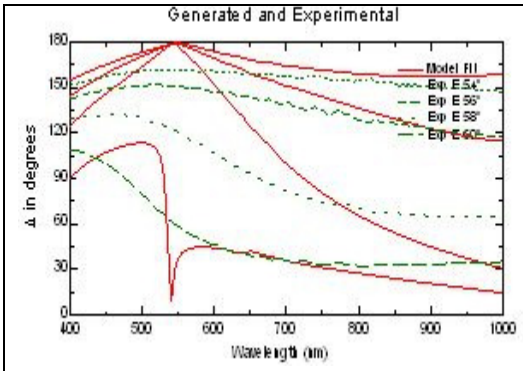

A

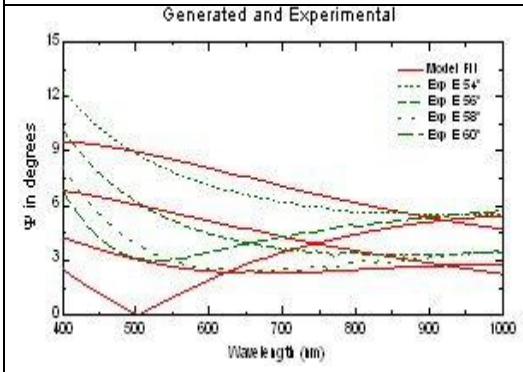

B

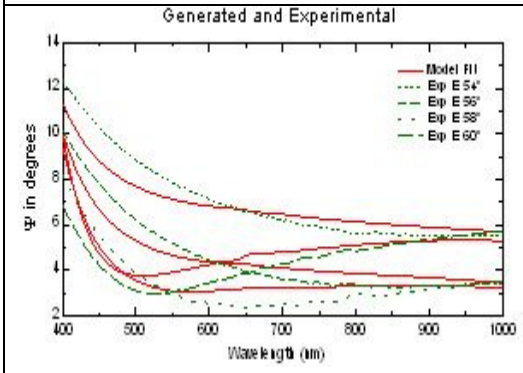

C

Fig. 1.6. Ellipsometry data (green) with model fit (red) for the three different models, EMA (A), Cauchy (B), and Lorentz (C). The Lorentz model shows a better fit.

The Lorentz clearly fits the data better than the EMA and Cauchy models. The kinks observed in the EMA and Cauchy models (which we believe are artifacts of the Brewster angle) are not

removed even when we include extra parameters in the model to represent the experimental angular spread of the incident light and possible grading of the index of refraction near the surface. The presence of too many fitting parameters is not a desirable course since any data can fit any model given enough fitting parameters. Even with the inclusion of angular spread and index grading, the unphysical features in the model fits are smoothed out but not removed. The Lorentz model provides a reasonable fit to the data and does not have the unphysical features and for these reasons we will use it to model the optical properties and the thicknesses of our films. Some additional considerations about the Lorentz model and losses due to diffuse scattering and absorption are found in Section 1.2.4 below.

1.2.4 Absorption and Diffuse Scattering

Fig. 1.7 shows our experimental setup for measuring the reflected and transmitted intensities for normal incidence where I_0, t, r, a, s are the incident, transmitted, reflected, absorbed, and scattered intensities respectively. By energy conservation

$$I_0 = t + r + a + s$$

Dividing through by I_0 we obtain

$$1 = T + R + A + S$$

where T, R, A, and S are the transmittance, reflectance, absorbance, and diffuse scattering fractions, respectively. Of these quantities, T and R are measured directly. If the films are dielectrics, then A is negligible for photon energies less than the bandgap. Solving then for S we obtain

$$S = 1 - R - T$$

which will serve as our definition for the diffuse scattered intensity.

There are two mechanisms for losses to occur, diffuse scattering and absorption. We have no way of distinguishing between the two in the sense that we cannot assign a definite percentage of the losses to scattering and to absorption. Hence scattering and absorption are treated as one mechanism only. It should be noted here though that for long wavelengths, and hence photon energies below the bandgap, absorption is negligible and all loss can be attributed to diffuse scattering.

Light is scattered diffusely from inhomogeneities in the bulk of the film and from surface roughness. The scattered intensity for a given wavelength is related to the Fourier component of

the respective bulk inhomogeneities or the surface roughness. The Fourier analysis of the surface roughness (measured by AFM) is discussed in Sections 4.6 and 4.8. The wavelength of the Fourier components with the highest magnitude correspond to the wavelength of the incident light that will be scattered most. Those components with wavelengths smaller than the incident wavelength give rise to Rayleigh scattering. The intensity of scattered light in this limit is proportional to $1/\lambda^4$. Scattering of light by those Fourier components whose wavelength is comparable to or larger than the wavelength of incident light is described by Mie Scattering.

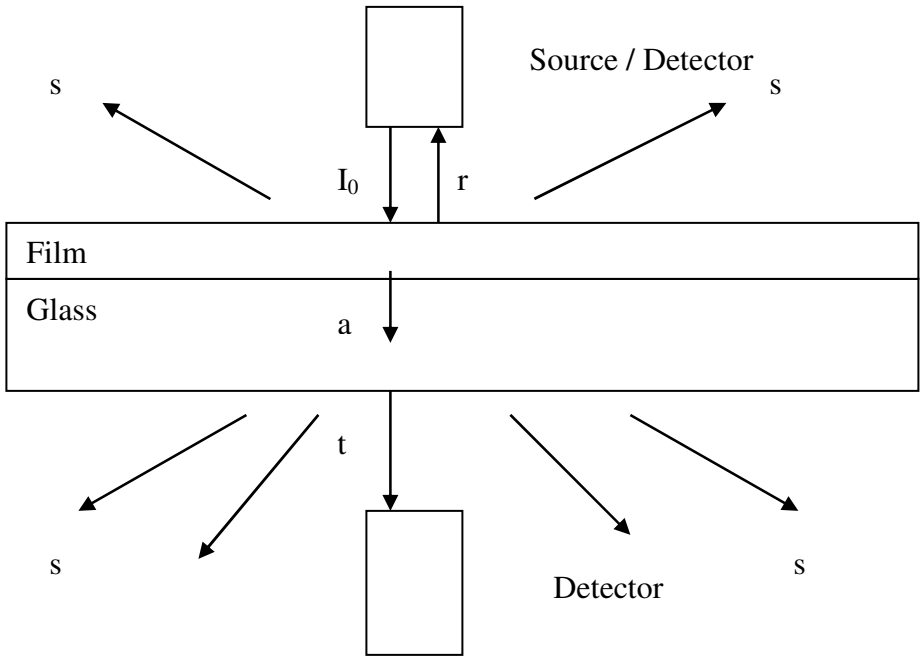

Fig. 1.7. Schematic of different intensities.

An important point relating to the previous section about ellipsometry should be emphasized here. The Lorentz model that we used to analyze our data assumed that the width of the complex dielectric function was independent of photon energy (assuming a narrow peak) which may not be true if the loss of incident intensity is due to diffuse scattering. As a consequence, the results from ellipsometry models regarding refractive indices and film thicknesses have to be taken with caution. The question of how to incorporate diffuse scattering into the model is an interesting one that will be considered next.

At this point it may be instructive to examine the Lorentz ellipsometry model more closely.

Solving Equations 1.5, 1.6, and 1.7 for n and k, one finds

$$n = \sqrt{\frac{\varepsilon_{real} + \sqrt{\varepsilon_{real}^2 + \varepsilon_{imaginary}^2}}{2}} \qquad \text{(Eq. 1.11)}$$

and

$$k = \frac{\varepsilon_{imaginary}}{\sqrt{2\varepsilon_{real} + 2\sqrt{\varepsilon_{real}^2 + \varepsilon_{imaginary}^2}}} \qquad \text{(Eq. 1.12)}$$

Comparing these with Equation 1.10 that gives $\varepsilon_{effective}$ in the Lorentz model we see that the only term that affects the extinction coefficient k is the BE term. This is easily seen since setting B = 0 gives zero imaginary part for $\varepsilon_{effective}$ and hence zero k which means no losses. B is one of the fitting parameters in the Lorentz ellipsometry model and it is taken (just like all other fitting parameters) as constant, or more specifically, wavelength independent. This is reasonable for absorbance near the band edge, but is a very bad approximation for modeling diffuse scattering.

When the photon energy is much less than the band gap, (long wavelength), the diffuse scattering is given by the Rayleigh expression

$S = c_1 E^4$ where E = hν

where c_1 is a constant. If the loss of incident intensity is due to absorbance, then we can write

$A = (1 - e^{-2kx}) \approx 2kx$ for thin films,

and consider the limits x → 0 and x → ∞, where k is the extinction coefficient given by Equation 1.12, and x is the thickness of the film. Since for long wavelengths the absorbance is negligible and since the Lorentz model does not make a distinction as to the loss mechanism, we can equate the right hand sides of these two equations. Now if diffuse scattering is strictly a surface effect and the bulk of the film does not contribute to it at all, then c_1 should be independent of x. If diffuse scattering occurs in the bulk of the film as well as the surface we can assume that c_1 is proportional to x. With these considerations and after some algebra we obtain

$$k_{effective} = \begin{cases} \dfrac{1}{2x}\left(\dfrac{E}{c}\right)^4 \\ \\ \dfrac{1}{2\chi}\left(\dfrac{E}{c}\right)^4 \end{cases} \qquad \text{(Eq. 1.13)}$$

where c and χ are constants with dimension of energy and length respectively. The first equation corresponds to the case where diffuse scattering occurs only at the film surface and the second equation to the case where diffuse scattering is a film bulk effect. In both cases the extinction coefficient is proportional to the fourth power of the energy. It can be shown that if the parameter B in the Lorentz model equation for $\varepsilon_{effective}$ is constant, then the extinction coefficient will not be proportional to E^4. In order to reconcile these two equations, we write the term B*E in the denominator as a power series in E:

$$BE = \sum_{n=0}^{\infty} c_n E^n$$

Since we are considering the limit of long wavelengths we can assume that

$$n = \sqrt{\varepsilon_{real}}$$

and

$$k = \frac{\varepsilon_{imaginary}}{2n}$$

By evaluating the real and imaginary parts of Equation 1.10 for $\varepsilon_{effective}$ and by neglecting the $(BE)^2$ term in the denominator we can expand the resulting expressions in powers of E and equate to the power series equation for BE. The coefficients in that expansion can then be evaluated by equating the result to $k_{effective}$ found in Equation 1.13. We find that the coefficients c_0, c_1, c_2, and c_3 are zero. Thus, we can model diffuse scattering with the Lorentz model if the coefficient B is proportional to E^3. This result provides an interesting future project as a new Lorenz model can be built and incorporated into the ellipsometer software where the parameter B is proportional to E^3. The two different loss processes, absorption and diffuse scattering, are the subject of the next two paragraphs.

1.2.4.1 Absorbance

As we attempted to understand the fall-off in transmittance and reflectance from our titania nanoparticles films at short wavelength, one explanation we considered was that the absorption edge due to the amorphous titania nanoparticles was not sharp and that we were seeing the consequences of the extended edge. In order to explore this possibility, we calculated R and T using the general theory of optically conducting films that can be found in advanced optics textbooks such as Principles of Optics by Max Born and Emil Wolf[6].

In the case of normal incidence, the transmittance and reflectance are given by

$$T = \frac{n_{substrate}}{n_{air}} \frac{\tau_{12}^2 \tau_{23}^2 e^{-2 v_2 \eta}}{1 + \rho_{12}^2 \rho_{23}^2 e^{-4 v_2 \eta} + 2 \rho_{12} \rho_{23} e^{-2 v_2 \eta} \cos(\phi_{12} + \phi_{23} + 2 u_2 \eta)} \quad \text{(Eq. 1.14)}$$

and

$$R = \frac{\rho_{12}^2 e^{2 v_2 \eta} + \rho_{23}^2 e^{-2 v_2 \eta} - 2 \rho_{12} \rho_{23} \cos(\phi_{23} - \phi_{12} + 2 u_2 \eta)}{e^{2 v_2 \eta} + \rho_{12}^2 e^{-2 v_2 \eta} - 2 \rho_{12} \rho_{23} \cos(\phi_{12} + \phi_{23} + 2 u_2 \eta)} \quad \text{(Eq. 1.15)}$$

where,

$$\eta = 2\pi (thickness) / \lambda$$

$$u_2^2 = \frac{n^2 - k^2 + \sqrt{n^2 - k^2 + 4 n^2 k^2}}{2}$$

$$v_2^2 = \sqrt{(n^2 - k^2)^2 + 4 n^2 k^2} - \frac{n^2 - k^2}{2}$$

$$\rho_{12}^2 = \frac{(1 - u_2)^2 + v_2^2}{(1 + u_2)^2 + v_2^2}$$

$$\rho_{23}^2 = \frac{(1.5 - u_2)^2 + v_2^2}{(1.5 + u_2)^2 + v_2^2}$$

$$\tan \phi_{23} = \frac{3 v_2}{u_2^2 + v_2^2 - 1.5^2}$$

$$\tau_{12}^2 = \frac{4}{(1 + u_2)^2 + v_2^2}$$

$$\tau_{23}^2 = \frac{4 (u_2^2 + v_2^2)}{(1.5 + u_2)^2 + v_2^2}$$

It is also assumed that the film is deposited on glass with index of refraction equal to 1.5 and the other medium is air with index of refraction equal to 1.

We use the Bruggeman EMA model to obtain the frequency dependent complex dielectric constant assuming the film is a mixture of titania and void space. The optical properties of titania were obtained from Mardare et al.[4] and described in Section 1.2.3. For void, n = 1 and k = 0. The results for T and R versus 1/λ are shown in Fig. 1.8 based on the assumption that the titania fraction was 0.446 and that the film thickness was 162 nm. These were typical values of void fraction and thickness for our films from set 7 (Section 4.8).

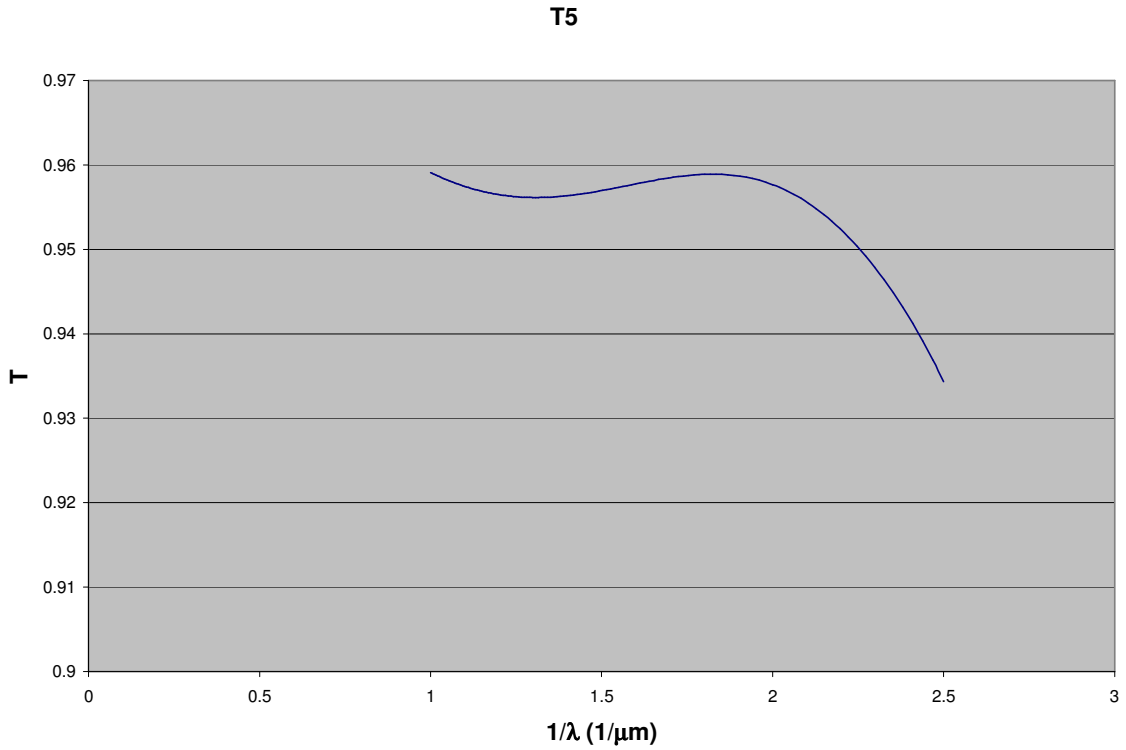

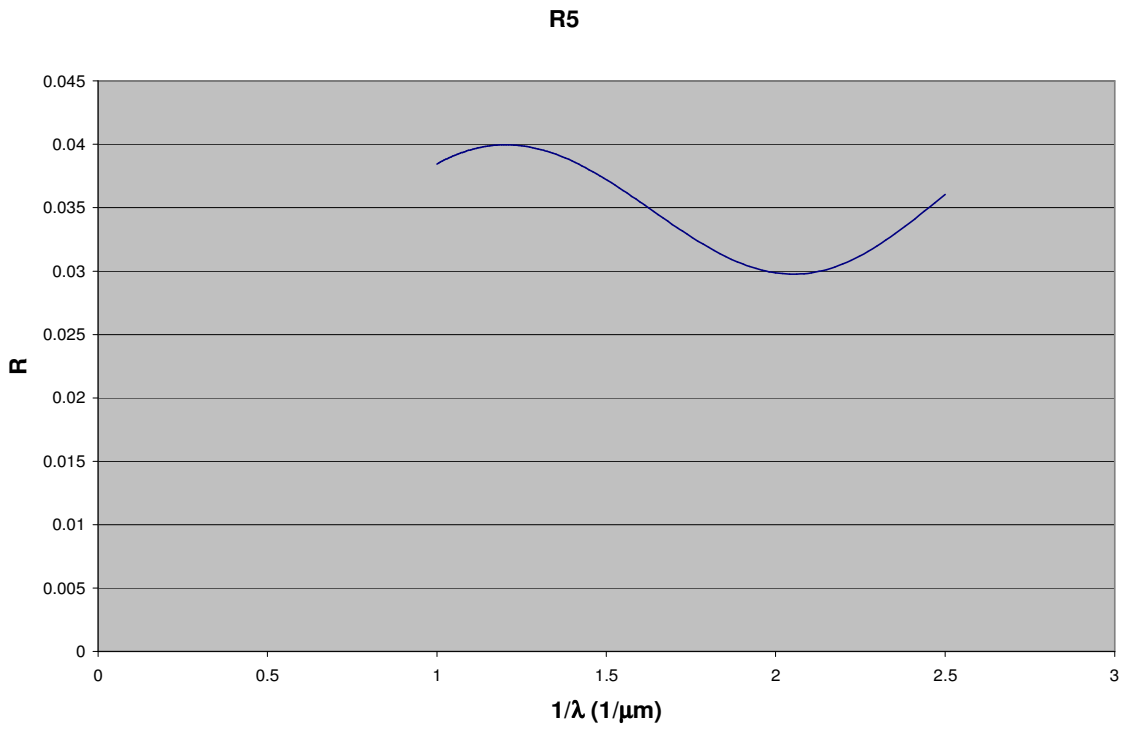

Fig. 1.8. Predicted T and R for film 5 with thickness equal to 162nm and titania nanoparticle fraction equal to 0.446.

1.2.4.2 Diffuse Scattering – Rayleigh and Mie Scattering

As discussed in Section 1.2.4, the dominant diffuse scattering process is **Rayleigh scattering.** When the dimensions of the scattering sources are comparable to λ the scattered intensity is proportional to $1/\lambda^4$. As the wavelength decreases, we enter the Mie scattering regime where light scattering is not described by a simple power law. Fig. 1.9 shows a typical plot of scattered intensity versus $1/\lambda^4$ for four films (25, 26, 27, and, 28) from set 1. It is seen that for $1/\lambda^4$ less than ~ $20\mu m^{-4}$ (corresponding to 470 nm) the line is straight which provides evidence that Rayleigh scattering occurs for those wavelengths. We note that the intercept of the data does not appear to be zero which suggests that true Rayleigh scattering may not be evident until the wavelength of the radiation is in the infrared. Mie scattering is clearly occurring for values of $1/\lambda^4$ greater than ~ $20\mu m^{-4}$.

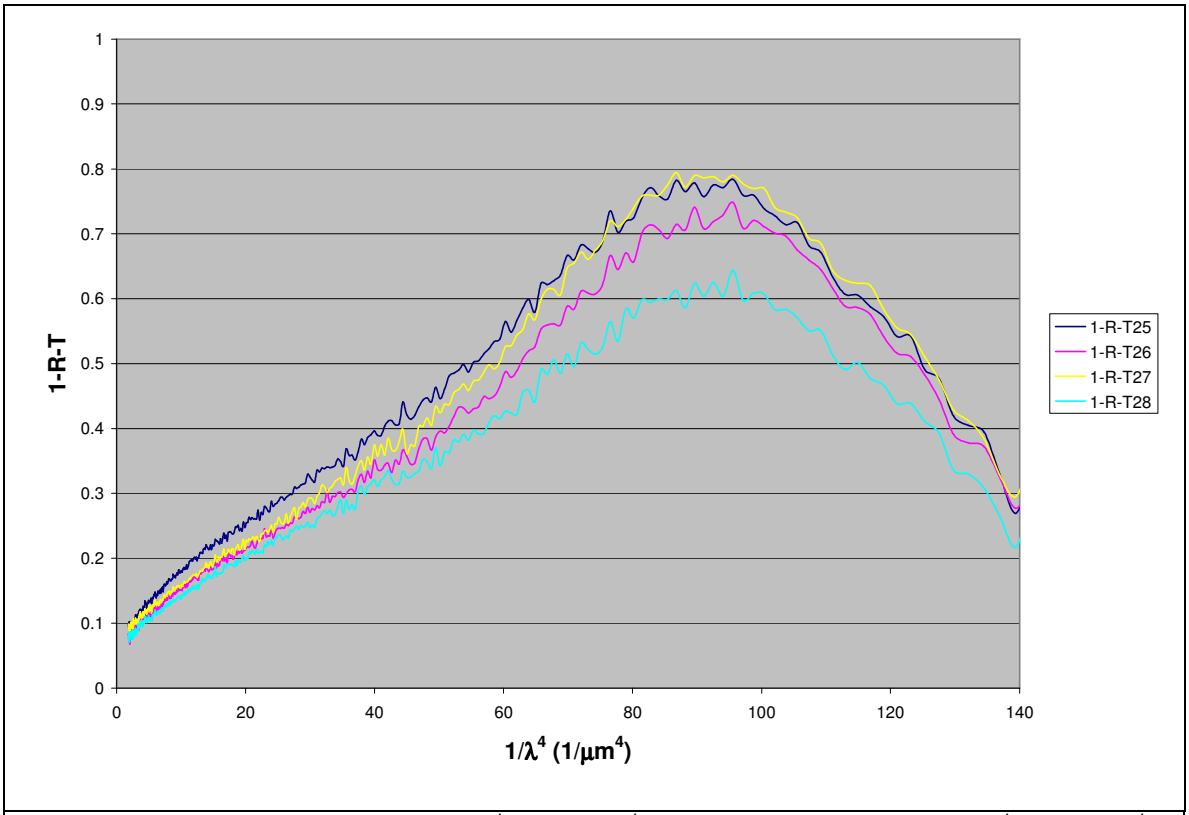

Fig. 1.9. Rayleigh scattering (for $1/\lambda^4 < 20\ \mu m^{-4}$) and Mie scattering (for $1/\lambda^4 > 20\ \mu m^{-4}$).

If the limit of Rayleigh scattering is $1/\lambda^4 = 20\ \mu m^{-4}$, then the characteristic dimension of the inhomogeneity is 500 nm. Fig. 1.10 shows the scattered intensity versus $1/\lambda^4$ for four samples (films 29, 30, 31, and 32 from set 1) in the apparent range of Rayleigh scattering. A linear regression fit to the data is also shown.

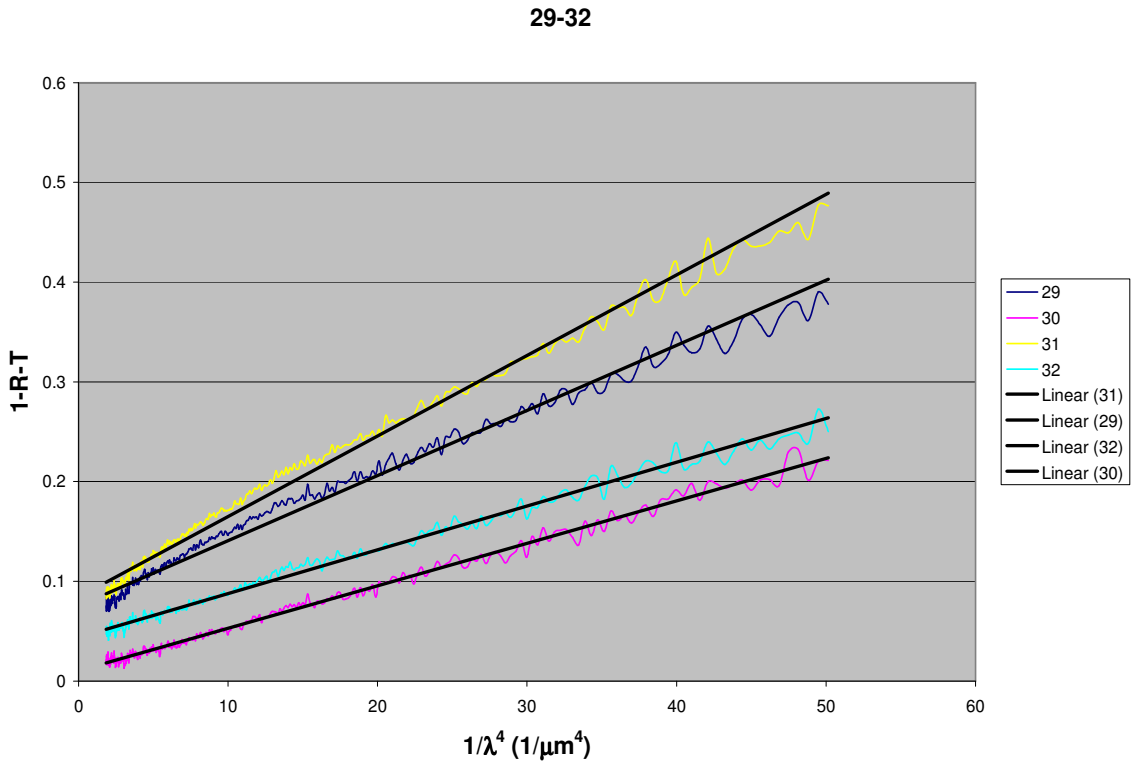

Fig. 1.10. Scattered intensity vs. $1/\lambda^4$ in the Rayleigh scattering region.

We noted that diffuse scattering could be due to a rough film surface or that it could be a film bulk effect. In the case of a bulk effect the scattered intensity depends on film thickness whereas in the case of surface scattering, the scattered intensity is independent of film thickness. That the surface is rough is evident from the SEM images shown in Fig. 1.11 A and B for titania nanoparticles films from an early and a late set, respectively (Sections 4.1 and 4.7). The aggregates shown in Fig. 1.11A are clearly much larger than the putative average diameter of the titania nanoparticles, 35nm. One of the latest films is shown in Fig. 1.11B. The homogeneity is clearly improved from set 1 to set 7 although surface and bulk inhomogeneities are still evident.

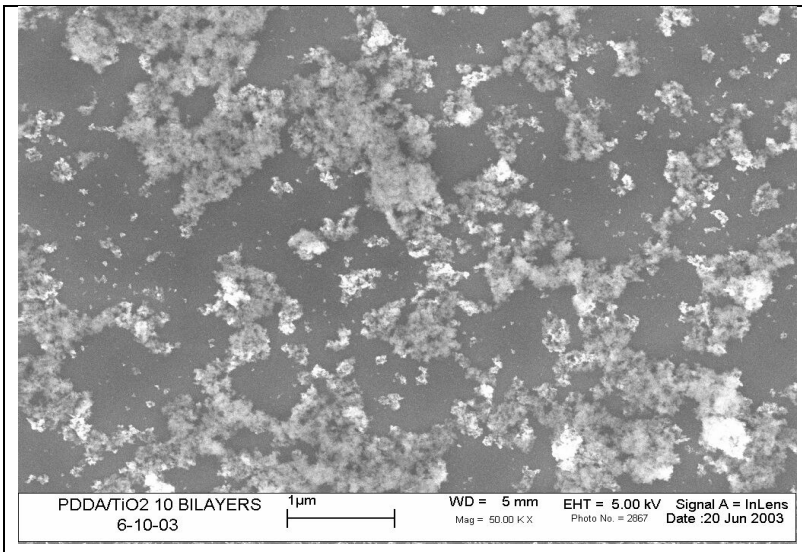

A

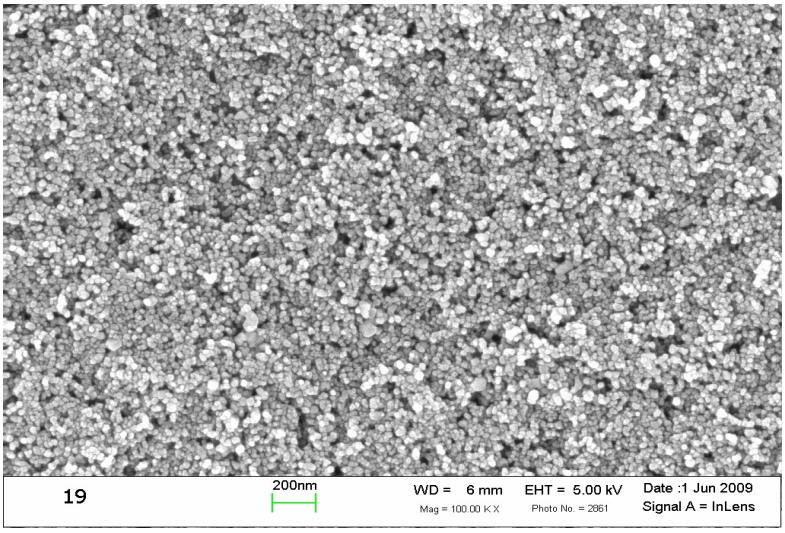

B

Fig. 1.11. SEM images of titania nanoparticles on glass from set 1 (A) and of film 19 from set 7 deposited with centrifugated titania solutions (B). The uniformity of the new film is evident in contrast with the obviously inhomogeneous old film.

Our goal is to optimize the deposition process in order to minimize the diffuse scattering regardless of whether it is a surface or a bulk effect. We will do this using the statistical

techniques of factorial design and response surfaces. We now discuss the deposition technique that we used in this work to produce our films.

1.3 ISAM

Different techniques for depositing thin films are discussed in Chapter 2. Many of the difficulties associated with existing film deposition techniques are avoided by use of a technique called Ionic Self-Assembled Monolayers or ISAM (in the literature this deposition technique is sometimes referred to as layer-by-layer deposition or LbL). ISAM is very simple and inexpensive to perform and does not present difficulties with large and/or non-planar surfaces. It involves alternating dipping the substrate in solutions containing particles or polyions of opposite charge as shown in Fig. 1.12. Electrostatic force between the nanoparticles and polycations are responsible for holding the nanoparticles in place. The substrate is washed with DI water between each immersion in order to remove weakly bound particles. The thickness of the film is equal to the number of bilayers (one bilayer is created by each cycle shown in Fig. 1.12) times the thickness of the bilayer. The optical and physical characteristics of the film are governed by the properties of the two constituent materials making up the bilayer. This process is carried out at room temperature and does not require volatile organic compounds.

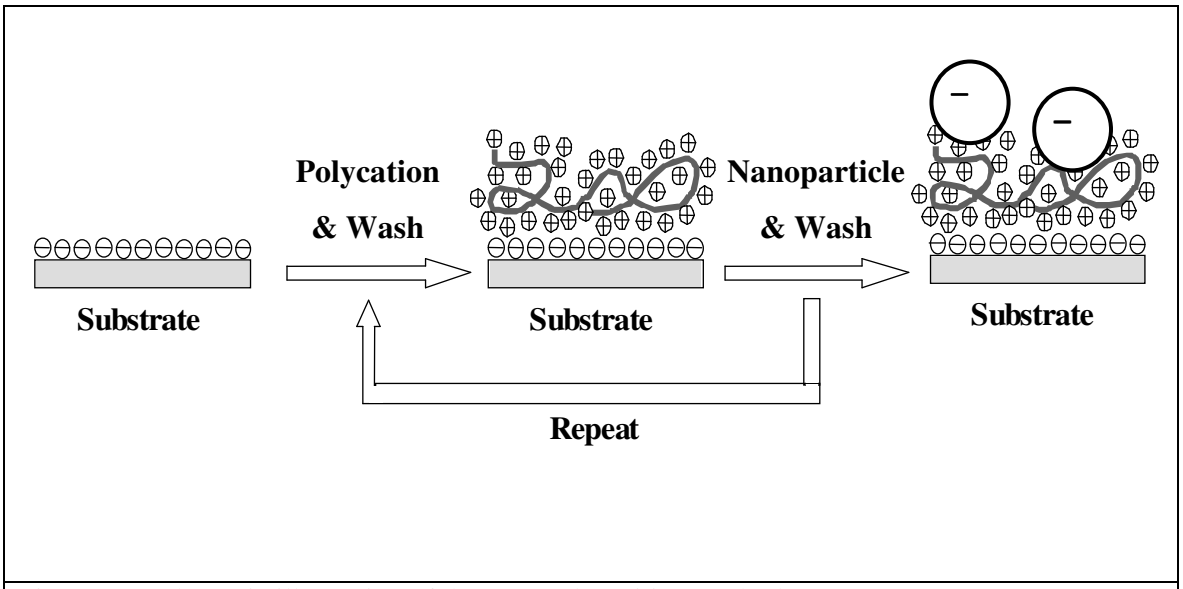

Fig. 1.12. Schematic illustration of the ISAM deposition method.

Our films are deposited on microscope glass slides with part of the film covering the frosted end to facilitate ellipsometry measurements. Glass slides have to be processed before deposition by a procedure called RCA cleaning. This involves three steps:

1. Macroscopic cleaning of the slide with acetone and kim-wipes.
2. Immersion of the glass slides for 20 minutes in a strong basic solution consisting of 6 parts de-ionized water (DI), 2 parts hydrogen peroxide, and 1 part ammonium hydroxide.
3. The temperature of the basic solution must be kept between 75 and 85 ^{0}C. This step removes organic materials from the glass surface.
4. Immersion of the glass slides for 20 minutes in a strong acidic solution consisting of 6 parts de-ionized water (DI), 2 parts hydrogen peroxide, and 1 part hydrochloric acid. This solution is kept at room temperature. This step removes heavy metals from the glass surface.

Between the last two steps, as well as after the final step, the glass slides must be thoroughly washed with DI water. At the end the slides are dried with nitrogen gas. It is very important that in no step of this procedure the slides are allowed to air-dry. The first step of the macroscopic cleaning is very important. If it is not done correctly, the glass slides emerge opaque and therefore, are not usable. It is also critical to use premium microscope glass slides rather than "standard" to obtain uniform films. For one set of the titania experiments we investigated a different macroscopic cleaning procedure. Instead of scrubbing the slides with kim-wipes and acetone we immersed the slides into an acetone sonic bath for 20 minutes per side. This is described in more detail in section 4.6.1.

In addition to removing impurities, RCA cleaning leaves the glass surface negatively charged. Having established the negative charge on the glass surface, the first step of ISAM is immersion of the glass slide in a solution of polycations. In this work, we experimented with two different polycations: Poly(allylamine hydro-chloride) (PAH) and Poly(diallyldimethylammonium chloride) (PDDA). After immersion, the slide is washed with DI water and then immersed into a colloidal solution of either titania or silica nanoparticles. This completes one bilayer. The isoelectric points of the titania and silica[7] nanoparticles that we used were pH = 6.5 and pH = 2, respectively. The process can be continued for as many cycles as necessary to generate the desired thickness. Finally, when the desired number of bilayers has been deposited and the process is complete, the film must be dried with nitrogen gas, labeled,

and stored in a slide holding box. Again, just as with RCA cleaning the slides must not be allowed to air-dry at any point of the ISAM process.

Before continuing with further considerations about antireflection coatings and the associated diffuse scattering we review in Chapter two some of the literature on this subject including various techniques of film deposition.

References for Chapter One

1 Eugene Hecht, *Optics*. (Addison Wesley, 2002), Fourth ed.

2 J. E. Sipe and R. W. Boyd, "Nonlinear Susceptibility of composite optical - materials in the Maxwell Garnett model," Phys. Rev. A **46** (3), 1614-1629 (1992).

3 T. Furukawa, K. Yasuda, and Y. Takahashi, "Dielectric and conductive spectra of the composite of barium titanate and LiClO4-doped polyethylene oxide," Ieee Transactions on Dielectrics and Electrical Insulation **11** (1), 65-71 (2004).

4 D. Mardare and P. Hones, "Optical dispersion analysis of TiO2 thin films based on variable-angle spectroscopic ellipsometry measurements," Materials Science and Engineering B-Solid State Materials for Advanced Technology **68** (1), 42-47 (1999).

5 Frederick Wooten, *Optical Properties of Solids*. (Academic Press, 1972).

6 Max Born and Emil Wolf, *Principles of Optics*. (Cambridge University Press, 1999), Seventh ed.

7 Teofil Jesionowski, "Influence of aminosilane surface modification and dyes adsorption on zeta potential of spherical silica particles formed in emulsion system," Colloids and Surfaces A: Physicochemical and Engineering Aspects **222** (1-3), 87-94 (2003).

CHAPTER TWO

Literature Review

2.1 Deposition of Thin Dielectric Films by ISAM for Optical Coatings

ISAM deposition has been done since the 60's but did not become a widespread technique until the 90's. The first publication of silica nanoparticle deposition to form films was from Iler[1] in 1966. In his study Iler introduces the deposition of negatively charged silica particles on glass substrates with colloidal alumina used as the counterion. Since then, alternate deposition of oppositely charged particles and polymers is a subject that has been explored extensively. The different applications of these ISAM films include photovoltaic applications, antireflection films, photocatalytic properties leading to applications such as self cleaning films, antifogging films, purification of water, and purification of air[2,3,4,5]. The review provided by Richards[2] included many such applications and properties of titania, silica and CeO_2 that include AR coatings, photocells, and film strength and endurance. He also discussed ISAM deposition of optical films with various possible dielectric materials. The review by Ariga et al.[3] also provided a very extensive account of different deposition techniques with reference to various combinations of organic and inorganic materials both as substrates and films. An earlier review publication from Ariga et al.[4] focused on ISAM and its simplicity and low cost relative to other techniques. The appropriateness of this technique for charged nanoparticle deposition is one more advantage. One of the earlier reviews is from Decher.[5] ISAM was described along with its advantages such as simplicity, speed, and the large number and types of materials that can be deposited by it such as polymers, proteins, and nanoparticles.

2.2 Alternative Techniques to ISAM Deposition

The majority of this thesis is about titania nanoparticle deposition by ISAM. Other common approaches for thin film deposition are spin coating, vacuum chamber evaporation, and sputter deposition. ISAM offers a number of advantages, notably its simplicity in terms of required equipment as well as applicability to surfaces of various sizes and shapes and its low cost compared to the other techniques mentioned above. Vacuum evaporation of optical thin films has been reviewed by Martin[6]. Vacuum chambers are considerably more expensive than

equipment required for ISAM deposition and the optical properties of the deposited materials can change when they are taken from the vacuum chamber. Another disadvantage of this technique is that the process takes place at high temperatures which can damage the film and the substrate. The vacuum chamber itself limits the size and shape of the substrate.

The spin coating technique has been reviewed by Ariga et al.[4] In this paper they described this method as an efficient way of depositing thin films for applications that exploit the photocatalytic properties of titania. Spin coating involves dropping the coating material on a rotating substrate with the resulting film thickness dependent on the viscosity of the coating material and the angular velocity of the substrate. An advantage of the technique is that weakly bound polymers are removed from the substrate and at the same time the deposition of the more strongly bound polymers occurs uniformly. Organic solvents are needed for spin coating whereas ISAM only requires water. This is a major environmental benefit of ISAM.

Pederson et al.[7] have reviewed the sputtering technique for thin film deposition. This technique is primarily used for depositing high melting point metals and dielectrics with a modest deposition rate, which depends on the target material, of approximately 1μm/hour. The technique is preferable to vacuum evaporation for target materials that are difficult to melt, but it still requires a vacuum chamber limiting its application to relatively small planar substrates.

The advantage of ISAM over spin coating, vacuum evaporation, or sputtering, is its simplicity as well as its applicability to large, non-planar surfaces. The disadvantage of using ISAM is a possible difficulty with the film's thickness and optical properties.

2.3 Possible Dielectric Nanoparticles

Various possible dielectric nanoparticles are summarized in Table 2.1. The deposition of silica and titania nanoparticles will be discussed in more detail in Section 2.5 . Silica and titania have the largest contrast in refractive indices ($n_{silica} = 1.4$, $n_{titania} = 2.5$) at 500 nm. The band gaps of anatase titania and silica are 3.2eV[8] and 5eV[9] respectively. The small band gap of titania limits the range of optical wavelength that we can use. For completeness we will discuss other dielectric materials that have been deposited as thin films. These materials include zirconia (ZrO_2), alumina (Al_2O_3), hafnia (HfO_2), yttria (Y_2O_3), tantalum pentoxide (Ta_2O_5), and niobia (Nb_2O_5) with refractive indices of 1.92, 1.84, 1.88, 1.81, 2.1, and 2.28 respectively. In addition we list the band gaps which specify the cut-off wavelength.

Tanner et al.[10] reported that the refractive indices for ZrO_2 and HfO_2 at 633nm are 1.92 and 1.88 respectively at room temperature. The variation of these values with temperature is less than a few percent. Stadler et al.[11] found that the refractive index of **mixtures of yttria and alumina** at 633nm is 1.84. The value given corresponded to a mixture of 84.4% yttria and 15.6% alumina. Ozer et al.[12] reported the index of refraction of **niobia** to be 2.28 at 530nm for temperatures below 450^{o}C. They also found that the extinction coefficient of niobia is $4x10^{-3}$ at 530nm. Haanappel et al.[13] reported that the value for the refractive index of their alumina films at 290^{o}C is 1.53. They measured the index of refraction and found that there is a small increase from 1.53 to 1.6 over temperatures ranging from 290 to 420^{o}C. The data did not follow a recognizable pattern but there seems to be a discontinuity between 330 and 370^{o}C indicating a possible change in crystalline structure. Xu et al.[14] reported the index of refraction of **yttria** to be 1.9 at 500nm. Chaneliere et al.[15] studied vacuum evaporated **tantalum pentoxide** films and found that the refractive index was 2.1 at 590nm. Patsalas et al.[16] reported that the index of refraction of CeO_2 is 2.2.

Table 2.1 is a summary of these facts along with the appropriate reference for each value given.

Dielectric (bulk)	Refractive index	Band gap (eV)
TiO_2 (anatase)	2.5[17] at 500 nm	3.2[8]
TiO_2 (rutile)	2.6[17] at 500 nm	3.0[18]
TiO_2 (brookite)	2.64[19] at 500 nm	3.1[20]
TiO_2 (amorphous)	2.4[17] at 500 nm	3.3[8]
SiO_2	1.4[2] at 500 nm	5.0[9]
ZrO_2	1.92[10] at 633 nm	5.5[21]
HfO_2	1.88[10] at 633 nm	5.5[8]
Nb_2O_5	2.28[12] at 530 nm	3.3[22]
Al_2O_3	1.84[11] at 633 nm	8.0[23]
Ta_2O_5	2.1[15] at 590 nm	3.9[24]
CeO_2	2.2[16] at 500 nm	3.6[25]
Y_2O_3	1.81[14] at 500 nm	4.5[14]

Table 2.1. Refractive indices and band gaps of various dielectrics that can be used as AR coatings.

2.4 ISAM Deposition of Silica Nanoparticle Films

The deposition and characterization of silica nanoparticles films has been discussed in several papers[1,26,27,28,29]. Since a silica layer is in the quarter wave stack, because of the large refractive index contrast between SiO_2 and TiO_2 a brief overview is given here of silica film deposition. Under some deposition conditions, silica nanoparticle films have been constructed with silica fractions equal to 0.6 which is close to the complete random close packing fraction for spherical particles of 0.63[26]. Several other studies have focused on the effect of nanoparticle size on film homogeneity and optical properties[27,28] with some conflicting results. It was seen by Ahn et al. and Bogdanovic et al. that the first few layers were formed with higher uniformity for nanoparticles with diameters less than 100nm meaning that the nanoparticles distributed themselves more evenly on the substrate.

Lvov et al.[30] studied how dip time influenced the distribution of silica nanoparticles (45nm diameter with colloidal pH = 9.5) on glass substrates using PDDA as the polycation. They measured the film thickness by ellipsometry, using the Lorentz model, as well as by analysis of

cross-sectional SEM images and found that islands of silica nanoparticles formed within 2 seconds in the colloidal solution and then growth of the layer (filling in between islands) proceeded far more slowly. The initial PDDA layer formed in 20 seconds. They followed the film growth over a period of 15min.

The majority of the results that we will use for the silica component of our quarter wave stacks can be found in Yancey et al[29]. They studied films prepared with 15 nm, 45 nm, and 85 nm average diameter nanoparticles. The index of refraction was 1.36 for films prepared with 15nm diameter nanoparticles and the diffuse scattering increased with increasing nanoparticle diameter. As a consequence of these results we used the 45 nm silica nanoparticles to prepare our films. In the same study it was found that for nanoparticles of diameters equal to 15nm, 45nm, and 85nm the film thickness increases linearly with the number of bilayers. Diffuse scattering was found to be independent of film thickness and hence attributed as a surface phenomenon. The pH values used in this study varied between 7 and 11. Diffuse scattering and the optical properties of the films were seen to be fairly independent of pH.

2.5 ISAM Deposition of Titania Nanoparticle Films

In this section we review ISAM techniques for depositing titania nanoparticle films which has been a field of research since the mid 90's. Much of this research is directed towards application of titania nanoparticle films for anti-fogging as well as for film self cleaning taking advantage of the photocatalytic properties of titania nanoparticles, to break down organic waste[31]. Titania nanoparticles films also can function as the n-type layer in photovoltaic devices. Titania is also heavily used as a whitener in such disparate products as paint, toothpaste, cosmetics. But in these products, the particles are typically a fraction of a micron in diameter.

A study by Caruso et al.[32] used the LbL technique to coat micro-size polystyrene spheres with alternating layers of PAH and titania nanoparticles. The polystyrene was removed by heating. These titania spheres are too large to be considered as nanoparticles but the techniques used for coating them are applicable to our research. They experimented with different pH values, making the titania nanoparticles either positively or negatively charged, and reported an average bilayer thickness of 30nm. They also presented SEM images of the surface showing the problem of particle aggregation in solution and the resulting surface roughness. They concluded

that the LbL technique is an effective method for coating polystyrene spheres with titania nanoparticles.

Bertino et al.[33] used ISAM to produce films of titania nanoparticles that had been functionalized with a dye. They demonstrated, using SEM images and ellipsometry, that irradiating these films with green and UV light reduced the volume of the void spaces between nanoparticles and hence increased the refractive index of the film. They attributed the reduction of void fraction in the radiated films to the photodissociation of the organic dye. Their results were the same for green light and UV light within experimental error. They pointed out that similar results can be obtained by heating the film to a temperature just below the melting point (calcination), but for microelectronic applications, this calcination step can have negative effects on other components on a chip.

Wang et al.[34] investigated titania nanoparticle films constructed by ISAM, and described the process in considerable detail. This paper can serve as a good introduction to the process. Their purpose was to demonstrate that ultra-thin films of titania nanoparticles can be constructed by ISAM for applications such as photovoltaics where good thickness control is essential. Their Titania nanoparticle solutions were in the acidic pH range which gave them a positive surface charge density. In their work they considered dip time and titania molarity as factors for controlling film thickness and reducing absorption. They measured film thickness by ellipsometry and observed a linear dependence of film thickness on number of bilayers. In their paper there is no mention of film refractive indices or diffuse scattering but instead they attributed all loss to absorption. This study concluded that absorption at 228nm increased linearly with the number of bilayers.

The motivation in these studies was not to create an antireflection coating, but, as noted above, to increase the efficiency of photovoltaic devices and to exploit the photocatalytic properties of titania for self cleaning films, water purification devices, and antifogging films[35]. Secondary concerns in these studies were high film strength, heat tolerance, uniformity in the nanoparticle distribution and control over the thickness and refractive index of the film. Regardless of the researchers' motivation for their studies, many general results about film construction were reported that are useful for our purposes, such as film thickness dependence on deposition parameters such as pH.

2.6 Broadband Antireflection Coatings by Graded Index Films and Quarter-Wave Stacks

2.6.1 Graded Index of Refraction

One way of constructing broad band antireflection coatings is with a graded index of refraction. This technique is described by Southwell et al.[36,37] The index of refraction of a graded index film varies continuously from the index of refraction of air to the index of refraction of the substrate. The graded index depends on thickness according to the following quintic formula

$$n(x) = n_{air} + (n_{substrate} - n_{air})\left[10\left(\frac{x^3}{T^3}\right) - 15\left(\frac{x^4}{T^4}\right) + 6\left(\frac{x^5}{T^5}\right)\right] \qquad \text{(Eq. 2.1)}$$

where T is the film thickness, x is the distance coordinate whose origin is at the air/film interface, n_{air} is the index of refraction of air, and $n_{substrate}$ is the index of refraction of the substrate. If the substrate is glass, then $n_{substrate}$ is usually set equal to 1.5. n_{air} is always set equal to 1.

An experimental realization of the above theory has been carried out by many researchers[38,39,40]. The proper variation in the index of refraction was achieved by use of the phenomenon of capillary condensation, which is a usually undesirable side-effect of titania nanoparticle films. Capillary condensation is the phenomenon of fluid trapped in the spaces between nanoparticles being less likely to evaporate near the substrate than near the film/air interface. They succeeded in broadening the region of low reflectance but they did not compare their results with a model calculation of the reflectance spectra.

In their study, Zhang et al.[38] attempted to create a graded index of refraction by using ISAM to deposit a PDDA/SiO_2 layer of silica nanoparticles (200nm diameter) followed by spin coating of sodium silicate on top. They found that the capillary phenomenon reduced the effectiveness of the films. They presented a transmission plot that shows a region of broadband antireflection but did not compare their experimental measurements to model calculations.

Kuo et al.[40] did an interesting study on another experimental realization of the graded index of refraction by depositing a mixture of both silica and titania nanoparticles and taking advantage of the resulting void fraction. They formed the high refractive index layers using titania, the medium refractive index layers using a mixture of silica and titania, and the low refractive index

layers using only silica. The refractive index of their film at the air/film interface was claimed to be 1.09, based on Ellipsometry measurements, presumably due to the very high void fraction at that interface. But there are no SEM images of the films included and details were not provided for how they modeled the ellipsometry measurements.

2.6.2 Quarter-Wave Stacks

There are examples of quarter-wave stacks in nature; iridescence, by which many species achieve their vivid colors, being a prime example. The theory of quarter wave stacks is discussed in section 1.2.2. The following papers used ISAM to create quarter-wave stacks[41,42,43,44] . For example Wu et al.[41] showed that deposition of a quarter wave stack is possible by forming the low refractive index layer using 7nm diameter silica nanoparticles and the high refractive index layer by using 4nm diameter titania nanoparticles. They calcinated some of their films and compared average bilayer thickness, refractive index at 633nm, porosity, and percent volume of polymers for films with and without calcination. All quantities except percent volume of polymer were found to be slightly affected by calcination. The polymer was completely removed after calcination. They called their films Bragg stacks, rather than quarter-wave stacks, in order to emphasize the theoretical analogy with Bragg diffraction. They compared their obtained measurements of reflectivity with the theoretical values obtained by models derived using the characteristic matrices of the materials. Good agreement between measured data and theoretical calculations was reported.

Kanta et al.[42] investigated quarter wave stacks deposited on silicon wafers by ISAM with the purpose of controlling film thickness to obtain the optical properties they desired. One of the two layers consisted of silica nanoparticles of 40nm diameter and the other one of titania nanoparticles also of 40nm diameter. They demonstrated that complete coverage of silicon wafers as substrates by titania nanoparticles is possible as well as complete coverage of titania substrates by silica nanoparticles. They used AFM images to show this but did not compare the measured optical properties with model calculations.

Lee et al.[43] created a broadband antireflection coating by using ISAM to deposit alternating layers of silica nanoparticles (putative diameter equal 7 nm or 22 nm) and titania nanoparticles (putative diameter equal 7 nm) deposited either on a glass or silicon substrate without the use of polycations. They pointed out that their films did not fog due to the hydrophilicity of the

nanoparticles and, thus, would be useful in coating windows. It was suggested, but not investigated, that low temperature calcination could increase the strength of their films. They said that the colloidal solution for the titania nanoparticles had a low pH in order to obtain a positive surface charge, but did not give the pH. Nor were the deposition conditions for the silica nanoparticles given other than to say that the surface of the silica nanoparticles was negatively charged. The thickness and refractive index of each layer was measured by ellipsometry. The thickness per bilayer increased linearly with the number of bilayers and depended on the pH of the colloidal solutions. The refractive indices were independent of the number of bilayers which indicated that the nanoparticles were uniformly distributed throughout the film. They did not measure absorption or diffuse scattering and found that the transmittance of the coated slides displayed a broad maximum between 400 and 800nm. They compared the transmittances of their films with the transmittance of a clean glass slide. They also measured surface roughness and reported that the RMS roughness of their films (obtained by AFM imaging) was approaching a constant value with increasing film thickness. This value was reported to be different for each set of nanoparticle diameters but no actual value was given. The same group, Lee et al.[44] investigated in a later study the effect of pH on film parameters such as thickness and index of refraction. Their films were again all nanoparticle thin films consisting of one layer of titania nanoparticles and one layer of silica nanoparticles with the pH of titania kept under 3 so that the titania nanoparticles were positively charged. The titania and silica nanoparticles had putative diameters of 7nm and 22nm, respectively. The films were deposited on glass slides using a dipping machine and a linear dependence was observed between the film thickness and the number of bilayers. They characterized their films by ellipsometry using the Cauchy model to obtain the thicknesses and indices of refraction of the individual layers. The reported indices of refraction were 2.29 and 1.45 for the titania and the silica layer, respectively, with total film thicknesses ranging from 25 to 250nm. The values for the refractive indices were considerably higher than the ones we have found repeatedly. This may be attributed to the fact that their nanoparticles were much smaller in diameter than ours which favors more densely packed nanoparticles resulting in higher refractive indices. Since they used the Cauchy model to analyze their ellipsometry measurements, they did not take absorption or diffuse scattering into account.

In conclusion, the approach for creating a broadband antireflection coating by ISAM comes down to a choice between the quarter-wave stack and the graded index of refraction. One could conceivably obtain a graded index by using a mixture of silica and titania nanoparticles in each layer, but it would be difficult to approach an index of one at the air/film interface and the mixture of two different nanoparticles in each layer probably would create significant diffuse scattering. So at this time, it appears that the quarter-wave stack is the best approach for creating a broadband AR coating.

2.7 Nanoparticle Island Formations During ISAM Deposition. Surface Roughness.

ISAM involves the successive deposition of layers of nanoparticles. The first layer of nanoparticles consists of islands of nanoparticles interspersed over the substrate. The empty spaces between islands fill in with successive deposited layers[45]. This phenomenon is clearly seen in SEM images. It is also evident in plots of film thickness versus the number of bilayers; the dependence is linear, but the intercept is not zero. This film growth behavior gives rise to a rough surface that, in turn, contributes to diffuse scattering of light. There are few papers on the subject of nonuniformities during ISAM deposition. A concise treatment was provided by Yonezawa et al.[45] In their study they used ISAM to deposit anionic silica nanoparticles of 25nm diameter in colloidal solutions of concentration 100mg/cm^3 and with pH equal to 10. The polycations were PDDA and amphiphile 1 ($C_8AzoC_{10}N^+C_2OH$). The uniformity of nanoparticles coverage was obtained from SEM images for both polycations using dip times of 5s and 20min. For the first layer, there was no dependence between silica nanoparticle uniformity and dip time for either polycation. But amphiphile 1 produced much more uniform layers than PDDA. This was attributed to the higher charge of amphiphile 1 compared to PDDA. The researchers also pointed out that nanoparticle aggregation in the colloidal solutions would also lead to nonuniformities in the films, but there was no further investigation of this claim.

A more extensive study on surface roughness was provided by Lowman et al.[46] In their study they did not use nanoparticles but used ISAM to deposit all polyion films using PAH, Poly(ethyleneimine) (PEI), and Poly(sodium p-styrenesulfonate) (PSS), on glass microscope slides. All of their polyion solutions were 0.02M. They used AFM to quantify surface roughness by assigning a roughness RMS value defined as:

$$rms=\sqrt{\frac{(Z_i-Z_{ave})^2}{N}}$$

where N is the number of sectors in which they divided their images, Z_i is the height of the i-th sector of the image on the z-axis, and Z_{ave} is the average height of the whole image. It was found that this RMS roughness increased linearly with the number of bilayers for the first ten bilayers and then approached an asymptotic value of 4 nm beyond 10 bilayers. Similar results were observed when glass slides were etched to intentionally increase the roughness of the substrate. The same asymptotic behavior of RMS roughness was observed. They concluded that polyelectrolytes have the ability to smooth out rough surfaces.

References for Chapter Two

1 R. K. Iler, "Multilayers of Colloid Particles," Journal of Colloid and Interface Science **21** (6), 25 (1966).

2 B. S. Richards, "Comparison of TiO2 and other dielectric coatings for buried-contact solar cells: a review," Progress in Photovoltaics **12** (4), 253-281 (2004).

3 K. Ariga, J. P. Hill, M. V. Lee, A. Vinu, R. Charvet, and S. Acharya, "Challenges and breakthroughs in recent research on self-assembly," Science and Technology of Advanced Materials **9** (1) (2008).

4 K. Ariga, J. P. Hill, and Q. M. Ji, "Layer-by-layer assembly as a versatile bottom-up nanofabrication technique for exploratory research and realistic application," Physical Chemistry Chemical Physics **9** (19), 2319-2340 (2007).

5 G. Decher, "Fuzzy nanoassemblies: Toward layered polymeric multicomposites," Science **277** (5330), 1232-1237 (1997).

6 P. J. Martin, "Ion-based methods for optical thin-film deposition," Journal of Materials Science **21** (1), 1-25 (1986).

7 L. R. Pederson, P. Singh, and X. D. Zhou, "Application of vacuum deposition methods to solid oxide fuel cells," Vacuum **80** (10), 1066-1083 (2006).

8 J. Aarik, H. Mandar, M. Kirm, and L. Pung, "Optical characterization of HfO2 thin films grown by atomic layer deposition," Thin Solid Films **466** (1-2), 41-47 (2004).

9 K. Awazu and H. Kawazoe, "Strained Si-O-Si bonds in amorphous SiO2 materials: A family member of active centers in radio, photo, and chemical responses," Journal of Applied Physics **94** (10), 6243-6262 (2003).

10 C. Tanner, K. Geisinger, and R. Wusirika, "Temperature and wavelength dependence of refractive index of zircon and hafhon," Optical Materials **26** (3), 305-311 (2004).

11 B. J. H. Stadler and M. Oliver, "Sputter-deposited yttria-alumina thin films for optical waveguiding," Journal of Applied Physics **84** (1), 93-99 (1998).

12 N. Ozer, M. D. Rubin, and C. M. Lampert, "Optical and electrochemical characteristics of niobium oxide films prepared by sol-gel process and magnetron sputtering - A comparison," Solar Energy Materials and Solar Cells **40** (4), 285-296 (1996).

13 V. A. C. Haanappel, H. D. Vancorbach, T. Fransen, and P. J. Gellings, "Properties of alumina films prepared by atmospheric pressure metal-organic chemical-vapor-deposition," Surface & Coatings Technology **63** (3), 145-153 (1994).

14 Y. N. Xu, Z. Q. Gu, and W. Y. Ching, "Electronic, structural, and optical properties of crystalline yttria," Physical Review B **56** (23), 14993-15000 (1997).

15 C. Chaneliere, J. L. Autran, R. A. B. Devine, and B. Balland, "Tantalum pentoxide (Ta2O5) thin films for advanced dielectric applications," Materials Science & Engineering R-Reports **22** (6), 269-322 (1998).

16 P. Patsalas, S. Logothetidis, and C. Metaxa, "Optical performance of nanocrystalline transparent Ceria films," Applied Physics Letters **81** (3), 466-468 (2002).

17 D. Mardare and P. Hones, "Optical dispersion analysis of TiO2 thin films based on variable-angle spectroscopic ellipsometry measurements," Materials Science and Engineering B-Solid State Materials for Advanced Technology **68** (1), 42-47 (1999).

18 S. U. M. Khan, M. Al-Shahry, and W. B. Ingler, "Efficient photochemical water splitting by a chemically modified n-TiO2 2," Science **297** (5590), 2243-2245 (2002).
19 Xavier Rocquefelte, Fabrice Goubin, Hyun-Joo Koo, Myung-Hwan Whangbo, and Stéphane Jobic, "Investigation of the Origin of the Empirical Relationship between Refractive Index and Density on the Basis of First Principles Calculations for the Refractive Indices of Various TiO2 Phases," Inorganic Chemistry **43** (7), 2246-2251 (2004).
20 D. Reyes-Coronado, G. Rodriguez-Gattorno, M. E. Espinosa-Pesqueira, C. Cab, R. de Coss, and G. Oskam, "Phase-pure TiO2 nanoparticles: anatase, brookite and rutile," Nanotechnology **19** (14) (2008).
21 B. Kralik, E. K. Chang, and S. G. Louie, "Structural properties and quasiparticle band structure of zirconia," Physical Review B **57** (12), 7027-7036 (1998).
22 Frank Lenzmann, Jessica Krueger, Shelly Burnside, Keith Brooks, Michael Gratzel, Doron Gal, Sven Ruhle, and David Cahen, "Surface Photovoltage Spectroscopy of Dye-Sensitized Solar Cells with TiO2, Nb2O5, and SrTiO3 Nanocrystalline Photoanodes: Indication for Electron Injection from Higher Excited Dye States," The Journal of Physical Chemistry B **105** (27), 6347-6352 (2001).
23 K. Højrup Hansen, T. Worren, S. Stempel, E. Lægsgaard, M. Bäumer, H. J. Freund, F. Besenbacher, and I. Stensgaard, "Palladium Nanocrystals on Al2O3: Structure and Adhesion Energy," Physical Review Letters **83** (20), 4120 (1999).
24 Wang-Jae Chun, Akio Ishikawa, Hideki Fujisawa, Tsuyoshi Takata, Junko N. Kondo, Michikazu Hara, Maki Kawai, Yasumichi Matsumoto, and Kazunari Domen, "Conduction and Valence Band Positions of Ta2O5, TaON, and Ta3N5 by UPS and Electrochemical Methods," The Journal of Physical Chemistry B **107** (8), 1798-1803 (2003).
25 B. Elidrissi, M. Addou, M. Regragui, C. Monty, A. Bougrine, and A. Kachouane, "Structural and optical properties of CeO2 thin films prepared by spray pyrolysis," Thin Solid Films **379** (1-2), 23-27 (2000).
26 Y. Lvov, K. Ariga, M. Onda, I. Ichinose, and T. Kunitake, "Alternate assembly of ordered multilayers of SiO2 and other nanoparticles and polyions," Langmuir **13** (23), 6195-6203 (1997).
27 G. Bogdanovic, T. Sennerfors, B. Zhmud, and F. Tiberg, "Formation and structure of polyelectrolyte and nanoparticle multilayers: Effect of particle characteristics," Journal of Colloid and Interface Science **255** (1), 44-51 (2002).
28 J. S. Ahn, P. T. Hammond, M. F. Rubner, and I. Lee, "Self-assembled particle monolayers on polyelectrolyte multilayers: particle size effects on formation, structure, and optical properties," Colloids and Surfaces a-Physicochemical and Engineering Aspects **259** (1-3), 45-53 (2005).
29 S. E. Yancey, W. Zhong, J. R. Heflin, and A. L. Ritter, "The influence of void space on antireflection coatings of silica nanoparticle self-assembled films," Journal of Applied Physics **99** (3) (2006).
30 Y. M. Lvov, J. F. Rusling, D. L. Thomsen, F. Papadimitrakopoulos, T. Kawakami, and T. Kunitake, "High-speed multilayer film assembly by alternate adsorption of silica nanoparticles and linear polycation," Chemical Communications (11), 1229-1230 (1998).

31 Y. Sakatani, D. Grosso, L. Nicole, C. Boissiere, Gjda Soler-Illia, and C. Sanchez, "Optimised photocatalytic activity of grid-like mesoporous TiO2 films: effect of crystallinity, pore size distribution, and pore accessibility," Journal of Materials Chemistry **16** (1), 77-82 (2006).
32 R. A. Caruso, A. Susha, and F. Caruso, "Multilayered titania, silica, and Laponite nanoparticle coatings on polystyrene colloidal templates and resulting inorganic hollow spheres," Chemistry of Materials **13** (2), 400-409 (2001).
33 M. F. Bertino, B. Smarsly, A. Stocco, and A. Stark, "Densification of Oxide Nanoparticle Thin Films by Irradiation with Visible Light," Advanced Functional Materials **19** (8), 1235-1240 (2009).
34 Z. S. Wang, T. Sasaki, M. Muramatsu, Y. Ebina, T. Tanaka, L. Z. Wang, and M. Watanabe, "Self-assembled multilayers of titania nanoparticles and nanosheets with polyelectrolytes," Chemistry of Materials **15** (3), 807-812 (2003).
35 A. Fujishima, X. T. Zhang, and D. A. Tryk, "TiO2 photocatalysis and related surface phenomena," Surface Science Reports **63** (12), 515-582 (2008).
36 H. Sankur and W. H. Southwell, "Broad-band gradient-index antireflection coating for ZNSE," Applied Optics **23** (16), 2770-2773 (1984).
37 W. H. Southwell, "Gradient-index anti-reflection coatings," Optics Letters **8** (11), 584-586 (1983).
38 L. B. Zhang, Y. Li, J. Q. Sun, and J. C. Shen, "Layer-by-layer fabrication of broad-band superhydrophobic antireflection coatings in near-infrared region," Journal of Colloid and Interface Science **319** (1), 302-308 (2008).
39 Z. Gemici, P. I. Schwachulla, E. H. Williamson, M. F. Rubner, and R. E. Cohen, "Targeted Functionalization of Nanoparticle Thin Films via Capillary Condensation," Nano Letters **9** (3), 1064-1070 (2009).
40 M. L. Kuo, D. J. Poxson, Y. S. Kim, F. W. Mont, L. K. Kim, E. F. Schuhert, and S. Y. Lin, "Realization of a near-perfect antireflection coating for silicon solar energy utilization," Optics Letters **33** (21), 2527-2529 (2008).
41 Z. Wu, D. Lee, M. F. Rubner, and R. E. Cohen, "Structural color in porous, superhydrophilic, and self-cleaning SiO2/TiO2 Bragg stacks," Small **3** (8), 1445-1451 (2007).
42 A. Kanta, R. Sedev, and J. Ralston, "Fabrication of silica-on-titania and titania-on-silica nanoparticle assemblies," Colloids and Surfaces a-Physicochemical and Engineering Aspects **292** (1), 1-7 (2007).
43 D. Lee, M. F. Rubner, and R. E. Cohen, "All-nanoparticle thin-film coatings," Nano Letters **6** (10), 2305-2312 (2006).
44 D. Lee, D. Omolade, R. E. Cohen, and M. F. Rubner, "pH-Dependent structure and properties of TiO2/SiO2 nanoparticle multilayer thin films," Chemistry of Materials **19** (6), 1427-1433 (2007).
45 T. Yonezawa, S. Onoue, and T. Kunitake, "Formation of ordered monolayer of anionic silica particles on a cationic molecular layer," Chemistry Letters (7), 689-690 (1998).

46 G. M. Lowman and S. K. Buratto, "Nanoscale morphology of polyelectrolyte self-assembled films probed by scanning force and near-field scanning optical microscopy," Thin Solid Films **405** (1-2), 135-140 (2002).

CHAPTER THREE

Experimental Details

3.1 Materials and Instruments

3.1.1 Materials

We used Nanophase technologies T1121W titania nanoparticles for all our titania films and all quarter wave stacks. The manufacturer's claim for the average diameter of the nanoparticles was 35nm. For the silica components of the quarter wave stacks, we used Snowtex ST-20L nanoparticles that had a putative average diameter of 45nm. PAH (M_w = 15000) and PDDA (M_w = 400000 – 500000) were purchased from Sigma-Aldrich. Premium frosted microscope glass slides were purchased from Fisher Scientific.

3.1.2 Instruments

All transmittance and reflectance measurements were performed using a Filmetrics F-20 spectrometer. All ellipsometry data was acquired using a J.A. Woolam VB-2000 ellipsometer.

DLS and zeta potential measurements were carried out using a Zetasizer nanoSZ by Malvern Instruments. The dipping machine used for block 2 of the quarter wave stacks was a StratoSequence VI from Nanostrata. The film images were taken by Atomic Force Microscopy (AFM) and Scanning Electron Microscopy (SEM). The AFM microscope is a Veeco BioScope II. The AFM images that we obtained were taken in the tapping mode with tapping frequencies of the order of 100,000Hz. The SEM microscope is a LEO (Zeiss) 1550 field emission microscope.

3.2 Approach – Statistical Analysis

In order to expedite the optimization of the film deposition process, we used two statistical design of experiment techniques, factorial design and response surface methods. A factorial design is a special case of a more general statistical technique called Analysis of Variance (ANOVA) in which each factor is evaluated at only two levels (called, generally, high and low).

The statistical analysis was facilitated by the software application Design Expert[1,2]. We provide a brief introduction to the basic statistics.

When a random variable z_i is normally distributed about the mean, there is a particular combination, $\chi^2 = z_1^2 + \ldots + z_k^2$, that follows another distribution called the chi-square distribution with k degrees of freedom. Now if z and χ^2_k are independent, standard normal and chi-square distributed random variables, respectively, then the random variable $t_i = z_i/\sqrt{(\chi^2_k / k)}$ follows a different distribution called the t distribution with k degrees of freedom. Finally if χ_u^2 and χ_v^2 are independent, chi-square distributed random variables with u and v degrees of freedom respectively, then the ratio

$F_{u,v} = (\chi_u^2/u) / (\chi_v^2/v)$

follows the $F_{u,v}$ distribution with numerator u and denominator v degrees of freedom.

The formula for the F distribution is

$$h(x) = \frac{\Gamma(\frac{u+v}{2})(\frac{u}{v})^{u/2} x^{(u/2)-1}}{\Gamma(\frac{u}{2})\Gamma(\frac{v}{2})[(\frac{u}{v})x+1]^{(u+v)/2}}$$

where x is a particular realization of $F_{u,v}$ from a population of measurements and $\Gamma(x)$ is the Gamma function (the generalization of the factorial function).

It is the F-distribution that we use in our experimental analysis to identify statistically significant factors. A factor is the independent variable in an experiment and may be a numerical (for example, temperature) or categorical (for example, the type of polyion) quantity. The measured dependent variable is called the response (for example, the Rayleigh slope).

For n treatments (a treatment is a particular assignment of levels to each factor), the total sum of squares is

$$(SS)_{total} = \sum_{i=1}^{n} (y_i - < y >)^2 .$$

which can be partitioned by the Orthogonality theorem into terms

$SS_{total} = SS_A + SS_B + \ldots + SS_{AB} + \ldots + SS_{error}$

where SS_A denotes the sum of squares for the main effect of A etc, SS_{AB} denotes the sum of squares for the AB interaction and so forth. The term SS_{error} denotes the error sum of squares. Each factor has a number of degrees of freedom. For the main effects we have

$df_{main\ effects}$ = levels of factor – 1

so in our case this number is always equal to 1 since all our factors have two levels.

For the interactions we have

$df_{interactions}$ = (levels of first factor – 1) (levels of second factor – 1)

Again for our experiment this number is equal to one. The total number of degrees of freedom is $df_{total} = n - 1$ where n is the number of treatments in the experiments. Finally, the error degrees of freedom are those remaining from d_{total} after accounting for $df_{main\ effects}$ and $df_{interactions}$

$df_{error} = df_{total} - df_{main\ effects} - df_{interactions}$

Now, for each main effect and interaction and for error we define the mean square

$MS_{main\ effect\ or\ interaction} = SS_{main\ effect\ or\ interaction}/df_{main\ effect\ or\ interaction}$

$MSE = SS_{error}/df_{error}$

from which we obtain the F-value for a particular main effect or interaction

$$F = \frac{MS_{maineffector\,\mathrm{int}\,eraction}}{MSE}$$

It is this ratio that follows the F distribution for a population of measurements. The integral of the F-distribution from the measured F-value to infinity is the p-value for that particular main effect or interaction. The null hypothesis is that the response does not depend on that particular main effect or interaction. The smaller the p-value, the less likely it is that the null hypothesis is true. The standard p-value for rejecting the null hypothesis is 0.05.

3.3 Deposition of Single Layer Titania Nanoparticle Films

3.3.1 Summary of Experiments

One of the two main parts of this thesis is optimization of single layer titania nanoparticle films for their role as the high refractive index component of the quarter wave stack. We performed a total of seven sets of titania film experiments. For sets 1 through 5 the only response was the Rayleigh slope. Additional responses were included for sets 6 and 7. These were film thickness and index of refraction from ellipsometry. The seven sets were:

Set 1. A factorial experiment to identify statistically significant factors. The reflectance from these films did not display interference fringes which led us to consider the problem of diffuse scattering.

Set 2. A response surface experiment to search for settings of the statistically significant factors that would minimize diffuse scattering.

Set 3. A response surface experiment to expand the region of parameter space explored in set 2. In addition the new factor = number of bi-layers was added to the experiments.

Set 4. A response surface experiment that explored additional regions of the parameter space.

Set 5. A response surface experiment intended as a supplemental set to set 4 that focused on only two factors, pH and molarity, and narrowed their values.

Set 6. A more extensive response surface experiment with the additional responses of film thickness and refractive index obtained by ellipsometry.

Set 7. A response surface experiment to explore whether aggregation of nanoparticles in the colloidal solution was contributing to the inhomogeneity of our films with the concomitant deleterious diffuse scattering. The large aggregates were precipitated from the colloidal solution by centrifugation. The added factor in this experiment was centrifugation time.

The primary objective of this thesis is the deposition of alternating titania and silica nanoparticles layers to create a quarter-wave stack. The deposition of a silica nanoparticle layer is well characterized and this material does not present the problem of excessive diffuse scattering. Titania films, on the other hand, are readily deposited by the ISAM process, but the films exhibit significant diffuse scattering due to bulk inhomogeneities or surface roughness. This section describes how the problem of diffuse scattering from ISAM deposited titania films was solved. .

3.3.2 Optimization of the Deposition Process to Minimize Diffuse Scattering from the Titania Films

There are several factors that can affect the deposition of titania nanoparticles including the polycation, dip time, wash time, colloidal and polycation solution pH, agitation intensity of the rinse solution, and colloidal solution molarity. Some of these factors have been identified in the published literature, such as colloidal solution pH which Yonezawa et al.[3] demonstrated had significant effect on the uniformity of the film because of its influence on the ionization of the polycation. In order to determine which factors and factor interactions have a statistically significant influence on the deposition process, our first experiment was a factorial design. After the statistical significant factors and factor interactions were identified, then we used response surface experiments to optimize the deposition process.

3.3.3 Description of the Experimental Procedure

All the films were deposited by hand-dipping the substrates into the appropriate solutions except for the second block of the last experiment (quarter-wave stacks) where the substrates were dipped by a machine to create the quarter-wave stack. The procedure used for all hand dipping, including the first block of the quarter wave stack experiment, is as follows:

- All films are deposited on RCA cleaned glass slides with part of the film covering the frosted end.
- The dipping is done using standard plastic slide holder containers for both solutions.
- The solutions are prepared with the required molarity and pH. All polycation solutions (PAH or PDDA) are stirred at least overnight. All polycation solutions are 10mM on a monomer basis.
- Washing with DI water is done after each layer is deposited.
- Washing is done by attaching the slide to an aluminum slide holder and placing it into a 1500mL beaker containing approximately 400mL of DI water and a magnetic stir bar. The beaker is placed on a stirring plate. The stirring speed and stirring time can be adjusted.
- Plastic tweezers are used to handle the slides.
- A record of each dipping is carefully recorded in the lab notebook in order to prevent mistakes.
- After all dipping is completed, the slides are dried with nitrogen. At no point during the dipping must the slides be allowed to air dry.
- The slide is labeled according to the set in which it belongs and to the run number that it occupies in the set. It is then placed in a special slide holding box. The location of the slide and its deposition conditions are recorded in the lab notebook.

3.4 Deposition of the Quarter-Wave Stack

The quarter-wave stacks were constructed in exactly the same way as the titania films described in the section above, except that the substrates were dipped by hand for the first block of the experiment and by machine for the second block.

There was one response surface experiment to optimize the deposition of the quarter-wave stack. The three factors were pH of both silica and titania colloidal solutions, molarity of the

silica solution, and wash time. The molarity of the titania solution was effectively governed by the centrifugation time (to remove nanoparticle aggregates) that was 10 minutes. Five bilayers of titania nanoparticles and PDDA were first deposited on microscope glass slides and then four bilayers of silica nanoparticles with PDDA were deposited on top of the titania film. The experiment involved a total of 24 films created in two blocks of 12. The first block was done by hand dipping in exactly the same way that all titania nanoparticle films were deposited while the second block was done by a dipping machine. Though one can not draw statistical inferences based on blocking factors (whether the film was hand dipped or machine dipped in this case) because the levels of the blocking factors are not randomized, comparison of the block sum of squares can provide a qualitative measure of the blocking factors influence. Our responses for the quarter-wave stack experiment were Rayleigh slope and titania and silica layer thickness. The refractive index of the silica layer was taken equal to 1.3. The titania and silica layer thicknesses and the refractive index of the titania layer were determined by ellipsometry using the Lorentz model.

References for Chapter 3

1 Mark J. Anderson and Patrick J. Whitcomb, *DOE Simplified*. (Productivity, 2000).

2 D. C. Montgomery, *Design and Analysis of Experiments.* (John Wiley and Sons, New York, 1997), 4th ed.

3 T. Yonezawa, S. Onoue, and T. Kunitake, "Formation of ordered monolayer of anionic silica particles on a cationic molecular layer," Chemistry Letters (7), 689-690 (1998).

CHAPTER FOUR

Results for Titania Nanoparticle Films.

The experimental procedure for these experiments was described in detail in Section 3.3. We performed a total of seven sets of experiments involving single layer titania nanoparticle films with the purpose of minimizing diffuse scattering. Here we give the details of each set along with the results of the statistical analysis.

4.1 Factorial Experiment (set 1)

The first experiment was designed not so much to provide specific ideas of how diffuse scattering depends on particular factors but as an initial screening experiment to identify statistically significant factors. For this purpose, a factorial experiment is well suited. The factors that we considered are shown in Table 4.1 along with their corresponding low and high levels.

FACTOR (Units)	**LEVELS (low, high)**
Polycation type	PAH, PDDA
pH of both solutions	7, 9
Molarity of titania solution (mM)	10, 100
Dip time (min)	2, 4
Wash time per side (min)	2, 4
Wash speed (dial indicator)	7, 10
Table 4.1. Factors and levels for the first set of experiments.	

All factors except polycation are numerical. Polycation is a categorical factor.

Given the fact that we have six factors each of which has two levels, we are faced with 2^6 = 64 experiments, a very large number by any measure. Fortunately, factorial experiments can be reduced to half factorials or even quarter factorials. The cost of such a reduction is that higher order interactions are confounded with lower order interactions or even with the main effects in some cases. We chose to use a half factorial experiment which would include 32 experiments

that were split into 2 blocks without replications or center points. In block 1 were 15 experiments done in the past by Sam Kung. In block 2 were 17 experiments. The two polycation solutions were a concentration of 10mM and were stirred overnight before use. The resulting experimental design with the results for the Rayleigh slope response is shown in Table 4.2. Similar tables are generated for the other 6 sets, but will not be shown.

Std	Run	Block	A	B	C	D	E	F	Rayleigh slope
14	1	1	PDDA	7	100	4	2	7	0.004543
16	2	1	PDDA	9	100	4	4	10	0.002392
7	3	1	PAH	9	100	2	2	7	0.0029
10	4	1	PDDA	7	10	4	4	10	0.001955
12	5	1	PDDA	9	10	4	2	7	0.004265
5	6	1	PAH	7	100	2	4	10	0.000875
9	7	1	PAH	7	10	4	2	10	0.003486
6	8	1	PDDA	7	100	2	2	10	0.004526
13	9	1	PAH	7	100	4	4	7	0.002026
15	10	1	PAH	9	100	4	2	10	0.0033
4	11	1	PDDA	9	10	2	2	10	0.005246
11	12	1	PAH	9	10	4	4	7	0.007458
2	13	1	PDDA	7	10	2	4	7	0.004029
1	14	1	PAH	7	10	2	2	7	0.003508
8	15	1	PDDA	9	100	2	4	7	0.002685
3	16	1	PAH	9	10	2	4	10	0.005887
30	17	2	PAH	7	100	4	2	7	0.0018
29	18	2	PDDA	7	100	4	4	7	0.001
18	19	2	PAH	7	10	2	4	7	0.0041
27	20	2	PDDA	9	10	4	4	7	0.0029
17	21	2	PDDA	7	10	2	2	7	0.0021
24	22	2	PAH	9	100	2	4	7	0.0036
22	23	2	PAH	7	100	2	2	10	0.0015
23	24	2	PDDA	9	100	2	2	7	0.0013
25	25	2	PDDA	7	10	4	2	10	0.0025
21	26	2	PDDA	7	100	2	4	10	0.001
26	27	2	PAH	7	10	4	4	10	0.0021
32	28	2	PAH	9	100	4	4	10	0.0028
20	29	2	PAH	9	10	2	2	10	0.0022
28	30	2	PAH	9	10	4	2	7	0.0032
31	31	2	PDDA	9	100	4	2	10	0.0016
19	32	2	PDDA	9	10	2	4	10	0.001

Table 4.2. List of experiments comprising set 1. A: Polycation, B: pH of both solutions, C: Molarity of titania nanoparticle solution, D: Dip time, E: Wash time, F: Wash speed.

It should be noted that a factorial experiment can contain center points; that is, points that lie between the two extremes that we have chosen for our factors. This helps us determine whether there is any non-linear behavior of the response. The disadvantage of center points is that they increase the number of experiments that have to be performed. Design Expert analyzes the results and offers all the relevant p-values by which we can decide the statistically significant factors that will be kept and the statistically insignificant factors that will not be considered further. In addition to this Design Expert offers many diagnostics that can help us spot problems. In Fig. 4.1 the experimental residuals (measurement minus model fit) are plotted versus run number. This graph displays no particular trend, say constantly decreasing with run number, providing evidence for the absence of systematic error.

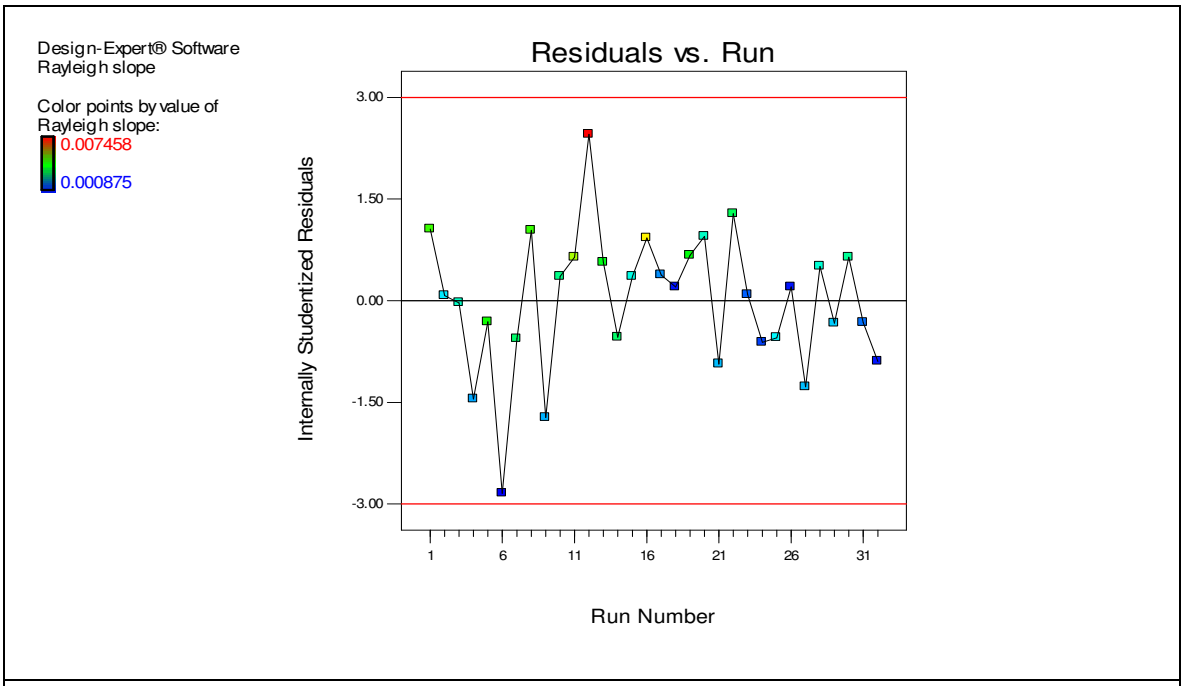

Fig. 4.1. Residuals vs. Run diagnostic graph for set 1.

Similar diagnostics will not be shown for any of the following sets since none of them exhibited problems.

The next step in the analysis of a factorial experiment is the identification of statistically significant factors. The half-normal plot for the data is used for this purpose and is shown in Fig. 4.2. If there were replications in this experiment and if the replicated measurements were normally distributed, then they would fall on a straight line in the half-normal plot. There were

no replications in this experiment, but those main effects and interactions that were not statistically significant provide a measure of the error distribution and form a straight line on the half-normal plot. Those main effects and interactions that are potentially significant lie below error line. In this case, many main effects and interactions appear to be statistically significant, probably because of systematic variability introduced by having two different people prepare the films (the blocking factor).

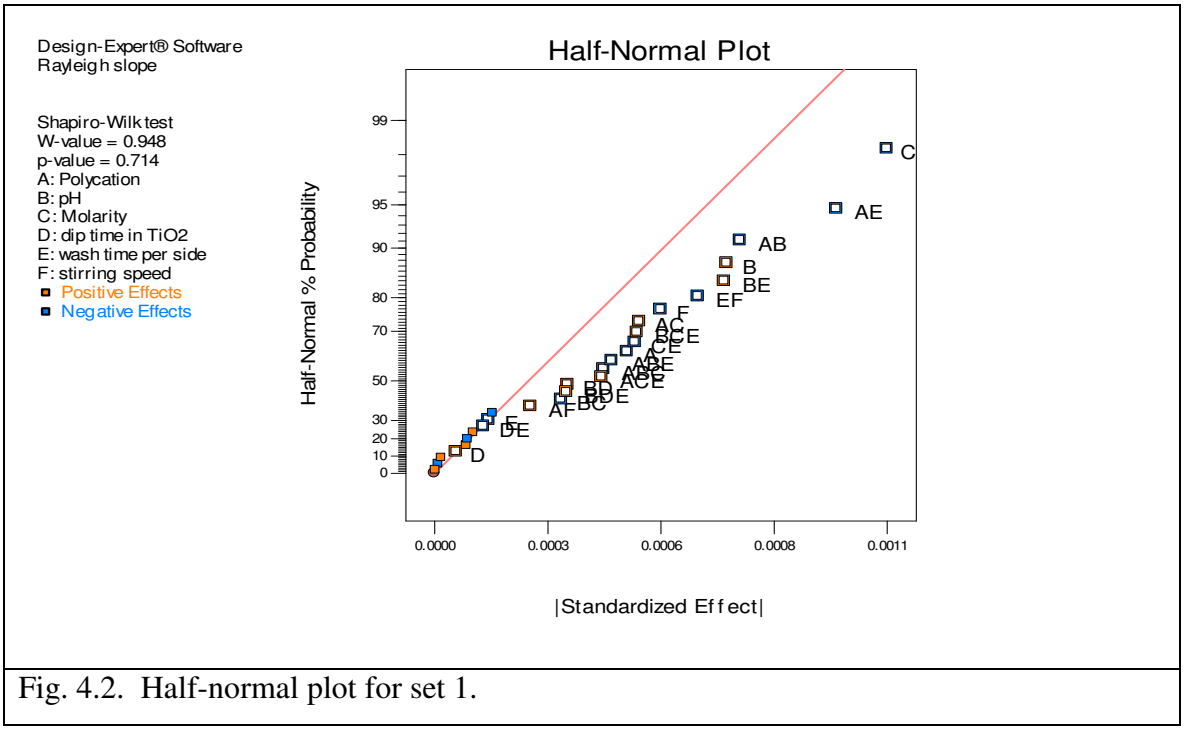

Fig. 4.2. Half-normal plot for set 1.

The ANOVA result for those main effects and interactions identified in the half-normal plot that have very small p-values ($p<0.0001$) is shown in Table 4.3. We have tightened the criteria for rejecting the null hypothesis from $p<0.05$ to $p<0.0001$ because of the large uncertainty introduced by the blocking factor.

Source	Sum of Squares	df	Mean Square	F Value	p-value Prob > F	
Block	1.86E-05	1	1.86E-05			
Model	3.46E-05	20	1.73E-06	34.09	< 0.0001	significant
Polycation	1.85E-06	1	1.85E-06	36.52	0.0005	
pH	4.27E-06	1	4.27E-06	84.12	< 0.0001	
Molarity	1.02E-05	1	1.02E-05	201.55	< 0.0001	
Wash Time	2.56E-06	1	2.56E-06	50.43	0.0002	
Polycation*pH	4.66E-06	1	4.66E-06	91.93	< 0.0001	
Polycation*Molarity	8.07E-06	1	8.07E-06	159.13	< 0.0001	
pH*Wash time	4.20E-06	1	4.20E-06	82.75	< 0.0001	
Wash time*Stir speed	3.47E-06	1	3.47E-06	68.33	< 0.0001	
Residual	3.55E-07	7	5.07E-08			
Cor Total	5.35E-05	28				

Table 4.3. ANOVA table for Rayleigh slope, set 1.

We infer from the low model p-value that the average of all the measurements is a poor fit to the data and, therefore, some main effects and/or interactions must be statistically significant. We observe that the main effects of pH and molarity are quite significant. The main effects of polycation and wash time do not meet the criteria ($p<0.0001$) but are retained for hierarchy (they appear in interaction terms). The interactions polycation*pH and polycation*wash time are also significant and are included in the model. We see that main effect of dip time is not statistically significant and it will therefore be set to 3 minutes for all the experiments conducted from now on. After the statistically significant factors and interactions have been identified, a regression model is constructed from the significant terms and fit to the data by standard regression techniques.

Fig. 4.3 shows graphs of the effect of the interaction between polycation and pH on the response with molarity set low and high, respectively. The model fit to the Rayleigh slope data is plotted versus polycation with black square and red triangles corresponding to low and high pH, respectively.

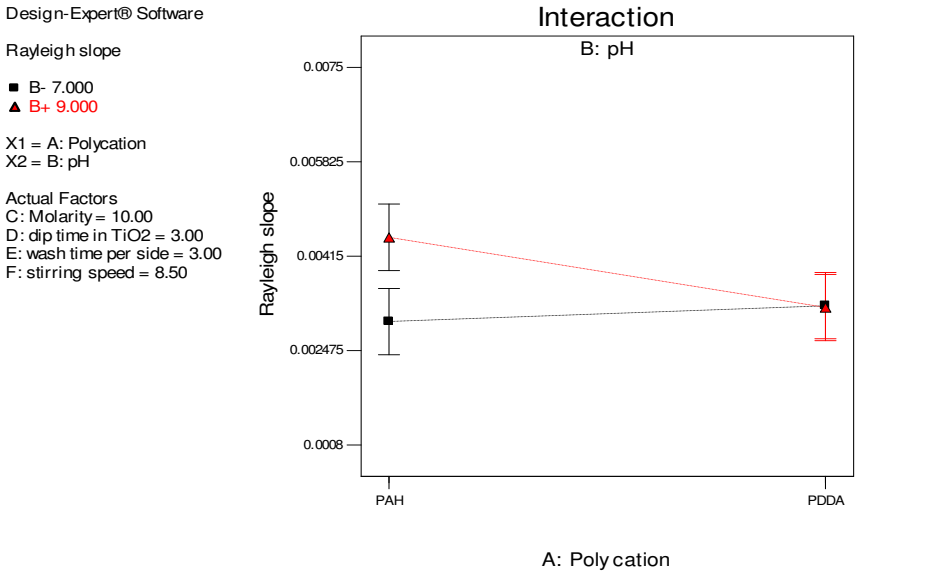

A

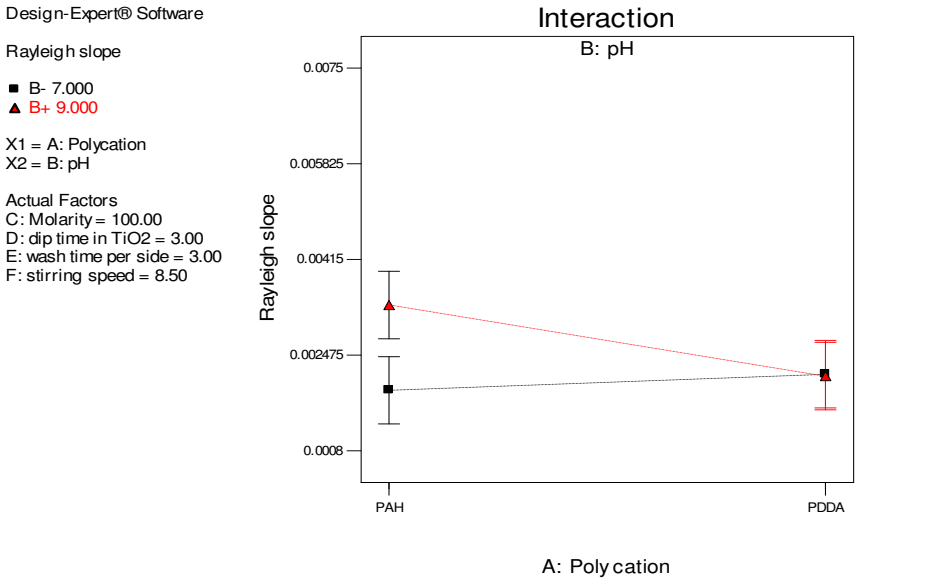

B

Fig. 4.3. Dependence of Rayleigh slope on the interaction polycation*pH for molarity low (A) and molarity high (B).

The molarities are 1mM and 100mM in Figures 4.3 A and B, respectively. We see that films produced with higher molarity have lower Rayleigh slopes. Secondly, if PAH is used as the polycation, the value of pH has a great influence on the Rayleigh slope while the slope is insensitive to pH if PDDA is the polycation. This result is consistent with PAH being a weak polycation (pK_a between 8 and 9[1]) while PDDA is a strong polycation (because it is a quaternary

amine) with a pH independent ionization level. The Rayleigh slope is independent of polycation, within statistical uncertainty, for both levels of pH.

Fig. 4.4 is the interaction plot of pH*wash time for low stir speed (A) and high stir speed (B). Minimized Rayleigh slope (blue) appears to occur for low pH and high wash time when the stir speed is high.

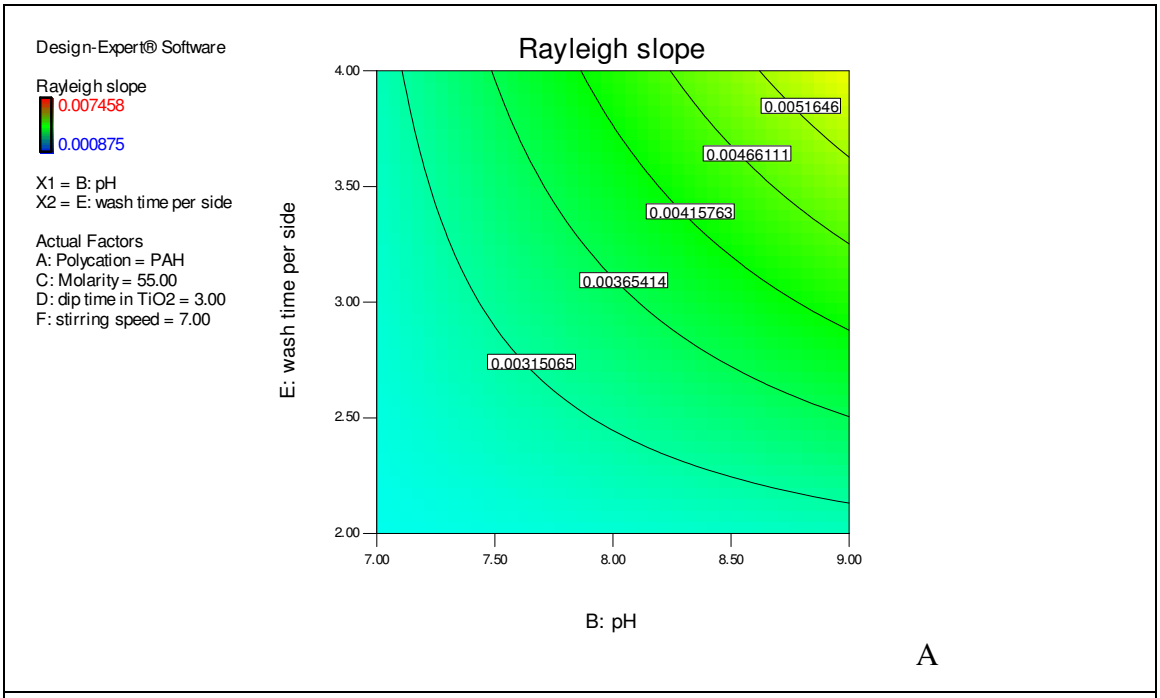

Fig. 4.4. Interaction of pH*wash time for stir speed low (A) and stir speed high (B).

4.2 Response Surface Experiment (set 2)

Having eliminated dip time as a significant factor and chosen PDDA (10mM) as the polycation to minimize the influence of pH on Rayleigh slope, we proceed to the first response surface experiment, set 2. The idea of the response surface is to optimize the levels of the statistically significant factors to either minimize or maximize the response. In our case we want to minimize the Rayleigh slope with respect to factors molarity, pH, and wash time. We hypothesize that the homogeneity of the deposited films might be improved if the dipping solutions are stirred during the deposition process and, therefore, add a fourth factor, stirrer speed. The stirrer speed levels are based on dial reading (1 to 10) on the stirrer. The factors and factor levels are shown in Table 4.4.

FACTOR (units)	**RANGE**
Molarity (mM)	50 – 200
pH	6 – 8
Wash time (min)	3 – 5
Stirrer speed (stirrer dial)	6 – 8

Table 4.4. Factors and levels for set 2.

Again, for the response, R and T are measured for each film and the quantity 1 – R – T is plotted versus $1/\lambda^4$. The slopes of the resulting straight lines are taken as the response that is to be minimized.

As discussed in section 3.2, the purpose of the response surface experiment is to identify the statistically significant terms rather than factors to be included in the model for the regression fit to the data. The ANOVA results for this analysis are shown in Table 4.5. The model fit is better than the overall average for the data ($p < 0.0001$) and only the linear term in pH is statistically significant. The model fits the data well (Lack of fit is insignificant).

Source	Sum of Squares	df	Mean Square	F Value	p-value Prob > F	
Model	3.34E-05	1	3.34E-05	29.19	< 0.0001	significant
pH	3.34E-05	1	3.34E-05	29.19	< 0.0001	
Residual	3.20E-05	28	1.14E-06			
Lack of Fit	2.04E-05	23	8.89E-07	0.38	0.9476	not significant
Pure Error	1.16E-05	5	2.31E-06			

Table 4.5. ANOVA table for Rayleigh slope, set 2.

The model fit of Rayleigh slope versus pH is shown in Figure 4.5.

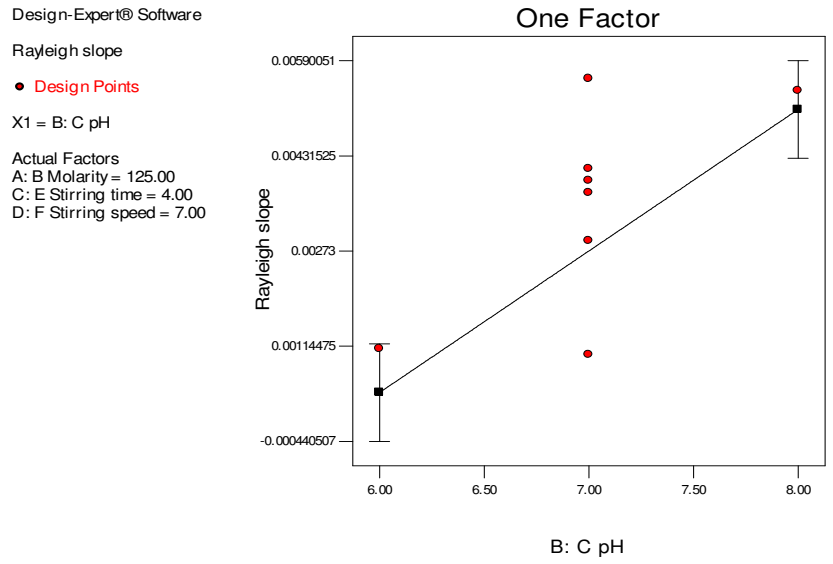

Fig. 4.5. Main effect of pH on Rayleigh slope. The red circles represent design points and the error bars show the 5% confidence interval in the response.

It is evident that low pH values minimize the response but it is possible that the lower Rayleigh slope at lower pH is due to less film being deposited. This possibility will be explored in experiment set 6 when we add film thickness measured by ellipsometry as another response.

4.3 Response Surface Experiment (set 3)

Experiments set 1 and 2 have suggested that a lower pH produces a more homogeneous film and that dip time and wash speed are not statistically significant factors. For the remaining experiments, wash speed will be set to 8.5. Set 3 is a new response surface experiment to expand

the range of our factors from set 2. In particular, the range of pH was extended down to 2 in order to determine whether the Rayleigh slope continued decreasing with decreasing pH or whether it went through a minimum between 2 and 7. We also add a new categorical factor, bilayers. Ideally, the number of bilayers would influence only the center wavelength of the reflectance minimum and not other optical properties such as the index of refraction and the level of diffuse scattering. Adding this factor will test this assumption. In addition, if the level of diffuse scattering is independent of film thickness, that would be evidence for associating the scattering with surface roughness rather than with bulk inhomogeneities. We chose the number of bilayers to be a categorical factor because otherwise, if it were a numerical factor, some levels of the number of bilayers would not have been integers. The factors and ranges of factors are shown in Table 4.6. The response for this experiment was the Rayleigh slope. The molarity of PDDA was 10mM.

FACTOR (units)	**RANGE**
pH	2 – 7
Molarity (mM)	30 – 90
Wash time (min)	2 – 5
Bilayers (categorical)	Low (5) – High (8)

Table 4.6. Factors and levels for set 3.

The ANOVA table for set 3 is shown in Table 4.7.

Source	Sum of Squares	df	Mean Square	F Value	p-value Prob > F	
Block	7.94371E-06	2	3.97185E-06			
Model	2.44283E-05	5	4.88566E-06	8.96	< 0.0001	Significant
pH	4.76882E-07	1	4.76882E-07	0.87	0.3567	
Molarity	3.73828E-07	1	3.73828E-07	0.69	0.4138	
Wash time	2.15019E-06	1	2.15019E-06	3.94	0.0557	
Molarity*wash	2.4025E-06	1	2.4025E-06	4.41	0.0438	
pH*pH	1.90249E-05	1	1.90249E-05	34.89	< 0.0001	
Residual	1.74477E-05	32	5.45242E-07			
Lack of Fit	1.56677E-05	26	6.02605E-07	2.03	0.1919	not significant
Pure Error	0.00000178	6	2.96667E-07			

Table 4.7. ANOVA table for Rayleigh slope, set 3.

The model is a better description of the data than the overall average of the data ($p<0.0001$), in other words, the factors that are included in the model have a significant effect, and the model provides a good fit for the data (Lack of fit is insignificant). The interaction between molarity and wash time is barely significant ($p = 0.0438$) while the quadratic term for pH is very significant. All the linear terms are included in the model for hierarchy. It is very encouraging that neither the linear nor the quadratic terms in the number of bilayers nor the interaction between number of bilayers and the other factors is statistically significant. This is our first evidence that diffuse scattering is a surface rather than a bulk effect. Fig. 4.6 is a graph of Rayleigh slope versus pH with molarity and wash time set to their center level values. This graph is for 5 bilayers, but the graph is independent of the number of bilayers.

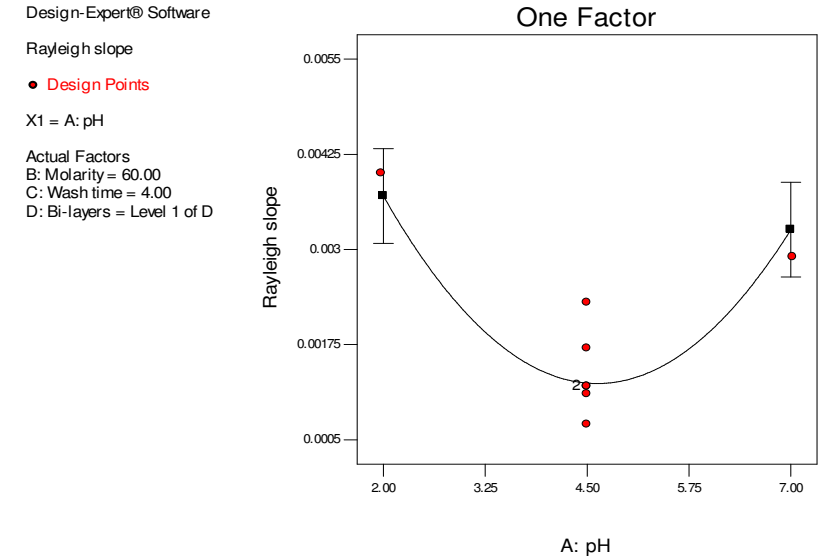

Fig. 4.6. Effect of pH on Rayleigh slope.

We see that, in fact, the Rayleigh slope goes through a minimum at pH = 4.5. The interaction between molarity and wash time is not shown because it is not very informative.

4.4 Response Surface Experiment (set 4)

We continue is this way investigating different regions of the parameter space. Set 4 deals with the same factors as set 3 but extends pH to 10 and molarity to 1000mM. The wash time is extended to include no wash. The number of bilayers is now a numerical factor. When the experimental design calls for a non-integer number of bilayers, it is rounded to the nearest integer. This set consists of 30 experiments broken into three blocks with again Rayleigh slope the response. The molarity of PDDA was 10mM. The factors and their range of levels are shown in Table 4.8.

FACTOR (units)	RANGE
pH	7 – 10
Molarity (mM)	100 – 1000
Wash time (min)	0 – 4
Bilayers	4 – 8

Table 4.8. Factors and levels for set 4.

The ANOVA table for set 4 is shown in Table 4.9.

Source	Sum of Squares	df	Mean Square	F Value	p-value Prob > F	
Block	8.437536385	2	4.218768192			
Model	242.3415169	9	26.92683521	58.75	< 0.0001	significant
pH	187.370751	1	187.370751	408.83	< 0.0001	
molarity	8.152012549	1	8.152012549	17.79	0.0006	
Wash time	0.051351319	1	0.051351319	0.11	0.7419	
bilayers	1.824456405	1	1.824456405	3.98	0.0623	
pH*molarity	3.231309958	1	3.231309958	7.05	0.0167	
pH*wash	2.422041823	1	2.422041823	5.28	0.0345	
ph*bilayers	3.664361709	1	3.664361709	8.00	0.0116	
molarity*molarity	9.086215389	1	9.086215389	19.83	0.0003	
wash*wash	21.22517684	1	21.22517684	46.31	< 0.0001	
Residual	7.791323649	17	0.458313156			
Lack of Fit	7.243097513	14	0.517364108	2.83	0.2125	not significant
Pure Error	0.548226136	3	0.182742045			

Table 4.9. ANOVA table for Rayleigh slope, set 4.

The model is a better description of the data than the overall average of the data ($p<0.0001$) and the model provides a good fit for the data (Lack of fit is insignificant). The linear terms, pH and molarity, are highly significant, but in contrast to set 3, the quadratic term pH*pH is not significant while the two quadratic terms molarity*molarity and wash*wash are highly significant. The interaction terms pH*molarity, pH*wash, and pH*bilayers are also significant. The linear term for wash time has been retained in the model for hierarchy.

Fig. 4.7 is a contour plot for the interaction between pH and molarity with wash time and number of bilayers set to their center values.

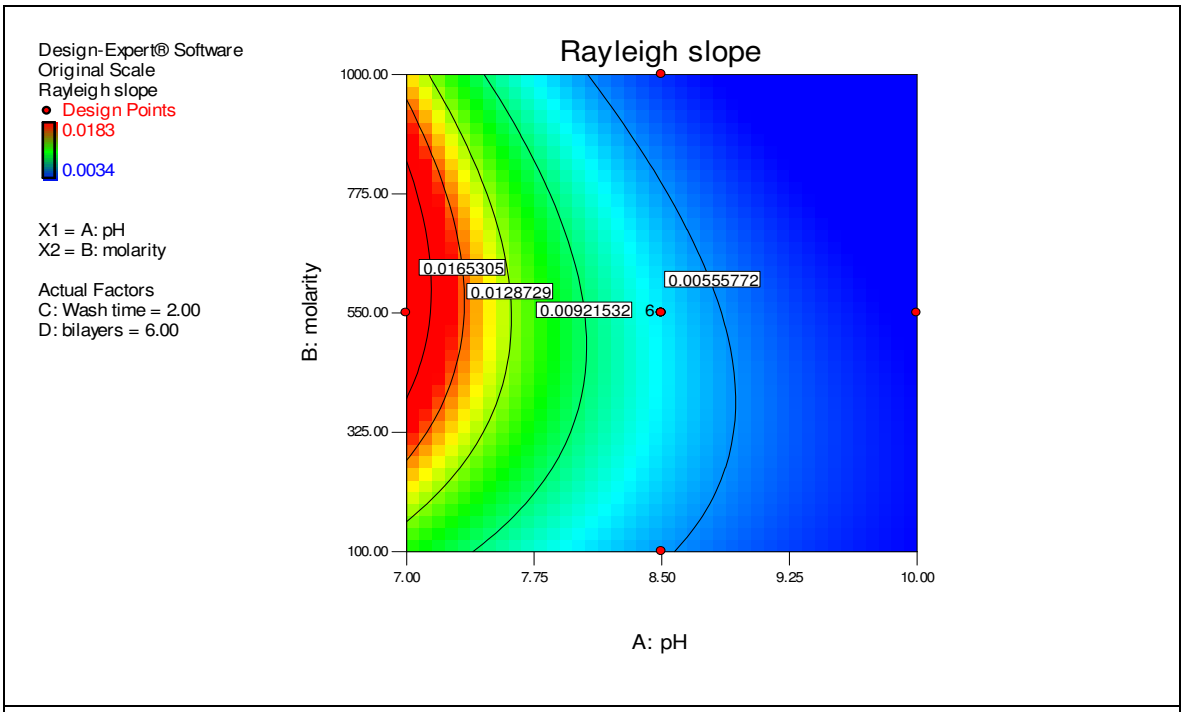

Fig. 4.7. Interaction graph for pH and molarity for set 4.

The color code for the Rayleigh slope extends through the visible spectrum from red for the lowest value and blue for the highest. One can see that the largest Rayleigh slope is obtained in the mid experimental range for molarity and at the lowest experimental level of pH while the highest Rayleigh slopes occur at the high end of the experimental range for both molarity and pH. The number of bilayers and the wash time have very little effect on the Rayleigh slope as expected from their high p-values.

4.5 Response Surface Experiment (set 5)

Set 5 is a small extension of set 4 to lower molarity while keeping pH in the range 6 to 8 where the diffuse scattering appeared to go through a maximum. The wash time was set to 3 minutes. The molarity of PDDA was 10mM.

The ANOVA table for set 5 is shown in Table 4.10.

Source	Sum of Squares	df	Mean Square	F Value	p-value Prob > F	
Model	5.90E-05	4	1.48E-05	35.20	< 0.0001	significant
pH	1.64E-06	1	1.64E-06	3.90	0.0836	
Molarity	3.64E-05	1	3.64E-05	86.74	< 0.0001	
pH*Molarity	3.42E-06	1	3.42E-06	8.17	0.0212	
pH*pH	1.76E-05	1	1.76E-05	42.00	0.0002	
Residual	3.35E-06	8	4.19E-07			
Lack of Fit	3.03E-06	4	7.56E-07	9.22	0.0268	significant
Pure Error	3.28E-07	4	8.20E-08			
Cor Total	6.24E-05	12				

Table 4.10. ANOVA table for Rayleigh slope, set 5.

The model is a better description of the data than the overall average of the data ($p<0.0001$) but the model provides a poor fit for the data (Lack of fit is significant). A contour plot of the interaction pH*molarity is shown in Fig. 4.8. The Rayleigh slope is minimized for low pH and low molarity.

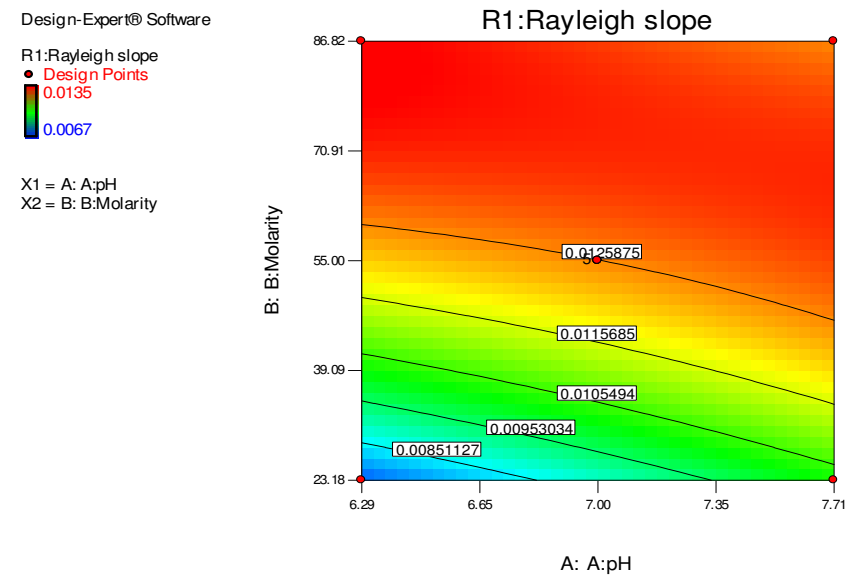

Fig. 4.8. Interaction plot of pH*molarity, set 5.

The information that we obtained from set 5 was only a confirmation of what we had obtained previously, namely that lower pH values produce films that scatter less and that molarity and pH have a strong interaction whereas low pH values with low molarity titania

solutions produce films that scatter less. For this set, the lack of fit with the model was significant. This is probably due to the small number of factors and the small number of experiments, resulting in insufficient degrees of freedom for error. Although it is encouraging to have our previous results verified, it is obvious that there is a need for more experiments and further investigation of the Rayleigh slope. In addition, new responses can now be introduced such as film thickness obtained by ellipsometry.

We have now reached a point where we are more comfortable with the deposition process for our films so that we can consider other responses, such as film thickness and index of refraction from ellipsometry measurements, to characterize our film. We also consider other possible sources of diffuse scattering and consider a different approach for measuring it.

4.6 Response Surface Experiment (set 6)

4.6.1 New Factors and Responses

For set 6 we expand our approach for optimizing the deposition process for minimum diffuse scattering. This is done in three ways:

1) We added a new categorical factor called "cleaning procedure": As was mentioned in Section 1.3, the conventional way of scrubbing the slides with acetone and kim-wipes in the RCA cleaning procedure may scratch the slide surface and enhance the scattered intensity. In order to explore that possibility, we replaced the usual scrubbing of the slide with immersion of the slides in a sonic bath of acetone for 40 minutes. The two levels of the categorical factor, "cleaning procedure", were the traditional RCA method (level 1) and the acetone sonic bath (level 2).

2) We introduce two new responses, film thickness and film index of refraction, that were measured by ellipsometry.

3) So far we have neglected absorption by the titania nanoparticles assuming that the loss in transmitted beam intensity is due to diffuse scattering. We will now consider the possibility that titania has a small but nonzero extinction coefficient which would result in absorption of the incident light. Absorption will be treated in more detail in Section 4.7.

4) Also for the first time, we obtain AFM images of some of our films in order to characterize the roughness of the film's surface and determine whether it correlates with the level of diffuse scattering.

4.6.2 Rayleigh Slope

The factors and their levels for set 6 are shown in Table 4.11.

FACTOR (units)	**RANGE**
pH	7 – 8
Molarity of TiO_2 (mM)	50 – 200
Cleaning procedure	Standard, sonication

Table 4.11. Factors and levels set 6.

This set involves a total of 26 experiments. Table 4.12 is the ANOVA table for the first response, the Rayleigh slope.

Source	**Sum of Squares**	**df**	**Mean Square**	**F Value**	**p-value Prob > F**	
Model	1.08E-04	6	1.79E-05	12.86	< 0.0001	significant
pH	1.00E-08	1	1.00E-08	0.01	0.9334	
Molarity	1.61E-06	1	1.61E-06	1.16	0.2959	
Cleaner	7.51E-05	1	7.51E-05	53.85	< 0.0001	
pH*Molarity	7.61E-06	1	7.61E-06	5.45	0.0307	
pH*Cleaner	6.49E-06	1	6.49E-06	4.66	0.0440	
Molarity*Molarity	1.68E-05	1	1.68E-05	12.03	0.0026	
Residual	2.65E-05	19	1.40E-06			
Lack of Fit	2.15E-05	11	1.95E-06	3.11	0.0591	not significant
Pure Error	5.02E-06	8	6.28E-07			
Cor Total	1.34E-04	25				

Table 4.12. ANOVA table for Rayleigh slope, set 6.

The model is a better description of the data than the overall average of the data ($p<0.0001$) and the model provides a good fit for the data (Lack of fit is insignificant). An interesting point is that the linear term, "cleaning procedure", is very significant and that the cleaning procedure interacts with pH (moderately significant). The Rayleigh slope is plotted versus pH in Fig. 4.9 with the black squares and red triangles being the model fits for the traditional and sonic cleaning, respectively. It is evident that the traditional method of RCA cleaning is far more effective than sonic cleaning and will be used for the remaining experiments.

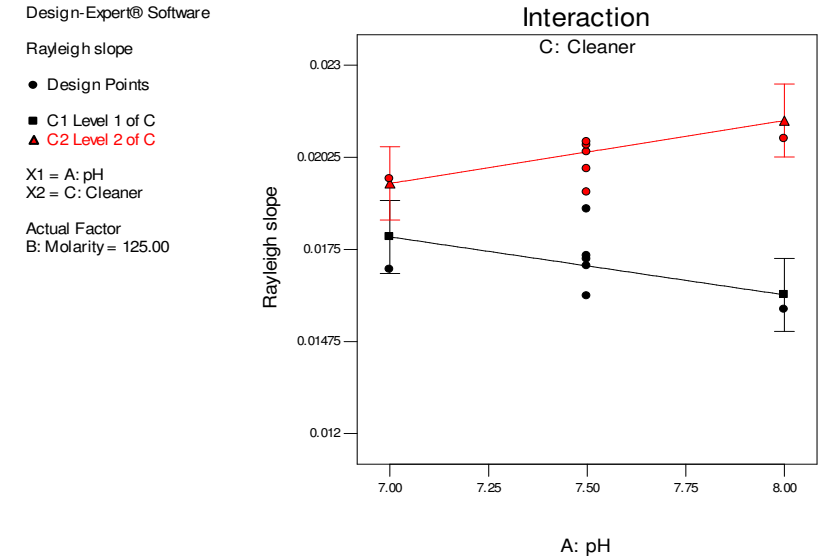

Fig. 4.9. Interaction of cleaner and pH. The black squares represent the standard cleaning method and the red triangles represent the sonication method.

Fig. 4.10 is a contour plot of the Rayleigh slope for the interaction between pH and molarity with the color code ranging from low (blue) to high (red) Rayleigh slope. There appears to be a ridge with the Rayleigh slope maximum occurring at pH ≈ 7.5. Although our goal is to minimize the Rayleigh slope, the minimum Rayleigh slope may correspond to minimum film thickness. This possibility is explored by measuring the thicknesses of the set 6 films by ellipsometry. At the same time we also measured the index of refraction.

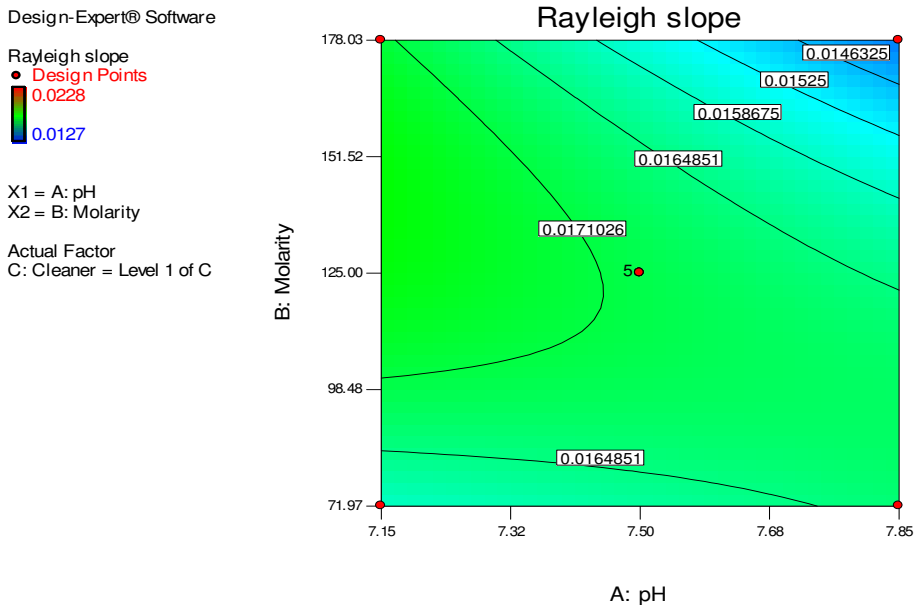

Fig. 4.10. Interaction graph of pH*molarity for Rayleigh slope, set 6.

4.6.3 Film Thickness and Index of Refraction

The thicknesses and indices of refraction of the set (6) films were measured by ellipsometry using the EMA model to analyze the raw data. At this point we had not yet attempted the Lorenz model. The ANOVA table for thickness is shown in Table 4.13.

Source	Sum of Squares	df	Mean Square	F Value	p-value Prob > F	
Model	3443.280207	2	1721.6401	20.62	< 0.0001	significant
B-Molarity	3098.23854	1	3098.23854	37.12	< 0.0001	
C-Cleaning procedure	395.5221848	1	395.522185	4.74	0.0411	
Residual	1752.984793	21	83.4754663			
Lack of Fit	1293.276793	13	99.4828303	1.73	0.2208	not significant
Pure Error	459.708	8	57.4635			

Table 4.13. ANOVA table for film thickness from ellipsometry.

The model is a better description of the data than the overall average of the data ($p<0.0001$) and the model provides a good fit for the data (Lack of fit is insignificant). The linear "cleaning procedure" term is barely significant, in sharp contrast to the results for Rayleigh scattering where it was quite significant. The linear molarity term is very significant and the quadratic molarity term is insignificant, again in contrast to the Rayleigh slope where the linear dependence on molarity was insignificant while the quadratic dependence was quite significant.

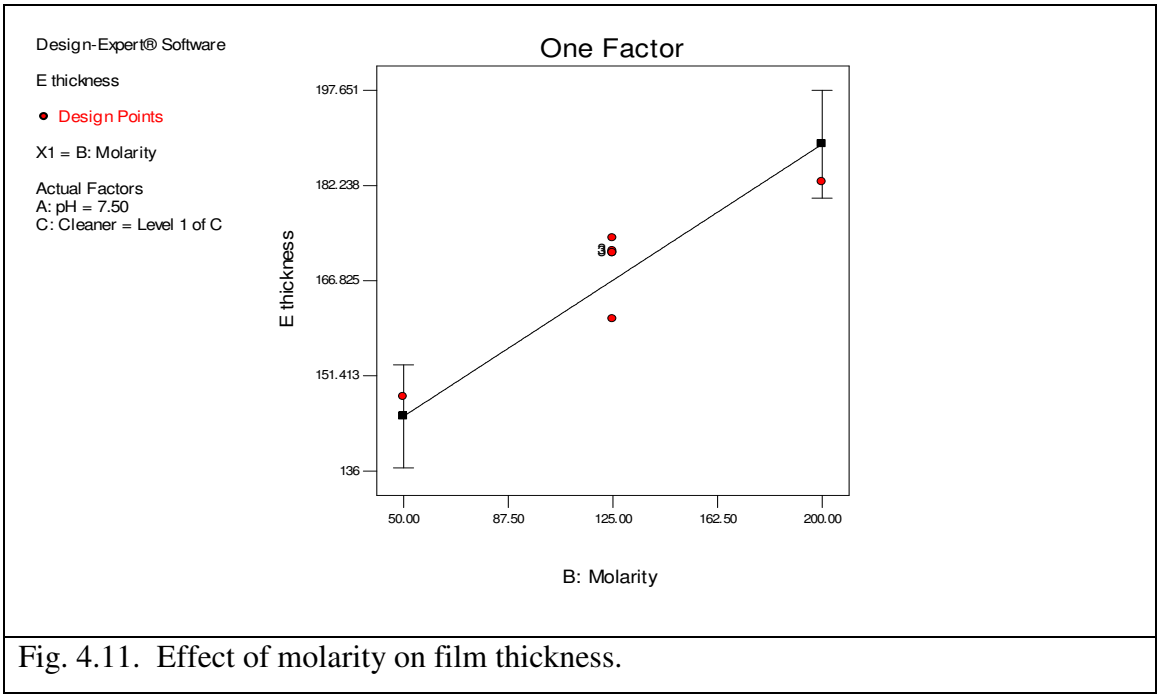

Fig. 4.11. Effect of molarity on film thickness.

A plot of thickness versus molarity is shown in Fig. 4.11 for the traditional cleaning procedure. The thickness increases with increasing molarity, while from Fig. 4.10 we see that the Rayleigh slope goes through a broad maximum in the range of molarity between 72mM to 178mM with pH = 7.5.

The ANOVA table for the index of refraction is shown in Table 4.14.

Source	Sum of Squares	df	Mean Square	F Value	p-value Prob > F	
Model	2.74E-03	3	9.15E-04	50.74	< 0.0001	significant
A-pH	4.26E-04	1	4.26E-04	23.63	0.0001	
B-Molarity	1.01E-03	1	1.01E-03	56.28	< 0.0001	
C-Cleaning procedure	1.33E-03	1	1.33E-03	73.57	< 0.0001	
Residual	3.25E-04	18	1.80E-05			
Lack of Fit	1.42E-04	10	1.42E-05	0.62	0.7625	not significant
Pure Error	1.82E-04	8	2.28E-05			

Table 4.14. ANOVA table for index of refraction.

The model is a better description of the data than the overall average of the data ($p<0.0001$) and the model provides a good fit for the data (Lack of fit is insignificant). The linear terms for all three factors are quite significant while neither the interactions nor quadratic terms are significant. We find that the index of refraction decreases with increasing pH, increases with increasing molarity, and is slightly higher for sonication versus traditional cleaning of the slides (data not shown).

4.6.4 Surface Roughness from AFM Images

In experiment set (3), the Rayleigh slope did not depend on the number of bilayers suggesting that the diffuse scattering was due to surface roughness rather than bulk inhomogeneities. But the range of the number of bilayers was relatively small (5 to 8), so it is possible that the contribution of bulk inhomogeneities to the diffuse scattering was lost in the noise. To explore this question further, we measured by AFM the surface profiles of three samples with low, medium, and high values of the Rayleigh slope. Our hypothesis was that the amplitudes of the surface roughness Fourier components with wavelengths in the visible range of light would correlate with the values of the Rayleigh slopes.

The technique of Atomic Force Microscopy (AFM) consists either of dragging the AFM tip across the surface of interest or, if the surface is sensitive and easy to damage, tapping the tip on the surface at a frequency of the order of 100,000Hz. This mode of operation is known as tapping mode and it is the one that we employed since we do not want to damage our films. We took AFM images of films 23, 20, and 3 corresponding to the lowest, intermediate, and highest

Rayleigh slopes, respectively. We obtained one 2μ x 2μ image and one 5μ x 5μ image. These two size images and diagonal cross-section profiles of each for film 3 are shown in Fig. 4.12. The Fourier spectrum versus wavevector (=1/λ) for the surface roughness also is shown in the figure. We find that the largest amplitudes of the Fourier components occur in the infrared and that the amplitudes for wavelengths corresponding to visible light are comparable for all three samples. That is, the Rayleigh slope does not correlate with the Fourier components of surface roughness having wavelengths in the visible. We also obtain the RMS surface roughness from these surface profiles and the results are compared to the Rayleigh slopes for the same samples in Table 4.15. There appears to be a correlation between Rayleigh slope and RMS roughness, but the results are not conclusive.

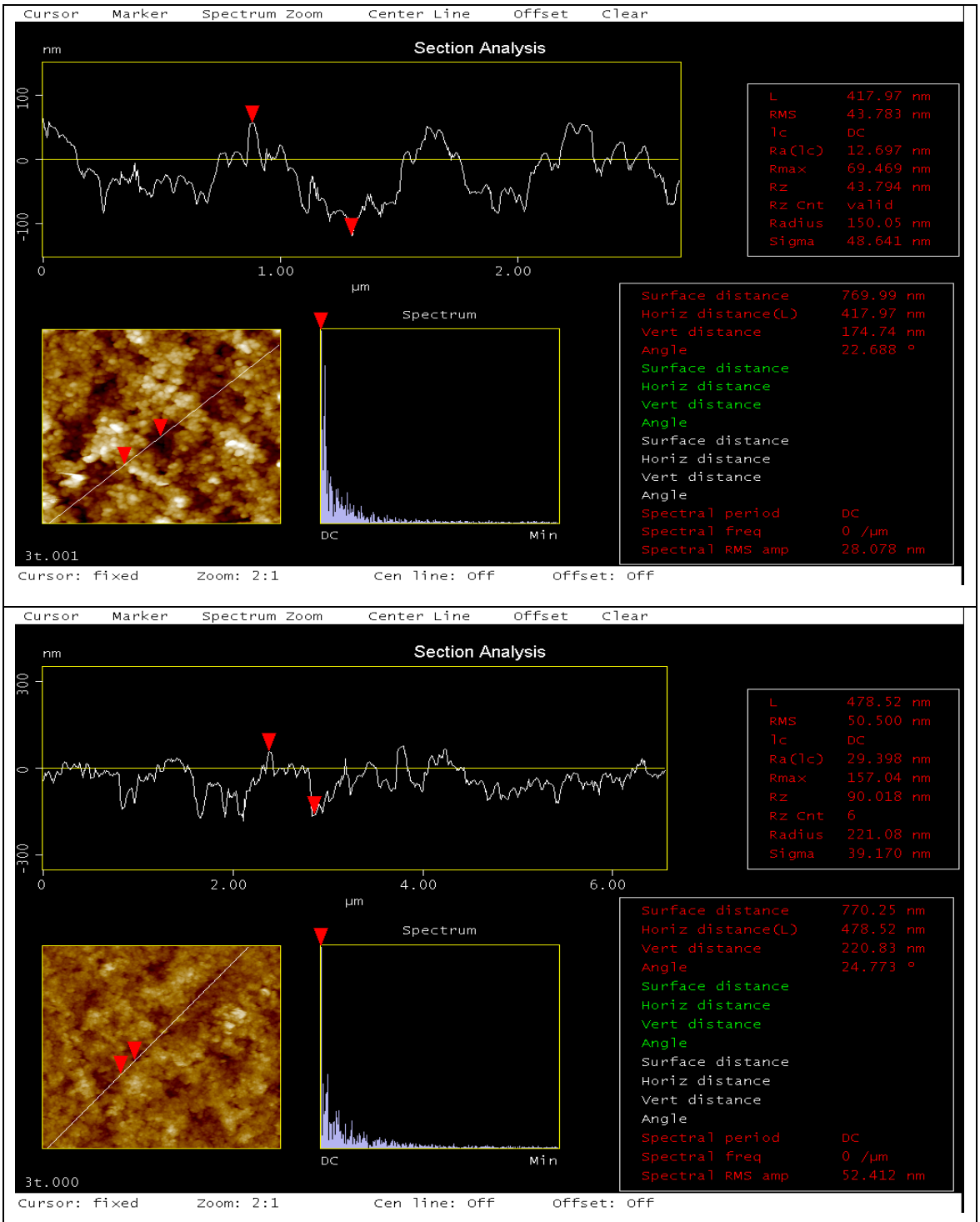

Fig. 4.12. AFM images for film 3, set 6.

SAMPLE (set 6)	RMS ROUGHNESS (nm)	RAYLEIGH SLOPE
23	34.8	0.012
20	42.9	0.016
3	50.5	0.017

Table 4.15. RMS roughness values from AFM and Rayleigh slopes for films 3, 20, and 23, set 6.

At this point in the research, diffuse scattering was still a significant problem and we felt we had exhausted further possibility of optimizing the deposition process. We turned our attention to the possibility that the surface roughness and possible bulk inhomogeneities were a consequence of the nanoparticles (nominal diameter = 35nm) aggregating in the colloidal solution. Our hypothesis was that if we could breakup the aggregates or remove them from the colloidal solution, then the diffuse scattering would be less.

4.7 Characterizing Aggregation in the Titania Colloidal Solutions by Dynamic Light Scattering

So far we have been trying to decrease diffuse scattering by optimizing the deposition process. The question now is whether this is a problem inherent in the deposition process or whether large aggregates exist in the titania colloidal solutions that are being deposited in the film and contributing to the diffuse scattering.

In order to characterize the degree of titania nanoparticle aggregation in our colloidal solutions, we performed Dynamic Light Scattering (DLS) measurements on the solutions. We also analyzed by DLS the size distribution of titania particles in colloidal suspensions that were from a different manufacturer. DLS gives us the particle size distribution based on scattering of light for a fixed incident angle from the Brownian motion of the particles. The incident beam from a laser is monochromatic and coherent and, as a consequence, the intensity of scattered light varies in time due to interference between scattered waves from different scattering centers that are constantly moving with respect to each other. The intensity of light scattered from small and large particles fluctuates at relatively high and low frequencies, respectively. The distribution of fluctuation frequency is related to the distribution of particle sizes in the suspension and, thus, by evaluating the autocorrelation of the time dependent scattered intensity,

the particle size distribution can be inferred. Ideally the size distribution would be narrow and centered on 35 nm, the nominal diameter of our nanoparticles. It should be noted that the colloidal suspensions being probed by DLS have to have relatively small concentrations in order to avoid multiple scattering of the incoming beam.

We now turn our attention to finding ways to reduce the average size of the aggregates. There are four approaches that we considered:

1) Sonication. We attempt to break up the large particle aggregates by sonicating the solution before deposition but it was possible that the particles might re-aggregate before the dipping is completed or on the substrate.

2) Filtration. The attempt here was to remove the large particle aggregates by passing the solution through filters. Some filters alter the surface charge of the particles which is undesirable when the particles are to be used for ISAM deposition. Teflon filters were chosen since they do not affect the surface charge.

3) Different source of colloidal titania solutions. So far we have been using titania particles provided by Nanophase technologies. We found a different source of nanoparticles, Evonik-Degusa, and measured their size distribution by DLS. We found the distribution was worse than the distribution of nanoparticles sizes in colloidal solution from Nanophase. This approach was not pursued further.

4) Centrifugation. Another way to separate large aggregates from smaller particles is centrifugation. A rough calculation shows that centrifuging our titania nanoparticles in water for a time between 2 and 10 minutes at 6000 x g should separate most aggregates into the sediment and leave the smaller particles still in the supernatant fluid.

4.7.1 Sonication-Filtration

We used a factorial design experiment to test whether sonication and/or filtration would improve the size distribution of nanoparticles supplied by Nanophase. The four factors and the factor levels are given in Table 4.16. The response for this experiment was the average particle diameter as measured by DLS. Each treatment (2^4) was replicated twice giving a total of 32 runs. The ANOVA table is not shown. But the overall average of the data was a good description of the data indicating that none of the main effects or interactions were statistically significant.

FACTORS (Units)	LEVELS (low, high)
Filter pore diameter (categorical)	220 nm, 450 nm
Sonication (categorical)	Yes, No
pH	7, 9
Molarity (mM)	10, 50

Table 4.16. Factors and levels for particle size factorial experiment.

4.7.2 Centrifugation

Our next attempt to remove aggregates from the titania colloidal solution was to centrifuge the solution. In order to determine whether centrifugation of the colloidal solution was an efficacious way to improve the particle size distribution, we did a response surface experiment with two factors, time in the centrifuge and molarity before centrifugation. The centrifugation acceleration was 6000g. The levels of centrifugation time and molarity ranged from zero to 3 minutes and from 1 to 100mM, respectively. It should be noted that after centrifugating the colloidal solution the molarity of the solution is unknown. The response was again the average particle diameter as measured by DLS. The ANOVA table for this response surface experiment is shown in Table 4.17.

Source	Sum of Squares	df	Mean Square	F Value	p-value Prob > F	
Model	1.62E+04	5	3.24E+03	22526.87	< 0.0001	significant
time	1.21E+04	1	1.21E+04	84463.66	< 0.0001	
Molarity	2.06E+02	1	2.06E+02	1435.92	< 0.0001	
time*molarity	6.19E+01	1	6.19E+01	430.62	0.0002	
time*time	8.71E+00	1	8.71E+00	60.56	0.0044	
molarity*molarity	1.32E+01	1	1.32E+01	92.05	0.0024	
Residual	4.31E-01	3	1.44E-01			
Lack of Fit	4.31E-01	2	2.16E-01			
Pure Error	0	1	0			

Table 4.17. ANOVA table for centrifugation time experiment.

The model is a better description of the data than the overall average of the data ($p<0.0001$), but there were insufficient degrees of freedom to assess the Lack of Fit. The linear terms, interaction, and quadratic terms were all statistically significant. A contour plot of the interaction between centrifugation time and molarity is shown in Fig. 4.13. The color code for

the average particle diameter ranges from blue (135 nm) to red (256 nm). We see that we obtain solutions with smaller particles at high centrifugation time and that the influence of molarity on the average diameter is significant for small centrifugation times but is much less significant when centrifugation times become longer.

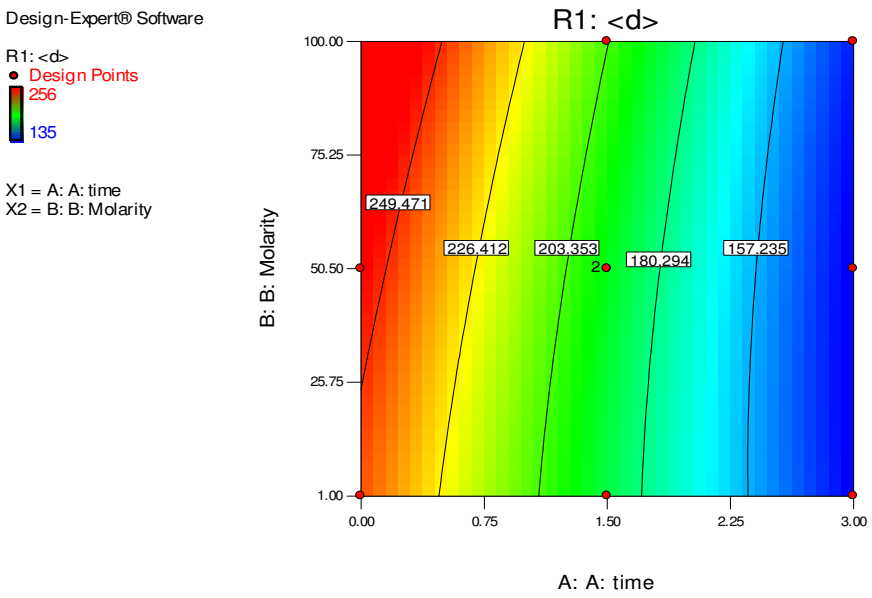

Fig. 4.13. Behavior of average particle diameter with molarity and centrifugation time.

It is seen that the dominant particle size in scattering measurements decreases with increasing centrifugation time. The average diameter of the nanoparticles as a function of centrifugation time and molarity is given by the regression model for the set 6 data. This equation can be inverted to obtain the centrifugation time necessary to obtain a particular average diameter as a function of molarity. The result is

Average diameter = 2.44.7 – 39.3*(centrifugation time) + 0.1*(molarity) (Eq. 4.1)

It should also be noted that the centrifugation and the measurements did not take place on the same day which means that there is no significant rate of re-aggregation of the particles, at least with respect to a time interval of a few days.

Fig. 4.14 contains the DLS measurements for three different solutions centrifugated for 0 minutes (green), 1 minute (red), and 3 minutes (blue). One can see that the apparent particle

diameter for the zero and one minute centrifugation time solutions is greater than for three minute centrifugation time.

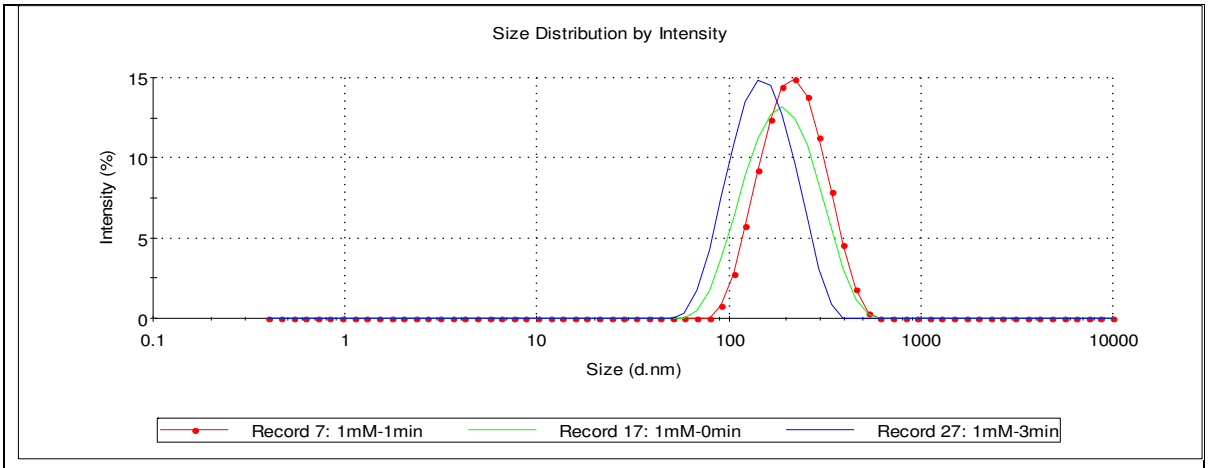

Fig. 4.14. DLS graphs for centrifugated titania solutions.

We will now perform a new set of depositions with centrifugated titania solutions and measure the Rayleigh slope hoping to have reduced it significantly. For all the experiments of the next set the titania solutions were centrifugated for 10 minutes.

4.8 Response Surface Experiment (set 7)

We now conduct a set of experiments with titania films that have been created from centrifugated colloidal solutions. All solutions were prepared at 100mM before centrifugating and all were centrifugated at 6000g. This response surface experiment included 40 films divided into two blocks. The molarity of PDDA was 10mM. The factors and their levels are shown in Table 4.18.

FACTOR (Units)	**RANGE**
pH	7 – 9
Wash time per side (min)	1 – 2
Centrifugation time (min)	2 – 10
Number of bilayers (categorical)	5 – 8

Table 4.18. Factors and levels for set 7.

The three responses for this set of experiments were Rayleigh slope, film thickness, and film index of refraction.

4.8.1 Rayleigh Slope

The ANOVA table for the Rayleigh slope is shown in Table 4.19.

Source	Sum of Squares	df	Mean Square	F Value	p-value Prob > F	
Block	1.73E-05	1	1.73E-05			
Model	4.86E-05	4	1.21E-05	19.26	< 0.0001	significant
pH	9.11E-06	1	9.11E-06	14.44	0.0006	
C-time	3.35E-05	1	3.35E-05	53.12	< 0.0001	
Bi-layers	2.55E-06	1	2.55E-06	4.04	0.0523	
pH*pH	3.43E-06	1	3.43E-06	5.44	0.0258	
Residual	2.14E-05	34	6.31E-07			
Lack of Fit	1.63E-05	26	6.26E-07	0.97	0.5604	not significant
Pure Error	5.16E-06	8	6.45E-07			

Table 4.19. ANOVA table for Rayleigh slope, set 7.

The model is a better description of the data than the overall average of the data ($p<0.0001$) and the model provides a good fit for the data (Lack of fit is insignificant). The linear terms for pH and centrifugation time are quite significant while the quadratic term for pH is moderately significant. The number of bilayers has a p-value that is close to the cut-off. We include it in the model in order to see how it affects the response. The fact that the linear term in number of bilayers is not significant is evidence that the diffuse scattering is mainly due to surface roughness, but again the range of the number of bilayers was not large enough to provide convincing evidence. Fig. 4.15 is a contour plot of the Rayleigh slope versus centrifugation time and pH with the color code going from low (blue) to high (red). This, when taken with the reduction in the average particle diameter with centrifuge time (Fig. 4.13), is convincing evidence that the diffuse scattering from our films is primarily due to aggregation of the nanoparticles in our colloidal solutions.

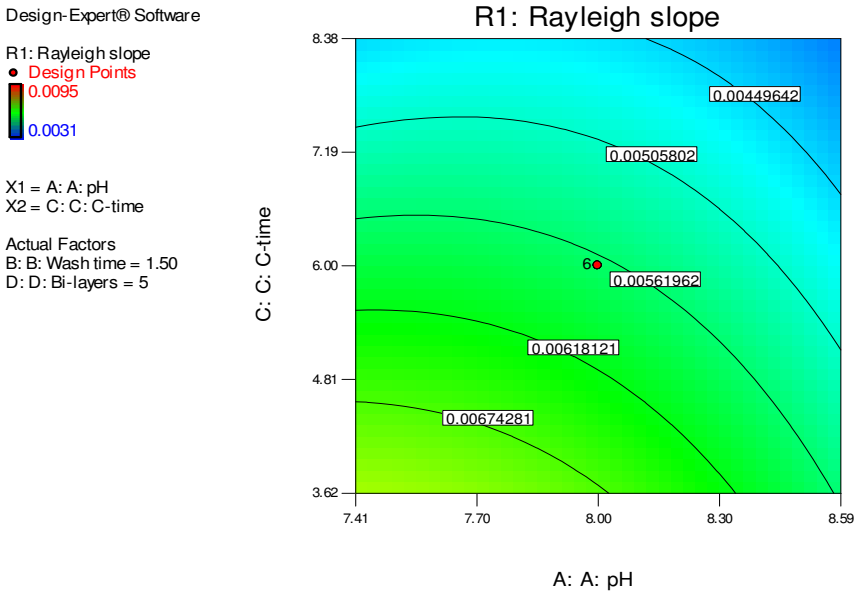

Fig. 4.15. Interaction of pH*centrifugation time with respect to the Rayleigh slope, set 7.

The Rayleigh slope also decreases with increasing pH which is probably due to the fact that the film thickness decreases with increasing pH (discussed in next section).

4.8.2 Film Thickness

The Ellipsometry data for films of set 5 were extensively analyzed using three different models. The Cauchy model yielded reasonable fits but it sets extinction equal to zero which is not consistent with the loss of incident intensity due to diffuse scattering. EMA was a good model for silica nanoparticle films, but provided poor fits to the Ellipsometry data for titania nanoparticles films as seen in Fig. 1.6.

The Lorentz model is relatively simple, takes into account absorption, and gave the best qualitative fit to the Ellipsometry data. For these reasons we used the Lorentz model to determine the thickness of set 7 films. The ANOVA table for the film thickness response is shown in Table 4.20.

Source	Sum of Squares	df	Mean Square	F Value	p-value Prob > F	
Block	2.74E+04	1	2.74E+04			
Model	1.17E+05	2	5.83E+04	14.35	< 0.0001	significant
pH	1.04E+05	1	1.04E+05	25.49	< 0.0001	
pH*pH	1.30E+04	1	1.30E+04	3.21	0.0817	
Residual	1.46E+05	36	4.06E+03			
Lack of Fit	1.15E+05	28	4.10E+03	1.04	0.5129	not significant
Pure Error	3.14E+04	8	3.93E+03			

Table 4.20. ANOVA table for film thickness (Lorentz model), set 7.

The model is a better description of the data than the overall average of the data ($p<0.0001$) and the model provides a good fit for the data (Lack of fit is insignificant). Only the linear pH term is significant; a plot of film thickness versus pH is shown in Fig. 4.16.

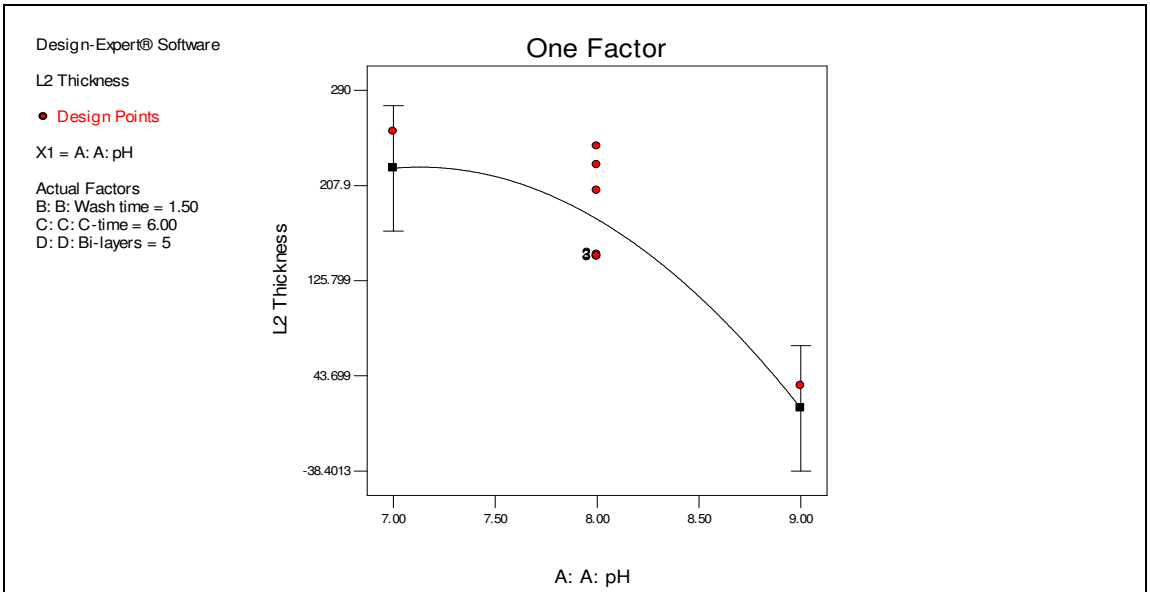

Fig. 4.16. Effect of pH on film thickness, set 7.

Lower pH values produce thicker films. This result is consistent with our previous observation that the decrease in Rayleigh slope with increasing pH values is due to the fact that the films are thinner at high pH.

We see that a film deposited from colloidal solution having a pH between 7 and 7.5 gives the thickest film. We also need to know the thickness as a function of the number of bilayers in order to create quarter wave stacks. But in the ANOVA analysis of thickness, number of

bilayers was not a statistically significant term. If we include number of bilayers in the ANOVA regression model for thickness, then the equation for thickness versus pH and number of bilayers is

$$\text{Thickness} = 178.81 - 61.57*\text{pH} + 15.52*\text{bilayers} - 21.08*(\text{pH})^2 \quad \text{(Eq. 4.2)}$$

We will use this equation in the next chapter to design the quarter wave stack.

4.8.3 Index of Refraction

In addition to information about titania nanoparticle film thickness we require information about the titania film's effective index of refraction in order to design the quarter wave stacks. The Lorentz model for the Ellipsometry data gives the index of refraction as a function of the response factors and the wavelength. In order to estimate the dependence of the index of refraction just on response factors, we modeled the ellipsometry data using the Lorentz model and found that pH is the only significant term in the regression model of the titania film's refractive index. A plot of the average refractive index versus pH is shown in Fig. 4.17.

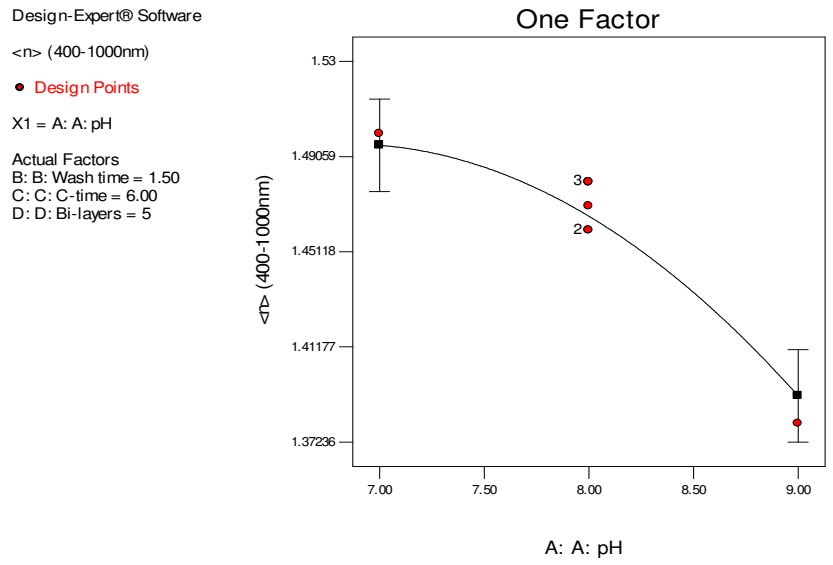

Fig. 4.17. Effect of pH on film refractive index calculated using the Lorentz model on ellipsometry data, set 7.

The pH is approximately 1.48 in the pH range 7 to 7.5.

4.8.4 AFM Images

AFM images for some of the films from set 7 (centrifugated colloidal solutions) were compared with the AFM images of films from set 6 (uncentrifugated colloidal solutions) and it was found that the surfaces were indeed much smoother. An image of film 16 from set 7 is shown in Fig. 4.18. The RMS roughness of this film is 19.2nm which is considerably smaller than the smallest RMS roughness value of the samples from set 6 shown in Table 4.15.

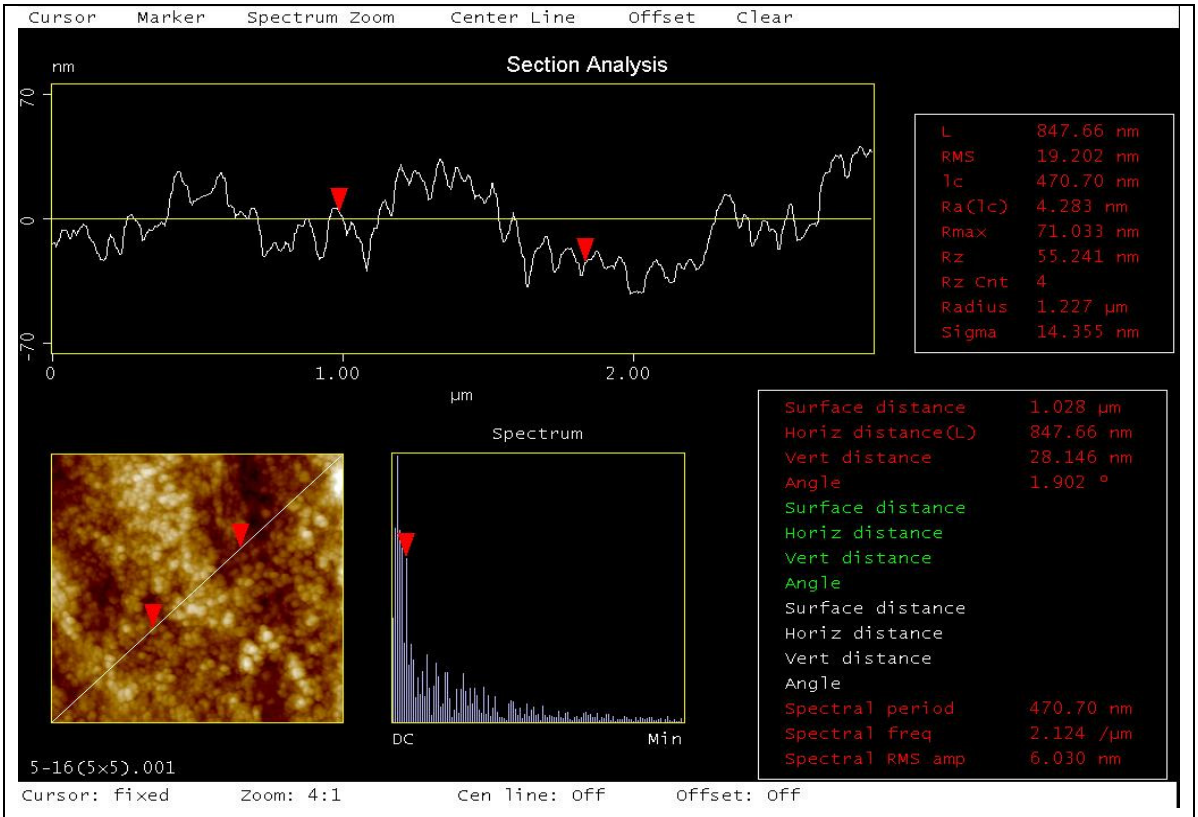

Fig. 4.18. AFM image (bottom left) of film 16, set 5. Surface section and Fourier coefficients are also shown.

All these considerations lead us to believe that centrifugation is very effective process for reducing the contribution of surface roughness to diffuse scattering.

4.9 Absorption

The absorption of incident light intensity was discussed to some extent in Section 1.2.4 and will be considered in more detail here.

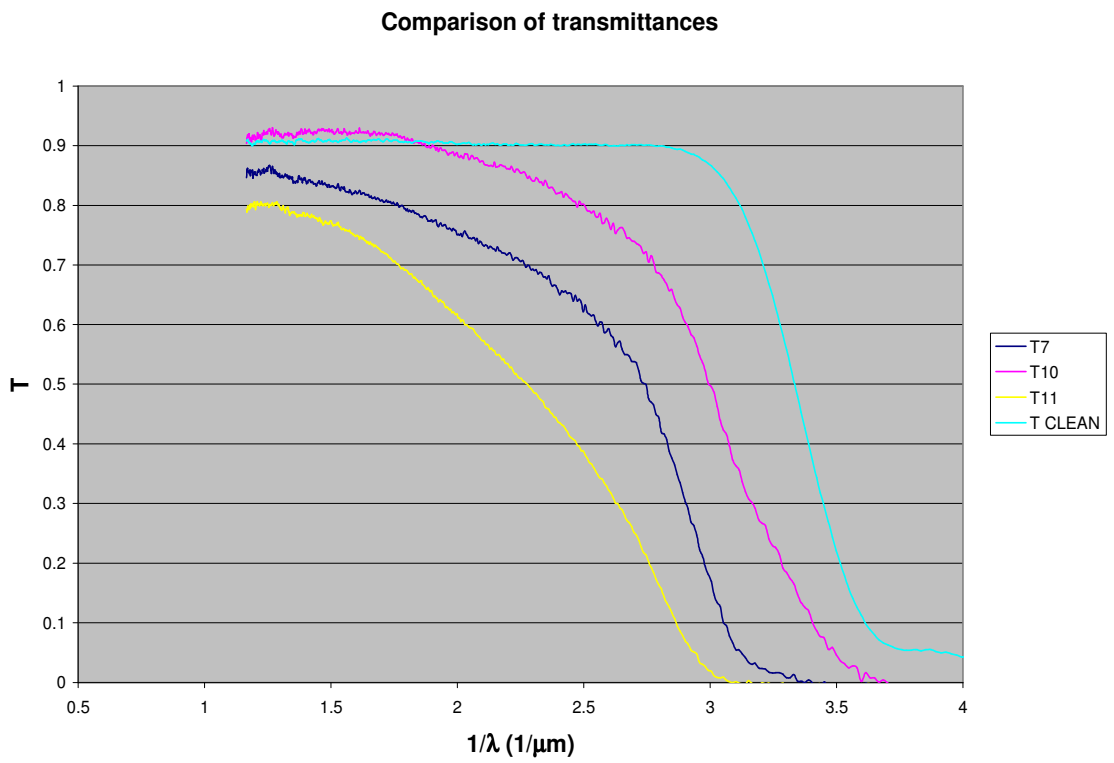

Fig. 4.19. Transmittance (T) vs. 1/λ for films 7 and 10 (set 7, blue and pink lines), film 11 (set 6, yellow line) and clean glass slide (light blue line).

The transmittance (T) versus 1/λ is shown in Fig. 4.19 of one film from set 6 (T11, uncentrifugated colloidal solutions), two films from set 7 (T7 and T10, centrifugated colloidal solutions) and the glass substrate (light blue). The sharp drop in the transmittance of the clean glass substrate at $1/\lambda = 3.2\ \mu m^{-1}$ is the signature of a sharp band edge. The transmittance of T11, the uncentrifugated film, falls off monotonically without a sharp edge as a consequence of diffuse scattering. The transmittances of T7 and T10, the centrifugated films, fall off more slowly than the transmittance of T11 and have a relatively sharp edge at $1/\lambda = 3.0\ \mu m^{-1}$ consistent with a much lower level of diffuse scattering in the centrifugated films. But the question still remains open whether the fall off in transmittance in the centrifugated films below $1/\lambda = 3.0\ \mu m^{-1}$ can be attributed entirely to diffuse scattering or whether there is a contribution to

the drop in transmittance from true absorption in the titania nanoparticles due to their finite optical conductivities at these wavelengths.

4.10 Summary of Results on Titania Film Experiments

Before continuing with the quarter wave stack, let us summarize what we have found so far from the seven sets of experiments involving titania films:

- PDDA is the polycation of choice because its ionization is independent of pH. pH is the most important factor for film deposition. A value between 7.0 and 7.5 seems optimum for maximizing film thickness and index of refraction, and minimizing diffuse scattering. This range of values is higher than the isoelectric point of our titania nanoparticles assuring that they carry a significant negative surface charge during the deposition process.
- Film quality is weakly dependent on the molarities of the titania solution between 100mM and 1000mM.
- Wash time is not a statistically important term in the range between 1 and 3 minutes.
- Dipping time is also not statistically significant. The three minute dip time that we used is certainly sufficient. To shorten the duration of the experiments a two minute dip time can be used.
- Centrifugating the titania solutions for 10 minutes at 6000g significantly reduces the average diameter of the titania nanoparticles and hence leads to deposition of films with minimized diffuse scattering. The reduction of surface roughness by centrifugation of the colloidal solution was verified by AFM.
- Modeling the ellipsometry data is problematic. The Lorentz model is better than the EMA or Cauchy models, but is not entirely satisfactory.

Having reduced diffuse scattering significantly by optimizing deposition conditions and by centrifuging the titania solutions for 10 minutes at 6000g we are now ready to proceed to the construction of a quarter wave stack from silica and titania layers.

References for Chapter Four

1 J. Choi and M. F. Rubner, "Influence of the degree of ionization on weak polyelectrolyte multilayer assembly," Macromolecules **38** (1), 116-124 (2005).

CHAPTER FIVE

Results for a Quarter-Wave Stack

The objective of this thesis is to broaden the region of low reflectivity, relative to the region of minimum reflectivity of a single layer film, by using the geometry of a two layer quarter-wave stack (QWS) which was described in Section 1.2.2. We chose 500nm as our center wavelength which means that the optical thicknesses of both the silica and titania layers should be 125nm. The order of layers was chosen so that the high index material, titania, was in contact with the glass slide and the low index material, silica, was in contact with air; a geometry known as an HL QWS. We used a factorial design experiment to explore the influence of process factors on various characteristics of the QWS. In particular, we wanted to know whether the interface between the titania and silica layers contributed significant diffuse scattering that was in addition to the individual contributions from each layer.

5.1 Factorial Experiment

5.1.1 Design Details

The factorial experiment consisted of three factors with a center point that is the end points plus the mid point. Each factor level was replicated twice and the center point was replicated 8 times giving 24 runs that were split into two blocks of 12 runs each. In one block, the films were deposited by hand dipping the glass slides and in the other block the films were deposited by machine dipping. In principle, the dipping machine removes the systematic error associated with the different ways that individuals hand dip the slides. Since the blocking runs are not randomized, we can not draw statistical inferences regarding the difference between hand and machine dipping. But we can look for qualitative differences between the data in the two blocks. The ranges of the factors were based on the optimum deposition conditions for a single titania layer film discussed in Chapter 4. The factors and factor levels are shown in Table 5.1.

FACTORS AND BLOCKING (Units)	LEVELS (low, high)
Blocks	Hand dipping, machine dipping
A: pH of all solutions	7.5, 9
B: Molarity of silica (mM)	350, 3500
C: Wash time per side (min)	1, 2
Table 5.1. Factors and their levels for the quarter-wave stack factorial experiment.	

The molarity of silica levels were chosen to correspond with molarities used by Yancey et al.[1] We used Snowtex ST-20L silica solutions with 45nm average particle diameter. All titania solutions are prepared by centrifugating an initially 100mM titania nanoparticle solution for 10 minutes at 6000g.

The thickness per bilayer and index of refraction of the silica layer are 25nm per bilayer and 1.3, respectively. Therefore, to obtain an optical thickness near 125 nm, we deposited 4 bilayers of silica nanoparticles giving an optical thickness of 130 nm. The thickness per bilayer and index of refraction of the titania layer are 22 nm and 1.5, respectively, where the value of the index of refraction is a rough average over the visible range of wavelength. In order to obtain an optical thickness close to 125 nm would require 4 bilayers, but instead, 5 bilayers were deposited giving an optical thickness of 160nm. The reason for the choice for the number of bilayers is that from the first seven sets it appeared that four bilayers were not enough for the film thickness to start increasing linearly with the number of bilayers. The optical thicknesses of the silica and titania layers are not optimized for an ideal QWS, but the theoretical models that we have constructed to predict the reflectance of our QWS can accommodate any optical thickness of the silica and titania layers. Therefore, we can still determine how closely our measured reflectance agrees with theoretical predictions.

5.1.2 Rayleigh Slope

Once again the Rayleigh slope provides a measure of diffuse scattering and we want to see how the different factors affect it. The ANOVA table of this response is shown in Table 5.2.

Source	Sum of Squares	df	Mean Square	F Value	p-value Prob > F	
Block	2.16E-06	1	2.16E-06			
Model	5.51E-05	2	2.75E-05	11.92	0.0004	Significant
pH	3.25E-05	1	3.25E-05	14.07	0.0014	
molarity	2.26E-05	1	2.26E-05	9.77	0.0056	
Curvature	6.45E-06	1	6.45E-06	2.79	0.1110	not significant
Residual	4.39E-05	19	2.31E-06			
Lack of Fit	3.77E-05	13	2.90E-06	2.83	0.1046	not significant
Pure Error	6.16E-06	6	1.03E-06			

Table 5.2. ANOVA table for Rayleigh slope, quarter-wave stack.

The model is a better description of the data than the overall average of the data ($p = 0.0004$) and the model provides a good fit for the data (Lack of fit is insignificant). The main effects of pH and molarity are significant, but the main effect of wash time and all interactions are insignificant. In Figures 5.1 A and B are plots of Rayleigh slope versus pH and molarity, respectively. As observed for single layer titania films, Fig 4.7, the Rayleigh slope decreases with increasing pH and depends weakly on molarity. The deposition of the silica layer on top of the titania layer did not change the dependence of the Rayleigh slope on pH and molarity between the single layer titania films and the quarter-wave stacks.

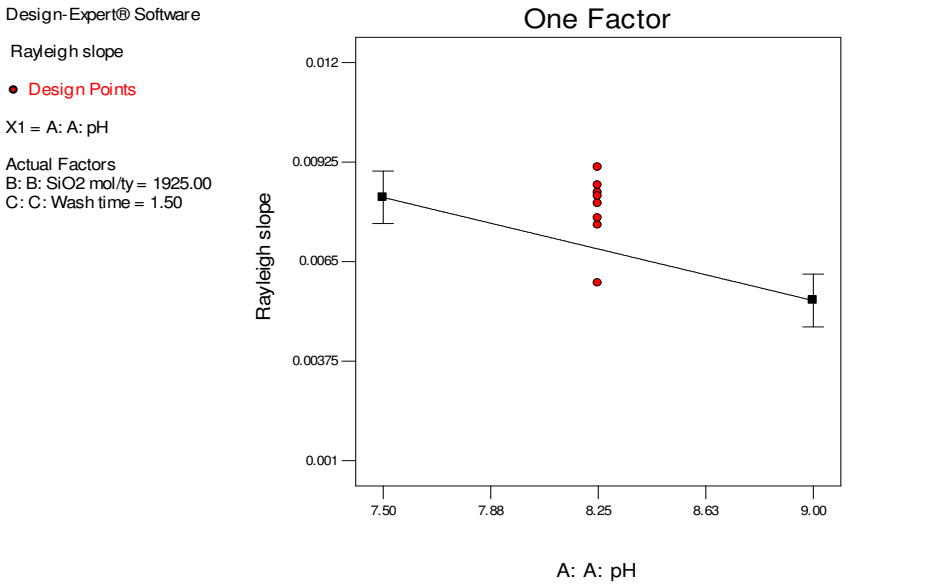

A

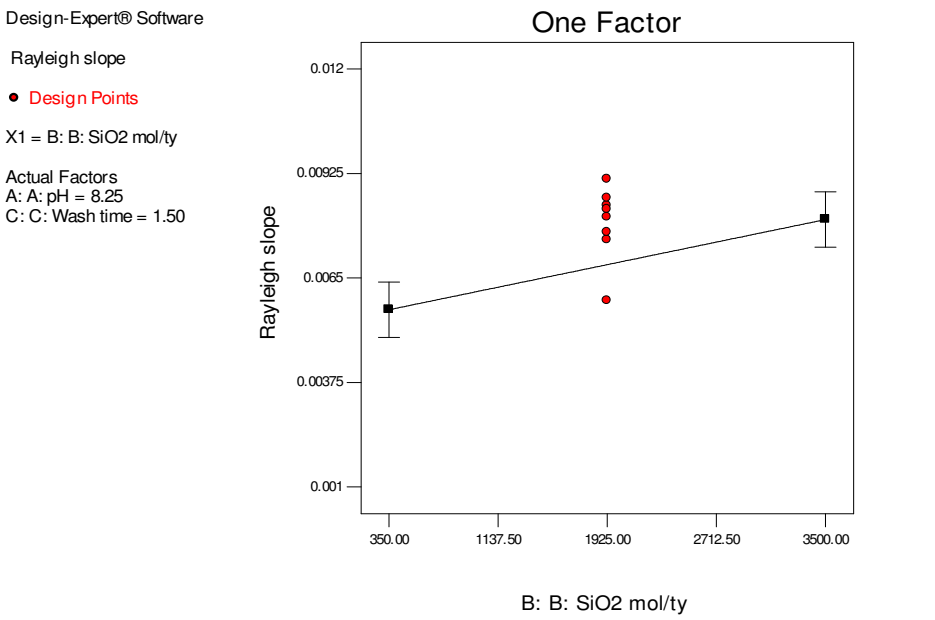

B

Fig. 5.1. Rayleigh slope vs. pH with silica molarity = 1925mM and wash time = 1.5min (A) and Rayleigh slope vs. silica molarity with pH = 8.25 and wash time = 1.5min (B).

5.1.3 Thicknesses / Refractive Indices

The thicknesses and indices of refraction of the individual silica and titania layers in the quarter-wave stacks was measured by Ellipsometry. The Lorentz model was used for the titania layer, taking its parameters from the analysis of the single titania layer films, while EMA was used to model the silica layer since it had been used quite successfully by Yancey et al.[1] to model their data.

There were no significant factors or factor interactions from the ANOVA analysis for the thickness of titania, while the main effect of pH was moderately significant for influencing the thickness of silica. There also were no significant factors from the ANOVA analysis of the refractive index of the titania layer. This is consistent with the results for the single layer titania films where the pH term was only moderately significant and the molarity term was insignificant.

5.1.4 Effect of Blocking on Rayleigh Slope

The slides in block 1 of this experiment were hand dipped while the slides in block 2 were machine dipped. We can qualitatively assess whether the Rayleigh slope is different for hand and machine dipping by plotting Rayleigh slope versus pH and color coding whether the data points are from block 1 or 2 (Fig. 5.2).

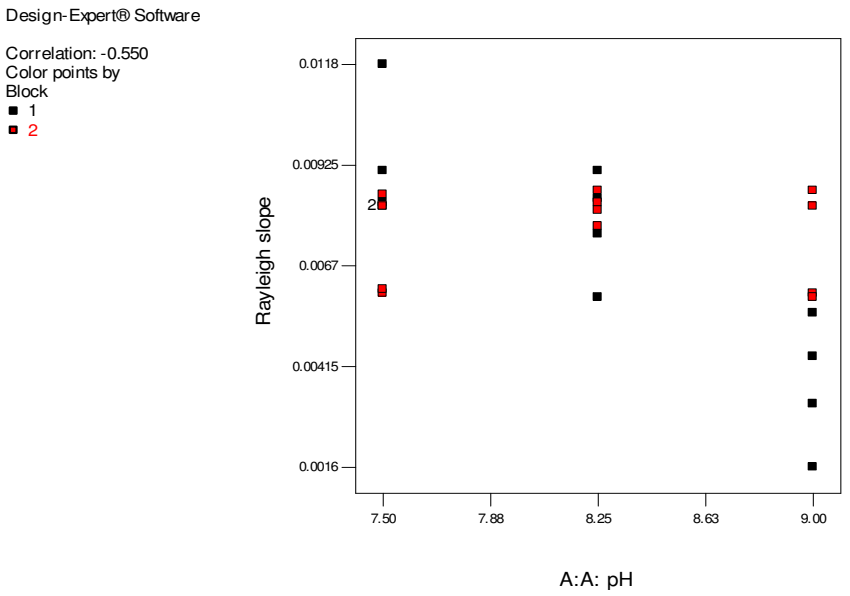

Fig. 5.2. Effect of dipping machine on diffuse scattering. Black squares correspond to hand dipped films, red squares to machine dipped films.

In this figure, black data points are from block 1 (hand dipped) and red data points are from block 2 (machine dipped). There clearly is an interaction between blocks and pH. The hand dipped slides have a larger Rayleigh slope at low pH and a smaller Rayleigh slope at high pH. Further experiments are necessary with the dipping technique a categorical factor in order to draw statistically valid inferences regarding the influence of the dipping technique on the Rayleigh slope. Next, we consider SEM images of the films.

5.1.5 SEM Images

After the optical measurements were taken, we obtained a SEM image of sample 11 shown in Fig. 5.3. A thin layer of gold must be plated on the film since it is non-conducting and, without the conducting layer, charge would accumulate on the film from the incident electron beam causing the beam to be unstable. Information is also provided in the figure on the elements in the film and on the substrate. Since the penetration depth of the electron beam is of order 1μm, the relative contributions of different impurities is heavily weighted by those in the substrate and, therefore, this information is not very useful. The surface does not appear irregular and there appear to be no bare spots on the slide which is very encouraging since it is not clear a priori how well silica layers will deposit on titania layers by ISAM.

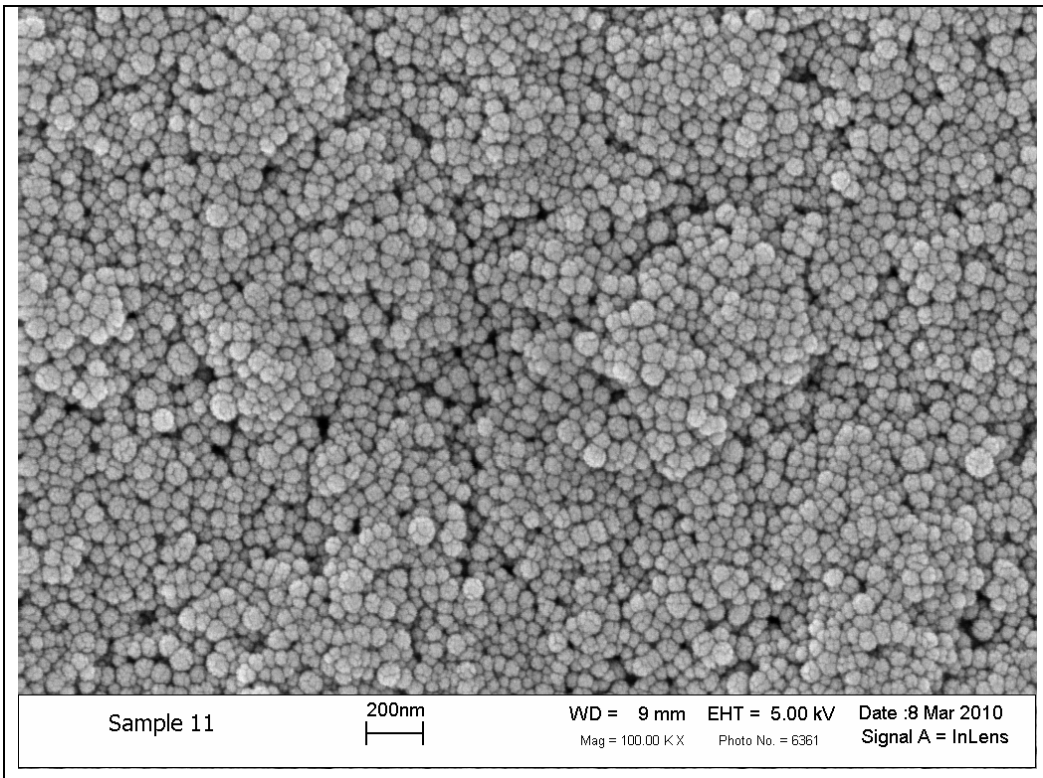

Standard :

C CaCO3 1-Jun-1999 12:00 AM

O SiO2 1-Jun-1999 12:00 AM

Na Albite 1-Jun-1999 12:00 AM

Mg MgO 1-Jun-1999 12:00 AM

Si SiO2 1-Jun-1999 12:00 AM

Ca Wollastonite 1-Jun-1999 12:00 AM

Ti Ti 1-Jun-1999 12:00 AM

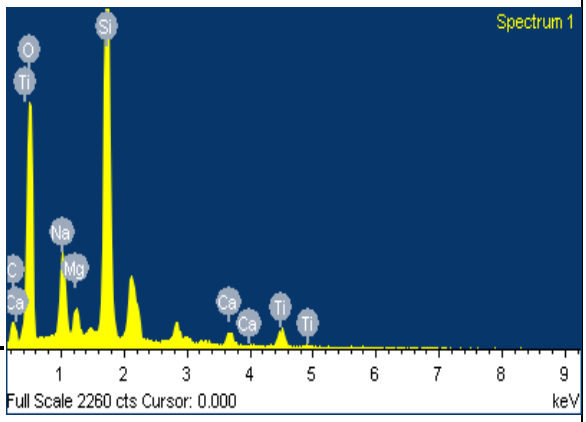

Element	Weight%	Atomic%
C K	8.17	13.77
O K	40.13	50.81
Na K	5.80	5.11
Mg K	1.90	1.59
Si K	33.06	23.84
Ca K	3.18	1.61
Ti K	7.75	3.28
Totals	100.00	

Fig. 5.3. SEM images and composition of quarter-wave stack 11.

5.1.6 Qualitative Analysis of Reflectance and Transmittance Plots

We now partition the 24 measurements of reflectance and transmittance from the quarter-wave stacks into three groups shown in Figures 5.4, 5.5, and 5.6, based on the value of pH (low level, center level, and high level). The two groups with low (7.5) and high (9.0) pH are partitioned further into two subgroups (Figures 5.4 and 5.6) of low (350mM) and high (3500mM) molarity levels while the group (Fig. 5.5) based on the center level of pH (8.25) is not partitioned further (molarity = 1925mM). We note again that absorbance in the film becomes significant for $1/\lambda > 2.5\mu m^{-1}$ which is marked by an arrow in the reflectance plots Figures 5.4 through 5.6.

Our first observation based on these figures is that there appears to be a positive correlation between the rate that the transmittance and reflectance fall off with $1/\lambda$. For example, the transmittances for samples 5 and 11 fall off more rapidly than the transmittances for samples 15 and 19 (Fig. 5.4 B). The same ordering in the rate of fall off is seen in the reflectance (Fig. 5.4 A, R5 and R11 versus R15 and R19). Similarly, the transmittance T12 in Fig. 5.4 D falls off more rapidly than the transmittances T2, T13, and T16 and again the same ordering is seen in the reflectances (Fig. 5.4 C, R12 versus R2, R13, and R16). This correlation in fall off between transmittance and reflectance is not as clear for the center point (Fig. 5.5), but reoccurs at high pH (Fig. 5.6; compare transmittance measurements T7 and T9 versus T20 and T23 with reflectance measurements R7 and R9 versus R20 and R23). We argue that this correlation is further evidence that the diffuse scattering is primarily due to surface roughness. If the surface were smooth, but the bulk of the film were inhomogeneous, then specular reflection would occur from the surface and be independent of $1/\lambda$, while the transmitted beam would be increasingly attenuated by diffuse scattering with increasing $1/\lambda$.

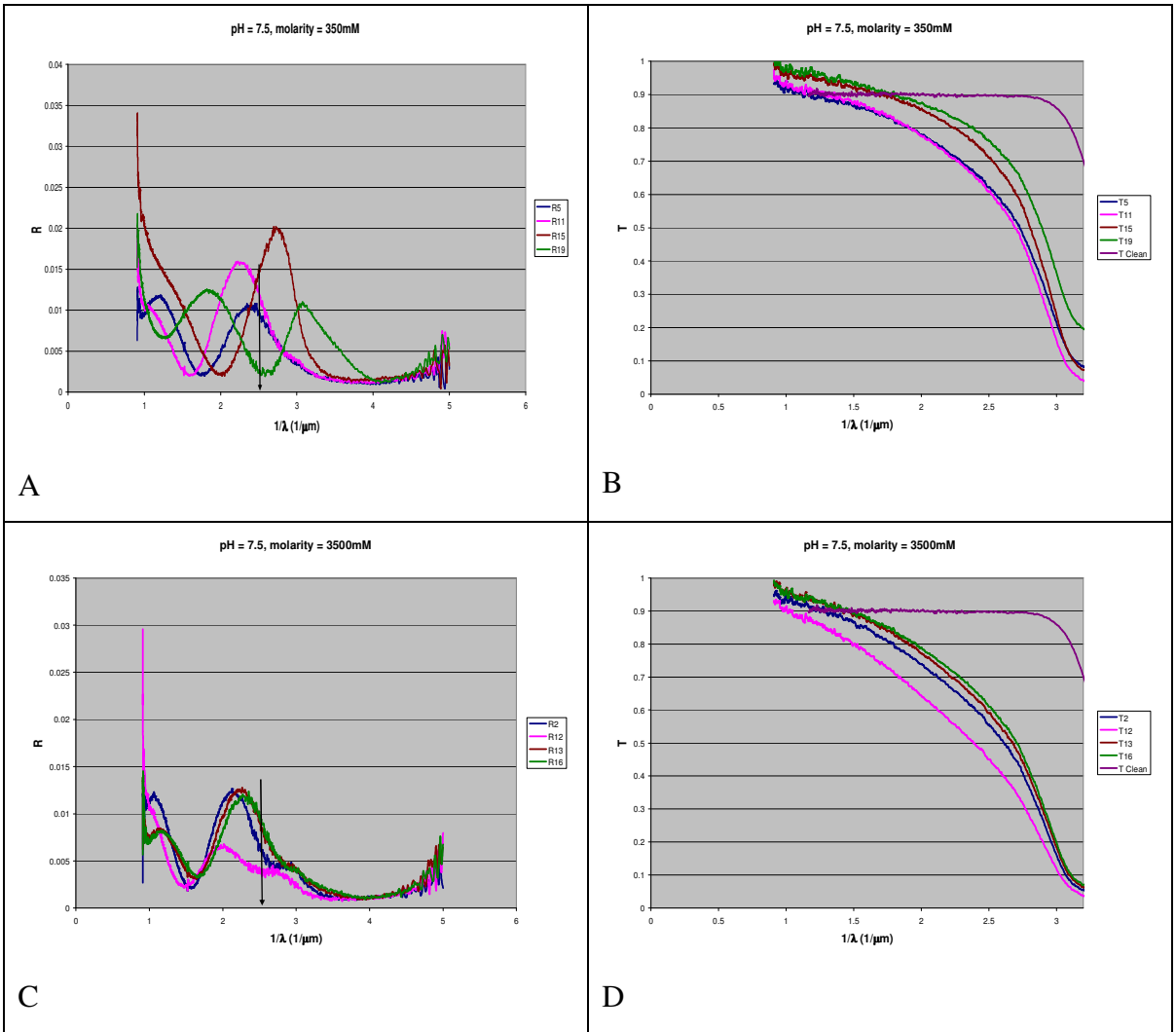

Fig. 5.4. Reflectances (left column, A and C) and transmittances (right column, B and D) for all quarter-wave stack with pH = 7.5 with low molarity (top row, A and B) and high molarity (bottom row, C and D). The arrow indicates the boundary for significant absorption.

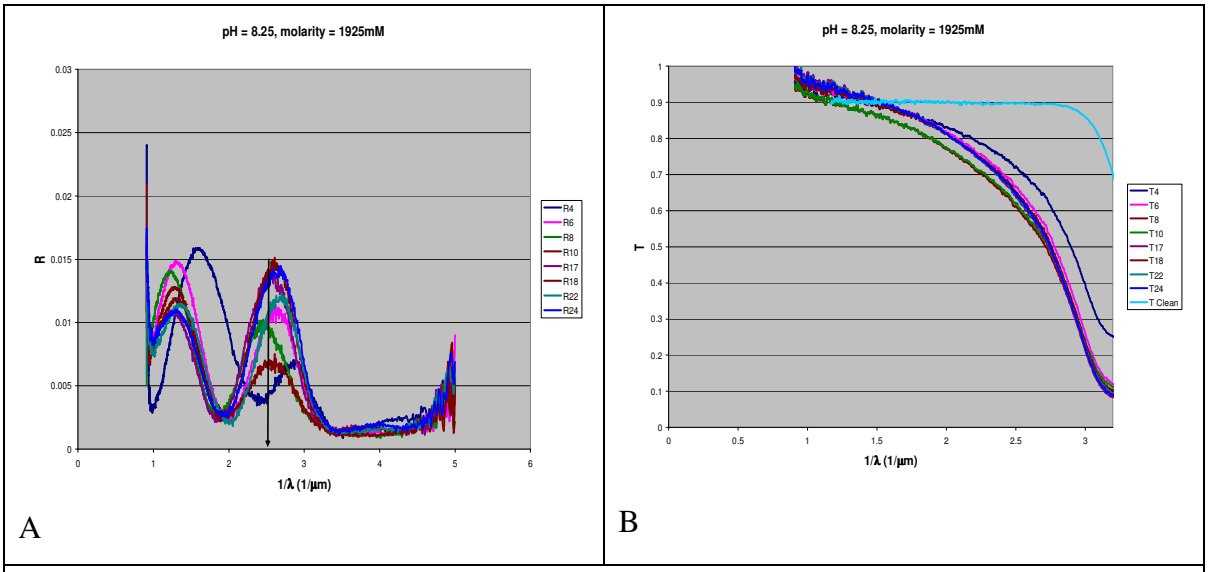

Fig. 5.5. Reflectances (A) and transmittances (B) for all quarter-wave stacks with pH = 8.25. All silica solutions were 1925mM. The arrow indicates the boundary for significant absorption.

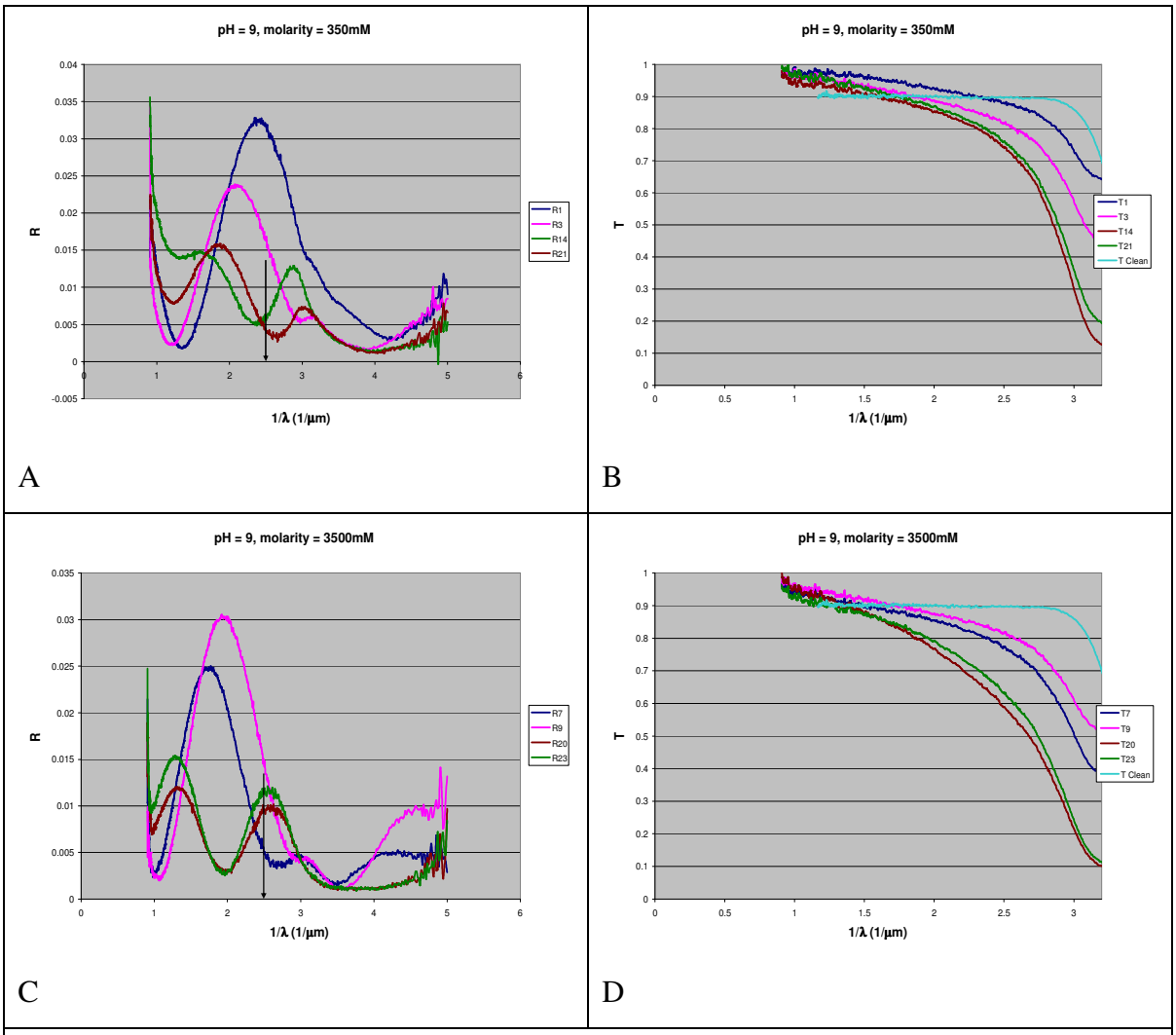

Fig. 5.6. Reflectances (left column, A and C) and transmittances (right column, B and D) for all quarter-wave stack with pH = 9 with low molarity (top row) and high molarity (bottom row). The arrow indicates the boundary for significant absorption.

Our second observation is based on the phases of the interference fringes in the reflectances; that is, on the positions of reflectance minima and maxima with respect to 1/λ. The phase of the reflectance fringes depends on the optical thicknesses of the silica and titania layers. According to the ANOVA analysis (section 5.1.3), the optical thickness of the titania layer did not depend on any of the factors while the optical thickness of the silica layer depended only on pH. This would imply that the phases of the interference fringes within the Figures 5.4 A and C (pH = 7.5), Fig. 5.5 (pH = 8.25), and Figures 5.6 A and C (pH = 9.0) would be the same, but the

fringes would shift as one went from Figures 5.4 A and C to Fig. 5.5 to Figures 5.6 A and C as one would expect thicker films for lower pH values. It appears clear that this implication is not true, but in order to test this inference further, we identified the values of $1/\lambda$ where the first maximum and the second minimum of reflectance occur in Figures 5.4 A and C, Fig. 5.5, and Figures 5.6 A and C and used them as responses in our factorial design. The ANOVA results for both responses were that the only statistically significant factor was the molarity of silica with pH having a borderline p-value. But the overall averages for both responses represented the data better than a regression model based on the significant main effects. In addition, the regression models for both responses had significant lack of fit. One possible reason that the models for the interference maxima and minima were not significant and that there was significant lack of fit with the regression models for the two responses is that the blocking factor was introducing significant and systematic variability. We assessed whether the observed variability in phase, where it should not be present, could be a consequence of the different dipping techniques from block 1 to block 2. In Figures 5.4 through 5.6, those measurements from block 1 are numbered 1-12 while measurements from block 2 are numbered 13 to 24. We are unable to see a consistent correlation between phase and dipping technique in the data and infer that the dipping technique, though it may be introducing some variability in the interference phase, is not the only source of systematic variability. We are collaborating with Dan Mazilu at Washington and Lee University on further experiments to identify the source or sources of the unexplained variability.

5.2 Comparison between Model Calculation and Reflectance Measurements

The model for the reflectance of a two layer HL quarter-wave stack is described in Section 1.2.2. The parameters of the model are the thicknesses and complex refractive indices of both the titania and the silica layers that are obtained by ellipsometry for each layer separately using the Lorentz model for the titania layer and EMA for the silica layer. As discussed in section 1.2.5, the loss of incident intensity due to diffuse scattering is not properly taken into account in the Lorentz model of the titania layer and, as a consequence, the measured reflectance is expected to be lower than the model prediction with the discrepancy increasing with increasing $1/\lambda$. The locations of the interference fringes in R should be less affected by this shortcoming in the Lorentz model and, therefore, congruence of the measured and model fringes will be used as

the metric to assess the quality of the model fit. We should also note here that the model assumes a sharp boundary between the two layers of the quarter-wave stack. Since our films are composed of nanoparticles, some intermixing of titania and silica nanoparticles is inevitable at the interface and the assumption of a sharp boundary between layers is unrealistic. It is difficult to assess how the breakdown of this assumption will be evident in comparing the measured and model reflectances.

5.2.1 Model Fits

Instead of using the optical thicknesses of the titania and silica layers as fitting parameters in the QWS model, we set the optical thicknesses of the titania and silica layers to their nominal values of 160 nm and 130 nm, respectively, and compare our 24 measurements of reflectance, still grouped according to pH and silica molarity, with this single model. The corresponding graphs are shown in Figures 5.7, 5.8, and 5.9. Also marked on each graph is the model reflectance when $1/\lambda = 0$.

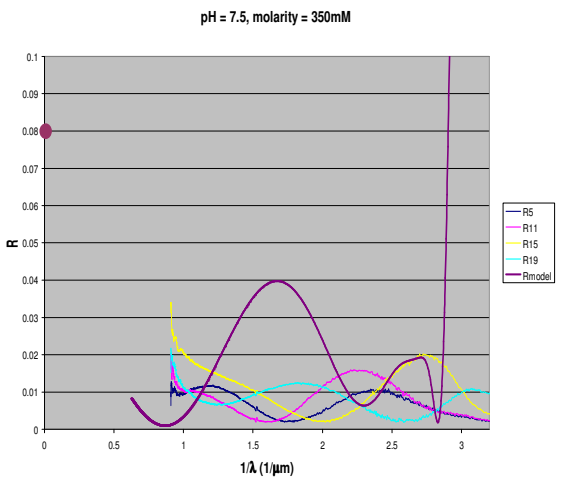

A

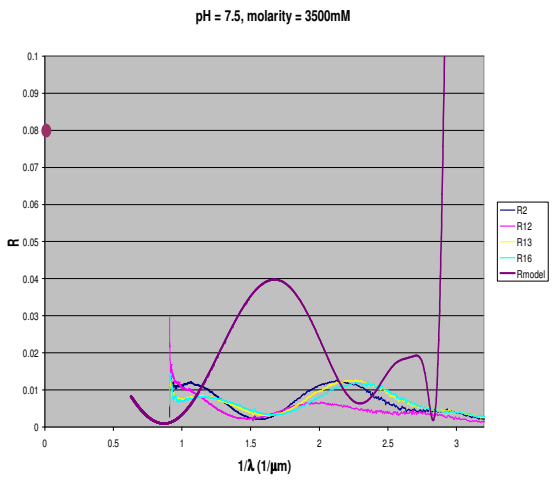

B

Fig. 5.7. Quarter-wave stack model and data for all quarter-wave stacks with pH = 7.5 with silica molarity low (A) and high (B). The point on the R-axis is the model reflectance when $1/\lambda = 0$.

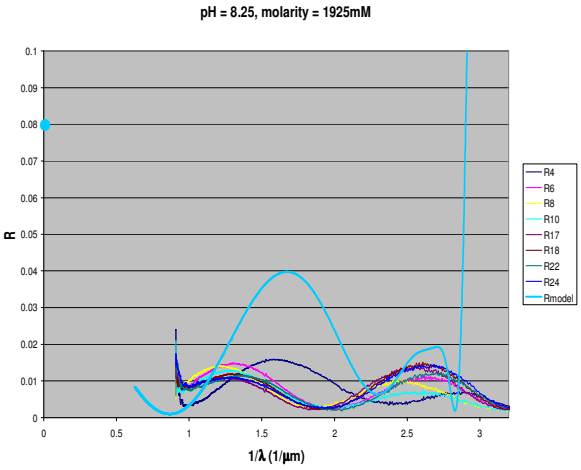

Fig. 5.8. Quarter-wave stack model and data for all quarter-wave stacks with pH = 8.25 with silica molarity equal to 1925mM. The point on the R-axis is the model reflectance when $1/\lambda = 0$.

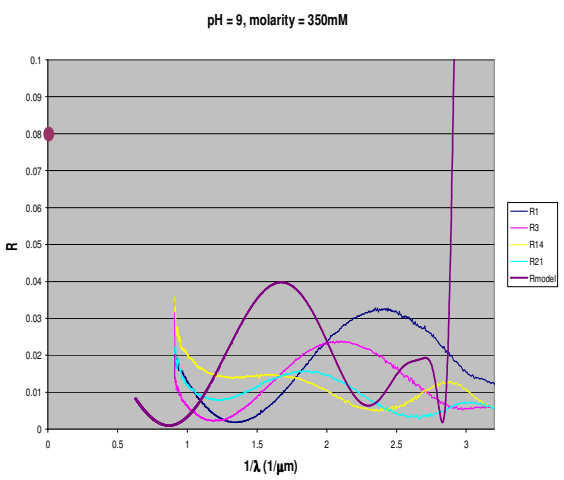

A

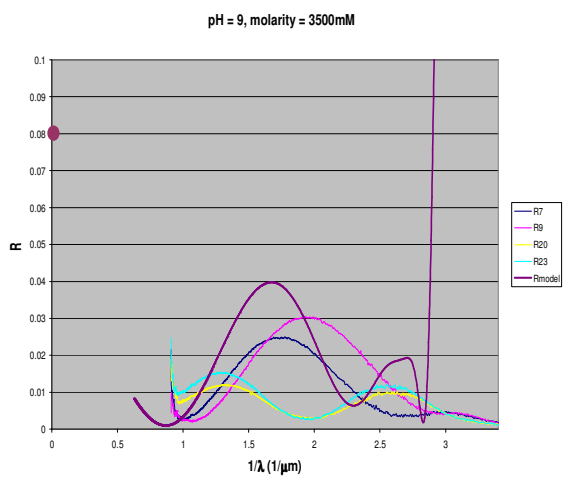

B

Fig. 5.9. Quarter-wave stack model and data for all quarter-wave stacks with pH = 9 with silica molarity low (A) and high (B). The point on the R-axis is the model reflectance when $1/\lambda = 0$.

It is difficult to judge the positions of interference fringes in the measured reflectance because absorption and diffuse scattering produce an envelope that creates false maxima. Also, the lack of data for $1/\lambda < 0.9\ \mu m^{-1}$ creates uncertainty in identifying the position of fringes in the long wavelength limit. In Fig. 5.7 A (pH = 7.5, molarity = 350mM), the positions of the fringes in R15 and R19 are in relatively good agreement with the model, but in the same figure, poor agreement exists between the model and fringes in R5 and R11. The frequency of the fringes in R5 and R11 appears to be higher than the frequency of model fringes suggesting that the optical thickness of one or both of the QWS layers is greater than its nominal value. The frequencies of all the measured fringes in Fig. 5.7 B (pH = 7.5, molarity = 3500mM) are higher than the frequency of the model fringes suggesting that the optical thicknesses of one or both layers in all these films are greater than their nominal thickness. In Fig. 5.8 (pH = 8.25, molarity = 1925mM), the frequencies of all the fringes, except those in R24, are higher than the frequency of the model fringes, while, in sharp contrast, the fringes of R24 are in excellent congruence with the model fringes. In Fig. 5.9 A (pH = 9, molarity = 350mM) the frequencies of all the fringes are less than the model frequency suggesting that the optical thicknesses of one or both layers in these films are less than the nominal value. In Fig. 5.9 B (pH = 9, molarity = 3500mM), the fringes from two films, R7 and R9, are shifted slightly higher in $1/\lambda$ relative to the model fringes,

but otherwise they are in good congruence with the model fringes. The frequencies of fringes in the other two films, R20 and R23, again are higher than the frequency of fringes in the model suggesting that the optical thicknesses of one or both layers in these films are greater than the nominal value.

The lack of a clear pattern relating the deposition conditions to the degree of agreement between measurement and model further supports the conclusion drawn in section 5.1.6 that there is variability in the deposition conditions being introduced by some unidentified factor or factors.

5.2.2 Quarter-Wave Stack Layer Thickness Estimates

We argued in the previous section that the optical thicknesses of one or both layers in the QWS were larger than the nominal optical thicknesses of the two layers. In order to explore this possibility further, we calculated from our model the reflectances of a series of QWS with the thicknesses of the silica layer varying from 70 nm to 140 nm (nominal silica thickness = 100 nm) and with the thicknesses of the titania layer (nominal titania thickness = 110 nm) being set 10% higher than the silica thickness. The results, R versus $1/\lambda$ for different silica thicknesses, are plotted in Fig. 5.10.

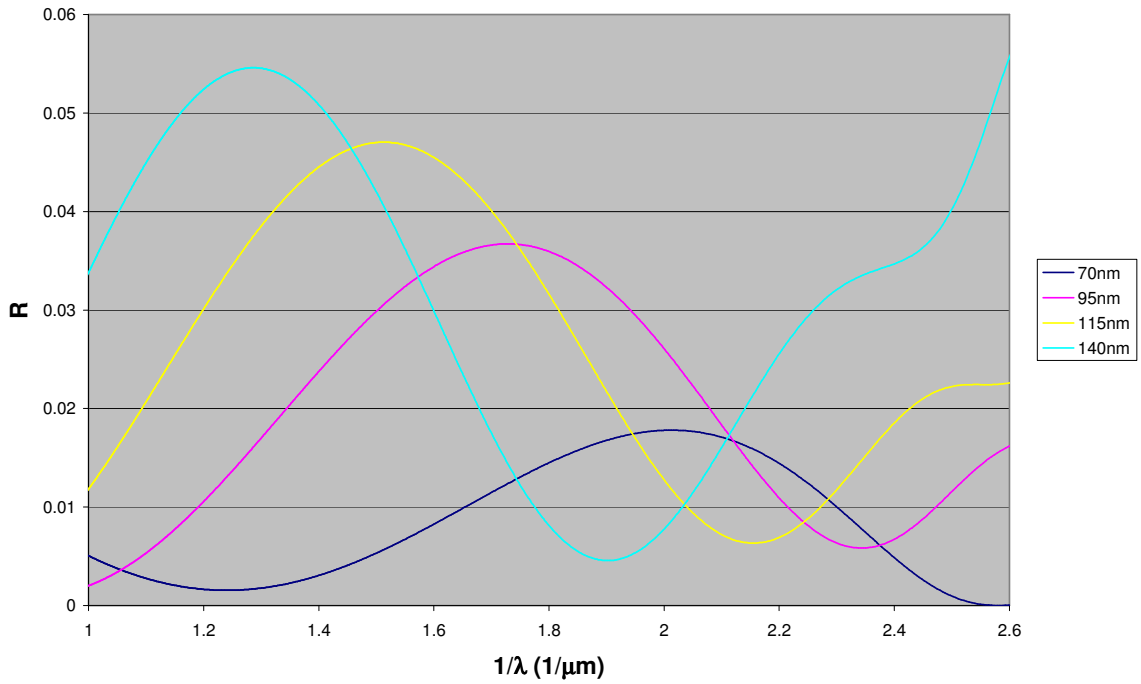

Fig. 5.10. Quarter-wave stack models with the silica layer thickness varying from 70nm to 140nm and the titania layer thickness equal to 1.1 times the silica layer thickness.

It is seen in this plot that the fringes shift to smaller values of $1/\lambda$ with increasing layer thickness and that the frequency of fringes increases as the thicknesses of the two layers increase. We plot in Fig. 5.11 the position of the first fringe maxima versus the silica layer thickness in order to estimate how small variations in a layers thickness will influence the position of a fringe. In some cases the fringes in Figures 5.7, 5.8, and 5.9 were shifting by of order 0.5 μm^{-1} corresponding to layer thickness variations of over 40 nm. This would correspond to a difference of order 50% in the average bilayer thickness. This seems unlikely. A more likely explanation is that the number of dipping cycles required to fill in the first bilayer was varying between films due to the unidentified factor in the deposition process. Further experiments will be required to test whether this hypothesis is true.

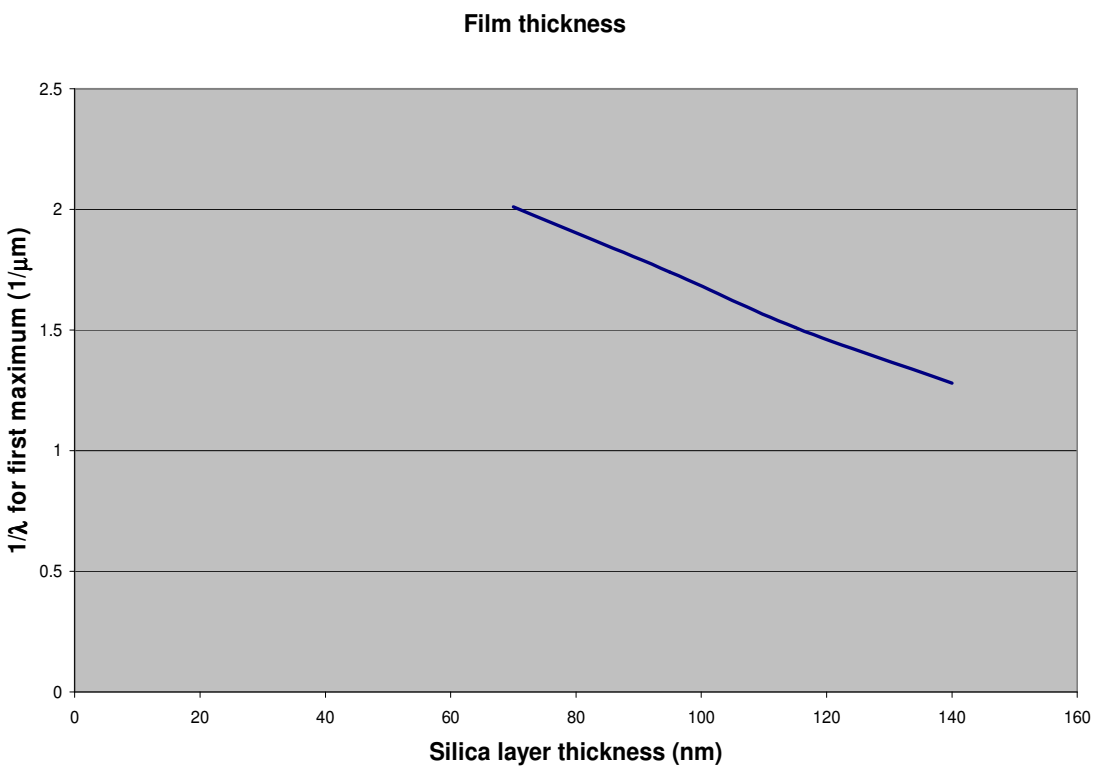

Fig. 5.11. Variation of the location of the first maximum in the reflectance model with silica layer thickness. The thickness of the titania layer is taken to be 1.1 times the thickness of the silica layer.

5.3 Summary of Results on Quarter-Wave Stacks

We summarize here what we have learned from this set of experiments on quarter-wave stacks.

- Construction of a quarter-wave stack consisting of one layer of titania nanoparticles and one layer of silica nanoparticles is possible by ISAM.
- There seems to be little intermixing of the two layers, titania and silica since the ellipsometry data of the composite film are modeled reasonably well by applying a separate model to each layer individually. Still, the model that we used assumes a sharp boundary between the titania and the silica layer and hence an improved model may be useful in the future.

- There appears to be an interaction between dipping method (hand dipping versus machine dipping) and pH although no statistical inferences can be drawn from our present data because block treatments are not randomized.
- The theoretical reflectance does not fit ideally the measured reflectance for any subset of the data. There must be additional factors that affect our results that we have not considered. This factor is possibly connected with the nanoparticle deposition in the first layer. A greater number of experiments is needed for further clarification.

References for Chapter Five

1 S. E. Yancey, W. Zhong, J. R. Heflin, and A. L. Ritter, "The influence of void space on antireflection coatings of silica nanoparticle self-assembled films," Journal of Applied Physics **99** (3) (2006).

CHAPTER SIX

Summary and Future Work

6.1 Summary

In this thesis we identified the source of diffuse scattering from a single layer titania nanoparticle film and explored the influence of several factors on the characterization of a quarter-wave stack consisting of one layer of titania nanoparticles and one layer of silica nanoparticles deposited on glass microscope slides by ISAM.

6.1.1 Titania Nanoparticle Films

The problem of diffuse scattering was extensively investigated and it was argued that it is mainly a surface effect, and not a film bulk effect, since film thickness was not a statistically significant factor. AFM images confirmed the fact that the titania nanoparticle films had rough surfaces. The surface roughness was measured by AFM and compared to the Rayleigh slope. The correlation between the two was weak. We approached this problem in two ways, one directed at the deposition conditions and the other directed at the titania nanoparticle solutions before deposition. After optimizing the deposition conditions, we found that we can decrease surface roughness and hence reduce diffuse scattering from the titania films by centrifugating the titania nanoparticle solutions before deposition. In particular we found that a pH value between 7.4 and 8.25 is preferable due to the fact that the titania nanoparticles maintain their negative charge to a point that allows them to be used with the appropriate polycation but not so high as to disable uniform deposition due to strong mutual electrostatic repulsion of the nanoparticles. For this pH value PDDA is a better choice than PAH. Regarding the other main source of surface roughness, nanoparticle aggregation in solution before deposition, we found that centrifugating the titania nanoparticle solutions at 6000g for ten minutes and discarding the sediment significantly reduced the average diameter of the remaining nanoparticles hence lead to reduced surface roughness on deposition. This result was again verified by AFM and SEM images. Ellipsometry data of titania nanoparticle films are better modeled by the Lorentz ellipsometry model which takes into account absorption from the film.

6.1.2 Quarter-Wave Stacks

The experiments on the quarter wave stacks showed that construction of such a configuration is possible by ISAM. The silica layer does not appear to be as sensitive to deposition conditions as the titania layer. The reflectance of the quarter wave stacks that we constructed under the optimum conditions followed the theoretical reflectance fairly well but more experiments are needed on this subject. In addition, the model used assumes a sharp boundary between the two layers of the quarter wave stack. This is an idealization which may be improved by adding a thin intermixing layer between the titania and the silica layers. Films constructed by use of a dipping machine did not show a significant difference in the responses. Ellipsometry data of the quarter wave stacks was modeled using a Lorentz model for the titania layer and an EMA model for the silica layer.

6.2 Future Work

The above results show that construction of a HL quarter wave stack by ISAM is possible. It should be remembered that our results are based on only one set of experiments. There is much more work that can be done to optimize the quarter wave stack deposition and to obtain consistency with the calculated models. To illustrate this point we look at the eight quarter wave stacks that were constructed with solution pH = 7.5 as an example. Similar considerations apply to the other quarter wave stacks as well.

6.2.1 Additional Experiments with Quarter-Wave Stacks

The model that we used to fit the eight quarter wave stacks (Fig. 5.7) that were constructed with solutions of pH = 7.5 was not unique. This is to say that in order to fit the model to these eight quarter wave stacks we had to modify the thicknesses of the individual layers. Hence the few results that we analyzed were not reproducible. Table 6.1 shows the details of the factors under which these four films we constructed.

SAMPLE	MOLARITY OF SILICA (mM)	DIPPING METHOD	WASH TIME (min)
2	3500	Hand	1
5	350	Hand	2
11	350	Hand	1
12	3500	Hand	2
13	3500	Machine	1
15	350	Machine	2
16	3500	Machine	2
19	350	Machine	1

Table 6.1. Silica molarities and wash times for the eight analyzed quarter wave stacks. All samples were constructed with solution pH = 7.5.

pH was the only statistically significant factor as far as any response is concerned (Table 5.4) with an occasional weak effect from the molarity of silica. Wash time was always statistically insignificant. The fact that we were unable to fit these samples, even the subset of them with the same silica molarity, with one model indicates that there may be other factors that we have not considered and that a greater number of similar experiments will be necessary in order to account for this discrepancy and acquire reproducibility of our results.

6.2.2 Improved Models

To model our quarter wave stacks we used the model described in Section 1.2.2[1]. The titania layer was modeled by the Lorentz model[2], while the silica layer by the EMA model[3]. This model assumes a sharp boundary between the titania and the silica layers. Since our films consist of nanoparticles and are necessarily not homogeneous, we should expect a thin intermixing layer at the boundary. A possible modification to the above described model can include a thin intermixing layer between the titania and the silica layers that can be modeled by performing EMA with three materials, silica, void, and titania modeled by Lorentz. This configuration is schematically shown in Fig. 6.1.

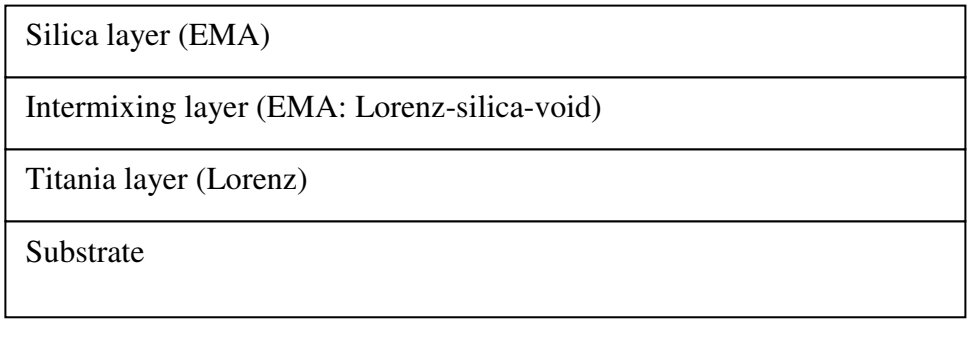

Fig. 6.1. Schematic of a possible improvement for the quarter wave stack model.

The characteristic matrix would then be the product of three matrices (Equation 1.2).

6.2.3 Further Considerations

In addition to the considerations in Section 6.2.1 there are further aspects of our films that can be investigated. It would be desirable to control the thicknesses of the two layers as well as their refractive indices. Considerable more work can be done with titania films to further reduce diffuse scattering and improve their optical properties. Silica film strength has been researched but similar work on titania films can also be done to improve film robustness and durability. Finally, a quarter-wave stack does not have to be limited to two layers. The model can be easily extended to an arbitrary number of layers by multiplication of the appropriate number of characteristic matrices. In addition to HL quarter wave stacks, LH quarter wave stacks can also be constructed by ISAM. The only difference is the reversal of the order of the two layers, silica first, titania second. A seemingly unlimited amount of work can be done on these subjects. These suggestions for future work are summarized below:

- Further reduction of diffuse scattering for titania films. Diffuse scattering is an undesirable effect of nanoparticle films. Further experiments may provide ways to reduce it. Polycations other than PDDA could provide a means for further reduction of diffuse scattering.
- Further experimentation with construction of quarter wave stacks with more layers. It can be shown that the value of R can approach zero as the quarter wave stack includes more layers. In theory ISAM can be used to construct films of unlimited thickness

consisting of several different layers of materials. Experimental verification of this expectation would be desirable.

- Optimization of quarter-wave stack deposition. Identification and investigation of new factors. This relates to the previous two points. Optimized deposition should reduce diffuse scattering and be applicable to quarter wave stacks with more layers.
- Control of optical properties and thicknesses of both components of the quarter wave stacks. This is probably the most important point especially since ISAM is a simple technique that should provide this advantage. It is important for the construction of a broadband AR coating that we are able to deposit layers with high contrasts in refractive indices. Since we are depositing nanoparticles, the refractive index of the layer depends highly on the volume fraction of the film occupied by the nanoparticles. Control over the volume fraction of the nanoparticles is therefore very important.
- New ellipsometry models that incorporate diffuse scattering as a distinct loss mechanism from absorption. This item has been addressed briefly in Section 1.2.4.2 and will require considerable investigation and modification of current models.
- LH quarter wave stacks. The same configuration but with the order of the high and low refractive index layers reversed. The reflectance and transmittance can be easily calculated using the product of the characteristic matrices of the two materials in reverse order. Such a configuration can be shown to maximize R therefore reducing T.
- Investigation and improvement of film strength and durability. This is important for many applications of AR coatings such as photocells or building windows. The films used in these cases are usually exposed to adverse weather conditions and it is desirable that they are able to withstand them. Several tests are available for testing film cohesion and adhesion such as tape peel tests. The photocatalytic properties of titania may also provide an area of exploration. Exposing titania or silica nanoparticles to UV light may provide useful results. Finally, we did not experiment with calcination of titania films. This process can have an effect on film strength since it can fuse the titania nanoparticles together as well as remove organic polycations and possible organic impurities.

References for Chapter Six

1 Eugene Hecht, *Optics*. (Addison Wesley, 2002), Fourth ed.

2 Frederick Wooten, *Optical Properties of Solids*. (Academic Press, 1972).

3 T. Furukawa, K. Yasuda, and Y. Takahashi, "Dielectric and conductive spectra of the composite of barium titanate and LiClO4-doped polyethylene oxide," Ieee Transactions on Dielectrics and Electrical Insulation **11** (1), 65-71 (2004).